D-MEM
PhD-UNIMI

Doctorate program
Milan
EXPERIMENTAL
MEDICINE

Università degli Studi di Milano

PhD Course in
Experimental Medicine

CYCLE XXXV

PhD thesis

Induced pluripotent stem cells (iPSC) to study pathomechanisms associated to Amyotrophic Lateral Sclerosis (ALS)

Candidate: **Dr. Santangelo Serena**
Matr. R12646

Tutor: **Prof. Antonia Ratti**
Director: **Prof. Nicoletta Landsberger**

Academic Year 2021-2022

TABLE OF CONTENTS

ABSTRACT

Amyotrophic Lateral Sclerosis (ALS) is a currently incurable and adult-onset neurodegenerative disease, characterized by the progressive and selective loss of upper and/or lower motor neurons, leading to a relentless and severe muscular atrophy with rapid death of patients, usually due to respiratory failure. The majority of ALS patients (90%) manifest a sporadic form with a multifactorial etiology, while 10% of cases are familial with more than 30 causative genes identified so far. The main genetic cause of ALS is represented by the intronic GGGGCC hexanucleotide repeat expansion (HRE) in *C9ORF72* gene which is polymorphic in healthy subjects (2-23 units), while in ALS patients it expands from 30 to more than 4000 units. The pathomechanisms associated to *C9ORF72* HRE include a loss of function due to C9ORF72 protein haploinsufficiency because of reduced transcription, and a toxic gain of function caused by both the formation of pathological HRE-containing RNA foci and the synthesis of dipeptide repeat proteins (DPR) resulting from RAN translation of the HRE-containing transcripts. *C9ORF72*-associated defects include impairment of RNA metabolism, genomic stability, DNA damage response (DDR), nuclear pore integrity and axonal transport.

The study of ALS pathomechanisms has always been hampered by the lack of suitable experimental models that could properly mimic the pathophysiology of the disease. The quite recent possibility to obtain patient-derived induced pluripotent stem cells (iPSC) represents a great advancement to study neurodegenerative disorders, because iPSC maintain the individual genetic background and can be differentiated into different neuro-glial cell lineages, including motoneurons and cortical neurons.

In my PhD project I exploited iPSC, reprogrammed from *C9ORF72* ALS patients, to study DNA damage and DDR and their possible link with actin cytoskeleton remodeling, and to test a novel RNA- based therapeutic approach to reduce *C9ORF72* pathology. I also established a new patient-derived iPSC line to elucidate the different pathomechanisms associated with *KIF5A* gene mutations.

To study DNA damage and DDR, we differentiated three *C9ORF72* and two healthy control iPSC lines, already reprogrammed in the lab, into both neural stem cells (iPSC-NSC) and motor neurons (iPSC-MN) at different maturation time (day 34 and 56). DNA damage was induced with the radiomimetic agent Neocarzinostatin and the phosphorylated histone H2AX (γH2AX) was used as marker of DNA breakage. By measuring the mean number of γH2AX-positive foci, the γH2AX mean fluorescence intensity in the cell nucleus and the percentage

of γH2AX foci-positive cells, we found that the presence of the *C9ORF72* HRE did not impact on the extent of DNA damage and DDR ability in iPSC-NSC. *C9ORF72* iPSC-MN (day 34) displayed a higher extent of DNA damage at physiological level compared to *wild-type* controls and they were able to recover the induced DNA damage after 6 hours rescue. However, prolonging the maturation time of iPSC-MN *in vitro* (day 56), we observed both a significant higher extent of DNA damage and an impaired ability of *C9ORF72* iPSC-MN to activate DDR compared to control iPSC-MN.

During my 3-months internship in the USA, I applied an innovative method to differentiate cortical neurons from one *C9ORF72* and one isogenic *wild-type* i^3-iPSC line using an inducible system. I found that modulation of the F-actin cytoskeleton using actin-modifier drugs had an impact on the incidence of DNA damage, DDR and chromatin remodeling.

To decrease *C9ORF72*-associated pathology, I used iPSC to test a novel RNA-based approach consisting in a modified spliceosomal U1 snRNA specifically designed to bind the sense transcript of the *C9ORF72* HRE. We first demonstrated U1 snRNA efficacy in reducing RNA foci and DPR formation in HEK293T cells, then we validated our results in *C9ORF72* iPSC-MN infected with U1-lentiviral vectors. We found that modified U1 snRNA could significantly decrease both the mean number of pathological RNA foci/cell and the percentage of *C9ORF72* iPSC-MN forming RNA foci.

I also took advantage of iPSC technology to establish a new *in vitro* model to study why different mutations in *KIF5A* gene may cause ALS or hereditary spastic paraplegia (HSP). *KIF5A* encodes for a microtubule motor protein involved in the anterograde transport in neurons. I reprogrammed fibroblasts from a HSP patient carrying a novel *KIF5A* mutation (p.R17Q) into iPSC and also generated its isogenic *wild-type* and a lof iPSC line using CRISPR/Cas9 gene editing. I differentiated these iPSC lines into MN to study and compare their differentiation capacity, mitochondria morphology and distribution along neurites as well as the axonal transport of mitochondria through live-cell imaging assay.

The results obtained in my PhD thesis provide evidence that patient-derived iPSC and iPSC-MN represent suitable *in vitro* platforms both to model *C9ORF72* and *KIF5A*-related pathogenetic mechanisms and to screen new promising therapeutic approaches for the treatment of ALS disease.

DISCLOSURE FOR RESEARCH INTEGRITY

I state that this scientific research was conducted following the principles of good research practice of the European Code of Conduct for Research Integrity, based on the principles of reliability, rigor, honesty, respect and accountability.

ABBREVIATIONS

Amyotrophic Lateral Sclerosis (ALS)
Motor Neuron Disease (MND)
Upper Motor Neuron (UMN)
Lower Motor Neuron (LMN)
Sporadic Amyotrophic Lateral Sclerosis (SALS)
Familial Amyotrophic Lateral Sclerosis (FALS)
Next Generation Sequences (NGS)
Whole Exome Sequencing (WES)
Whole Genome Sequencing (WGS)
Genome-Wide Association (GWA)
Single Nucleotide Polymorphism (SNP)
Frontotemporal Dementia (FTD)
ALS Patients with Cognitive Impairment (ALS-ci)
ALS Patients with Behavioral Impairment (ALS-bi)
Chromosome 9 Open Reading Frame 72 (*C9ORF72*)
SuperOxide Dismutase type 1 (*SOD1*)
TAR DNA-Binding Protein 43 (TDP-43)
FUsed in Sarcoma (*FUS*)
Hexanucleotide Repeat Expansion (HRE)
Transcription Start Sites (TSS)
Differentially Expressed in Normal and Neoplastic (DENN)
GDP-GTP Exchange Factors (GEF)
Loss Of Function (LOF)
Central Nervous System (CNS)
Gain Of Function (GOF)
Repeat Associated Non-AUG translation (RAN)
DiPeptide Repeat (DPR)
Kinesin Family Member 5A (KIF5A)
Charcot-Marie-Tooth (CMT)
Hereditary Spastic Paraplegia (HSP)
Kinesin Heavy Chain (KHC)
Kinesin Light Chain (KLC)

DNA Damage Response (DDR)
Reactive Oxygen Species (ROS)
H2A histone family member X (H2AX)
Ataxia-Telangiectasia Mutated (ATM)
Ataxia Telangiectasia and Rad3-related (ATR)
Poly ADP-Ribose Polymerase (PARP)
p53 Binding Protein (53-BP1)
Homologous Recombination (HR)
Non-Homologous End-Joining (NHEJ)
Double Strand Break (DSB)
Nucleo Cytoplasmic Transport (NCT)
Nuclear Pore Complex (NPC)
LInker of Nucleoskeleton and Cytoskeleton (LINC)
Nuclear Transport Receptors (NTR)
Ran with associated GTPase-Activating Protein (RanGAP)
Ran Guanine nucleotide Exchange Factor (RanGEF)
Tubulin alpha-4A (*TUBA4A*)
NIMA-related Kinase 1 (*NEK1*)
Latrunculin (LATR)
Intramimic 01 (IMM01)
Pectenotoxin-2 (PTX-2)
Neurofilament Light chain (NF-L)
Ribonucleoprotein (RNP)
Neurofilament heavy subunit (*NEFH*)
Peripherin (*PRPH*)
Peripheral Blood Mononuclear Cells (PBMC)
Induced Pluripotent Stem Cells (iPSC)
Neural Stem Cells (NSC)
Moto Neuron (MN)
Cortical Neurons (CN)
Clustered Regularly Interspaced Short Palindromic Repeats (CRISPR)
NeuroMuscular Junction (NMJ)
AntiSense Oligonucleotide (ASO)

INTRODUCTION

1. Amyotrophic Lateral Sclerosis

1.1. Clinical features

Amyotrophic lateral sclerosis (ALS), also known as Lou Gehrig's disease, is the most common adult motor neuron disease (MND) accounting for 80-90% of all MND cases (1). ALS has a mean incidence between 0.6 and 3.8 per 100.000 persons per year, and occurs with a higher frequency in males than in females with a 2:1 ratio (2).

ALS is an adult-onset, rapidly progressive and ultimately fatal disorder, presenting a great clinical heterogeneity across patients in terms of age of onset, progression rate and clinical symptoms. The mean age of onset ranges from 51 to 66 years and the mean survival ranges from 2 to 5 years (2).

Two main ALS clinical variants are identified according to the clinical site of onset, which includes a spinal or a bulbar one. The spinal onset is the most common form of ALS (80% of cases), selectively involving the motor function of upper or lower limbs without affecting sensitive and autonomic aspects. The bulbar site of onset (20% of cases) causes dysarthria (slurred speech), dysphagia (difficulty in swallowing), dysphonia (abnormal voice), sialorrhea (excessive drooling) and *ab ingestis* pneumonia (aspiration pneumonia), being epidemiologically related to a more rapid disease course. The other main clinical stratification of ALS forms is based on the early involvement of upper motor neuron (UMN) in the motor cortex (central motor neuron) or lower motor neuron (LMN) in the brainstem and spinal cord (peripheral motor neurons). Patients can suffer from hyporeflexia, flaccid paralysis, fasciculations and muscular atrophy if the LMN is primary involved, or from hyperreflexia and spastic paralysis due to UMN degeneration. The disease is characterized by a progressive and severe muscular atrophy which leads to a progressive paralysis with patients usually dying for respiratory failure within 2-3 years from the onset.

Over the last decades, more than 40 randomized controlled trials in ALS patients have been carried out, but they all failed to show a beneficial effect on disease progression or on survival (3). So far, Riluzole (t/a Rilutek, Aventis Pharma S.A.), an inhibitor of glutamate release, remains the first and only disease-modifying drug to prolong mean survival by 3–6 months with no effect on muscular strength (4). More recently, the free radical scavenger Edaravone (t/a Radicava^{TM}, Mitsubishi Tanabe Pharma America), which is thought to prevent oxidative stress damage to neurons, has been approved for the treatment of ALS in

the USA, Canada, Japan, South Korea and Switzerland, but not in the European Union (5). It ameliorates patients' mobility, increasing survival just by few months. Another therapy under investigation is Masitinib (t/a Masivet, AB Science), an oral tyrosine kinase inhibitor, which recently received the FDA approval to start Phase III clinical trial(6). However, none of these drugs can ameliorate the course of the disease, and progress towards finding effective therapies is hampered by an incomplete understanding of disease etiopathogenesis and by the lack of suitable experimental disease models.

1.2. Etiology

Similar to other neurodegenerative disorders (Alzheimer's and Parkinson's diseases), ALS has a multifactorial etiology consisting in a combination of both genetic and environmental risk factors and aging-related dysfunctions. 90% of ALS cases manifest a sporadic form of the disease (SALS), since no other cases of ALS or related neurodegenerative disorders have been previously diagnosed in the same pedigree.

The remaining 10% of ALS cases are instead considered familial (FALS), with a higher frequency in females, an earlier age of onset and a more rapid disease progression. Among FALS cases, about 70% are due to mutations in 30 different causative genes. Four major genes (*C9ORF72, SOD1, TARDBP* and *FUS*) account for about 60% of FALS cases, whereas 10% is due to a plethora of minor genes (7). The remaining 30% FALS cases still have an unknown genetic cause and Next Generation Sequences (NGS) approaches, including Whole Exome Sequencing (WES) and Whole Genome Sequencing (WGS), are now exploited to identify this missing hereditability in large international collaborative efforts.

Among SALS cases, about 10% are represented by unrecognized FALS cases, because of *de novo* mutations, incomplete penetrance, somatic mosaicism or incomplete familial anamnesis. The majority of SALS cases are due to a multifactorial etiopathogenesis and Genome-Wide Association (GWA) studies in association to WGS have recently allowed to define several common variants (single nucleotide polymorphisms - SNPs) conferring susceptibility to the disease development (8). Among these risk factors, intronic SNPs in *UNC13A* gene are among the strongest hits associated with ALS and determine a decreased TDP-43 binding affinity which leads to the inclusion of a repressed cryptic exon with a premature stop codon in *UNC13A* mRNA (9,10).

The genetic architecture of ALS is therefore complex, ranging from monogenic mutations with high effect size in FALS cases to common and rare genetic variants with low and moderate effect size in SALS cases with an oligogenic model (11).

Among the environmental factors, smoke, exposure to chemicals, heavy metals and intense physical exercise have been associated to an increased risk of developing ALS, together with genome-wide epigenetic modifications (12).

1.3. ALS and fronto-temporal dementia spectrum

Clinical studies conducted in the last 20 years have demonstrated an overlap between motor neuronal degeneration in ALS and cortical neuron death in frontotemporal dementia (FTD). During the course of the disease, 15% of ALS patients may indeed develop also FTD, resulting in abnormalities of behavior and language, whereas about 40% of ALS patients show subclinical executive and behavioral dysfunctions (ALS-ci, ALS-bi) (13). Conversely, 15% FTD patients also develop ALS, but many more have some evidence of lower motor neuron involvement (14). The existence of common neuropathological features between ALS and FTD was discovered in 2006 with the identification of TDP-43 as a major disease protein in the cytosolic ubiquitinated and phosphorylated inclusions of 97% ALS and of 45% FTD brain tissues (15,16). TDP-43 inclusions indeed represent the neuropathological hallmark of nearly all ALS patients, both FALS and SALS, with the exception of *SOD1*- and *FUS*-mutated patients. Defective TDP-43 nucleocytoplasmic transport, post-translational modifications or impairment of the protein degradation system are some of the mechanisms that have been proposed to promote nuclear TDP-43 protein mislocalization and aggregation in the cytoplasm (17). Moreover, mutations in *TARDBP* gene (encoding TDP-43), identified in 5% of FALS patients, may promote an increased localization and aggregation of the mutant protein in the cytoplasm (18).

The further identification of a common genetic cause of ALS and FTD – the chromosome 9 open reading frame 72 (*C9ORF72*) gene (19,20) – definitively confirmed the clinical and neuropathological evidence that ALS and FTD represent two ends of the same disease spectrum.

1.4. C9ORF72 gene

C9ORF72 was identified in 2011 as causative of both ALS and FTD (19,20). *C9ORF72* is so far the major causative gene in both disorders, accounting for about 35% of FALS and 6% of SALS cases, and for 26% of familiar FTD and 5% of sporadic FTD cases (21).

C9ORF72 has been additionally identified as a rare cause of other neurodegenerative and psychiatric disorders, including Alzheimer's disease, Parkinson's disease, Huntington's disease, multiple sclerosis, bipolar disorder and schizophrenia (22,23).

C9ORF72 mutation consists in the expansion of the GGGGCC hexanucleotide repeat (HRE) located in the first intron of the gene. In the normal population, the length of the hexanucleotide repeat is polymorphic and ranges from 2 to 23 units, whereas in ALS/FTD patients it exceeds 30 up to more than 4000 units (24). The age of onset of *C9ORF72* HRE carriers is slightly earlier than in *C9ORF72*-negative ALS/FTD patients, survival is reduced, and families exhibit high phenotypic variability regardless HRE size (25). Genetic anticipation is not so evident and both expansions and contractions of the HRE length are observed in ALS/FTD pedigrees (26,27). The mutation has an autosomal dominant inheritance, but the penetrance is incomplete and age-dependent (nearly complete by 83 years of age) (28,29) so that apparently sporadic mutated patients indeed represent undiagnosed familiar *C9ORF72* cases. Interestingly, there is not a clear correlation between the HRE size and the disease clinical presentation in terms of age of onset, progression rate and clinical symptoms, including the development of ALS, FTD or both. This suggests that the genotype-phenotype correlation could be also influenced by modifying factors such as somatic mosaicism, oligogenicity and promoter DNA methylation (25,30).

C9ORF72 gene is located on the reverse strand of the short arm of chromosome 9 (C9p21.2-p13.3). The gene is 27,320 base pair long and is composed of 12 exons and 11 introns. The two first exons belong to the non-coding 5'UTR of the gene and contain alternative transcription start sites (TSS) which generate three different *C9ORF72* mRNA isoforms (V1, V2 and V3) (**Fig. A**). V1 and V3 are transcribed from the first exon 1a TSS, upstream the intronic GGGGCC repeat, while the V2 isoform, that is the most abundant transcript, is transcribed from exon 1b TSS, located downstream the hexanucleotide repeat which acts as a promoter (29). V2 and V3 are translated into a long protein isoform of 55 kDa (481 amino acids), encoded by exons 2-11, while the V1 isoform (exons 2-5) is shorter and encodes for a 25 kDa (222 amino acids) protein (**Fig. A**).

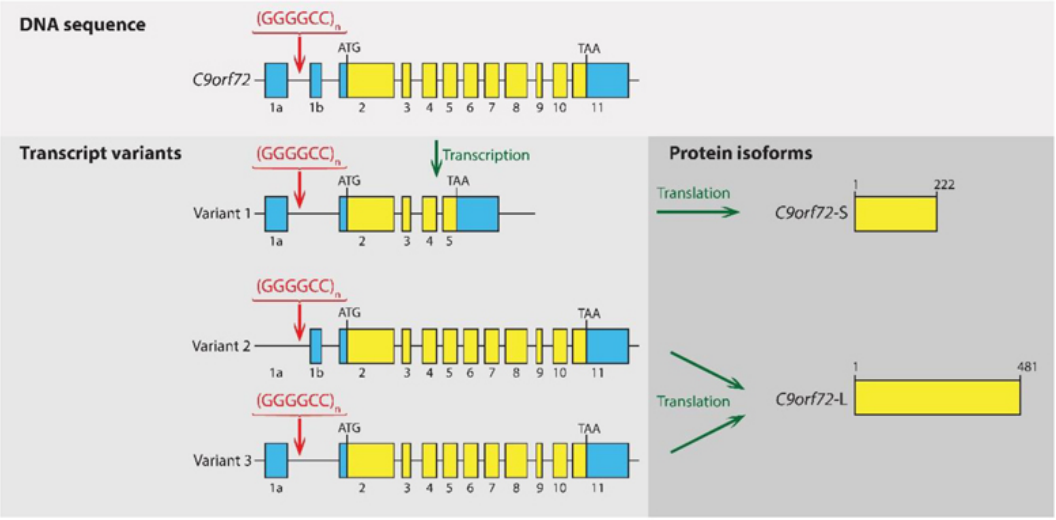

Fig.*A C9ORF72* gene structure, transcript variants and protein isoforms. Representation of the *C9ORF72* gene with its 11 exons and the three mRNA isoforms generated by transcription from the alternative exons 1a and 1b and alternative splicing. The two protein isoforms, short (S) and long (L), generated by translation of the three transcript variants are shown. The GGGGCC repeat, located in the first intron of variants 1 and 3 and in the promoter of variant 2, is indicated in red.

C9ORF72 protein activity is still unclear although, based on protein structure analysis, it was found to contain a DENN-like (Differentially Expressed in Normal and Neoplastic cells) domain typical of GDP-GTP exchange factors (GEFs) for Rab GTPases, which regulate intracellular compartments trafficking (31). The N-terminal end of the three mRNA isoforms (exon 2-5) harbors a Longing domain, that is known to interact with various types of GTPases involved in the endoplasmic reticulum to Golgi transport, while only the long isoforms (exon 2-11) also contain the DENN and the C-terminal alpha domain involved in GTPase activation (31). The long *C9ORF72* isoforms were identified to participate in the autophagosome assembly machinery and to mediate the trafficking of the key autophagy initiation ULK1 complex (32). Furthermore, C9ORF72 was demonstrated to be localized at the lysosome membranes, where it seems to recruit mTORC1 targets, contributing also to protein synthesis control by the mTOR pathway (33). *C9ORF72 knock-out* mice did not develop motor neuron disease but showed alterations in myeloid and/or lymphoid cell populations in the spleen and lymph nodes with increased levels of inflammatory cytokines, suggesting an important role of C9ORF72 also in immune response regulation (34).

1.4.1. C9ORF72-related pathogenetic mechanisms

In ALS and FTD the presence of *C9ORF72* HRE can induce neurodegeneration by three distinct, and not mutually exclusive, pathogenetic mechanisms, that are all likely to contribute to disease development (**Fig. B**).

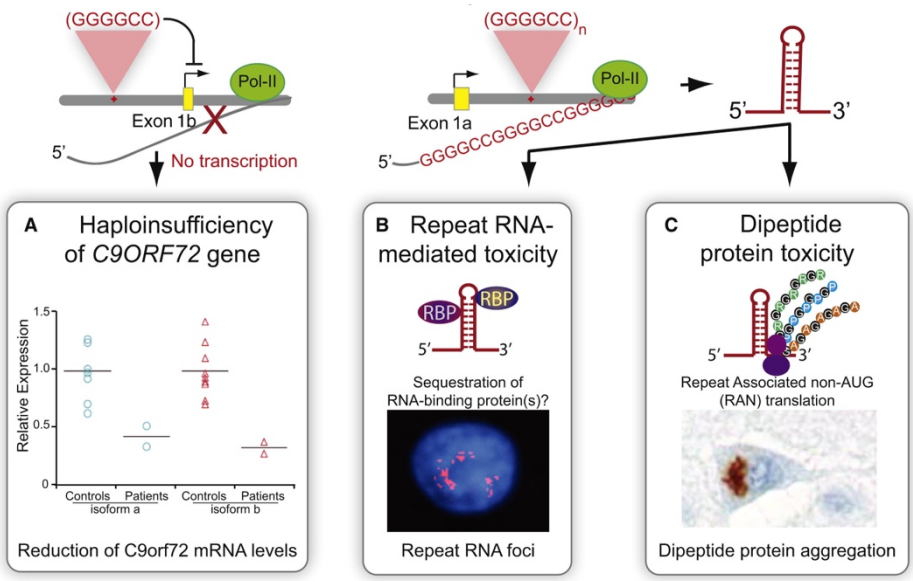

Fig. B Proposed pathogenic mechanisms for the GGGGCC HRE in *C9ORF72* gene. (A) The HRE located upstream exon 1b in the V2 promoter may inhibit the transcription of this isoform, leading to C9ORF72 protein haploinsufficiency. (B) The intronic HRE can be transcribed from the alternative exon 1a, leading to the formation of stable secondary structures containing the HRE, visualized as RNA foci in cells, that can also sequester RNA-binding proteins. (C) The transcribed HRE-containing RNAs undergo non-canonical repeat-associated non-ATG dependent (RAN) translation and lead to the production of different dipeptide proteins in each of three reading frames (35).

The first pathomechanism is a C9ORF72 protein loss-of-function (LOF). In the brain of *C9ORF72* patients the total level of *C9ORF72* mRNA and protein was found to be reduced by nearly 50% compared to controls (36,37). In particular, gene expression analysis of *C9ORF72* showed that the main V2 isoform is downregulated, indicating that the presence of the HRE in the V2 promoter inhibits the transcription of this isoform, resulting in protein haploinsufficiency (37).

The affected downstream pathways resulting from *C9ORF72* LOF have been widely studied. *Knock-down* of *C9ORF72* in human cell lines and primary neurons inhibits autophagy induction and neurons from *C9ORF72* patients show impaired basal autophagy, indicating that C9ORF72 reduced levels contribute to cellular distress (32,34). Moreover, reduced endocytosis was reported in *C9ORF72* knock-down cell lines (38) and impaired endosomal and lysosomal trafficking was observed in *C9ORF72* patients-derived fibroblasts and iPSC-

neurons (39). Transcriptomic changes in immune system pathways similar to those observed in the central nervous system (CNS) tissue from patients with *C9ORF72* HRE have also been found in *C9ORF72 knock-out* mice, suggesting an immune system dysregulation caused by *C9ORF72* haploinsufficiency (34).

The second pathomechanism is a toxic gain-of-function (GOF) at the RNA level. When the intronic HRE is transcribed from exon 1a, the formating V1 and V3 pre-mRNAs are very rich in GC nucleotides that give rise to secondary RNA structures, including hairpins and highly stable G-quadruplexes, as well as to RNA-DNA hybrids called R-loops (40,41). The HRE is also transcribed by the antisense strand giving rise to antisense RNA foci (42). The stable RNA G-quadruplex structures promote the formation of truncated RNA transcript containing the HRE that distribute both in the cytoplasm and in the nucleus as RNA foci (19,43,44). The HRE-containing transcripts act as an RNA GOF mechanism because the RNA foci can sequester, and consequently deplete, nuclear RNA-binding proteins and splicing factors, thus leading to possible alterations in RNA processing and transcription (45,46).

The third pathomechanism regards the toxic GOF at protein level. The sense and antisense transcribed HRE-containing RNAs are bidirectionally translated in all possible reading frames through a non-canonical repeat-associated non-ATG dependent (RAN) translation, leading to the production of five different dipeptide proteins (DPR): poly(GA), poly(GP) and poly(GR) from the sense frame; poly(GP), poly(PA) and poly(PR) from the antisense transcript (47,48). These DPRs form toxic aggregates in the cytoplasm specifically of brain and testis cells, in contrast to RNA foci which are ubiquitous (47,48). DPRs induce nucleolar stress, impair splicing and ribosomal RNA biogenesis, interfere with stress granules formation and cause nucleocytoplasmic transport alterations, contributing to neuronal cell death by different mechanisms (49,50).

Despite the debate in identifying the main pathomechanism responsible for *C9ORF72*-related pathology, it is likely that C9ORF72 haploinsufficiency and RNA or DPR toxicity altogether contribute, at different extent, to induce damage in multiple and fundamental pathways, culminating in neuronal loss in the motor system (ALS) and in frontal and temporal lobes (FTD).

1.5. KIF5A gene

A large-scale and combined GWA and WES study identifed mutations in *KIF5A* as a novel ALS-causative gene (51,52). *KIF5A* gene encodes for the Kinesin heavy chain isoform 5A and belongs to the ATP-dependent microtubule motor proteins, responsible for the anterograde transport in neurons. *KIF5A* gene is located on the sense strand of the long arm of chromosome 12 (12q13.3), encompasses 40,608 bases pair and is composed of 29 exons. In ALS patients, a mutational hot-spot was identified in the C-terminal domain of *KIF5A* gene (**Fig. C**). The p.Pro986Leu variant was identified as a relatively common, but low penetrance, risk allele for ALS, while loss-of-function variants in the C-terminal domain constitute rare, but with high penetrance, variants (51). The latters are predominantly located at the 5' and 3' splice junction of exon 27 (residues 998-1007) and they are expected to affect splicing causing the skipping of exon 27 (ΔExon27) yielding a protein with the normal C-terminal 34 aminoacids replaced by 39 aberrant aminoacids (51,52)

Interestingly, mutations in *KIF5A* have already been found to cause both Charcot-Marie-Tooth type 2 (CMT2), an autosomal dominant axonal sensorimotor peripheral neuropathy, and SPG10, an autosomal dominant form of Hereditary Spastic Paraplegia (HSP), a neurodegenerative disorder characterized by a slow, gradual, progressive weakness and spasticity of the lower limbs (53,54). In these disorders, in contrast to ALS, mutations are mainly localized at the N-terminal domain and are mostly missense variants mapping in the motor domain (53,55) (**Fig. C, on the left**). The motor protein kinesins are classified into 15 subfamilies (from 1 to 14B) and are encoded by 45 mammalian genes, 38 of which are expressed in the nervous system (56). Among them, Kinesin-1 isoform (also known as KIF5) is required for neuronal development and function, contributing to fast axonal transport (50-200 mm per day) of membranous organelles and slow axonal transport (0.1-3 mm per day) of cytoplasmic proteins, as well as dendritic and cell body transport. The list of their cargoes includes RNA granules containing RNA-binding proteins (like FUS and hnRNPA1), synaptic vesicle precursors (synaptotagmin and synaptobrevin), neurofilaments, mitochondria, lysosomes, tubulin dimers, endosomes, AMPA and GABA-A receptors and many other cargoes (57). Kinesin 1 isoform KIF5A, together with KIF5B and KIF5C isoforms, represent the heavy-chain subunits of the conventional kinesin, a tetrameric motor protein complex composed by two kinesin heavy chains (KHC) and two kinesin light chains (KLC), both assembled as homodimers (**Fig. C, on the right**). While KIF5B is ubiquitously expressed, with a prominent glial cells expression, KIF5A and KIF5C are, on the other hand, specific for neurons (58). In particular, KIF5A is composed by 1032 amino acids and organized in three

different domains: the motor domain, the stalk domain and the cargo-binding domain (**Fig. C, on the right**). At the N-terminal (1-324 residues) there is the globular motor domain ("head"), containing an ATP-binding sequence and a microtubule-binding sequence. This domain contains three elements (P-loop, switch 1, switch 2) which form the γ-phosphate-sensing regions. A "neck-linker" region (residues 325-340) connects them with the "neck" region (residues 341-370). The α-helical coiled-coil stalk domain (residues 371-906), flanked by two flexible regions, is involved in the KIF5A homodimerization and in the interaction with KLC dimer. The C-terminal globular domain (residues 907-1032), called the "tail", is responsible for the cargo and KLC binding, microtubule sliding/bundling and for the autoinhibition mechanism (59,60) (**Fig. C, on the right**).

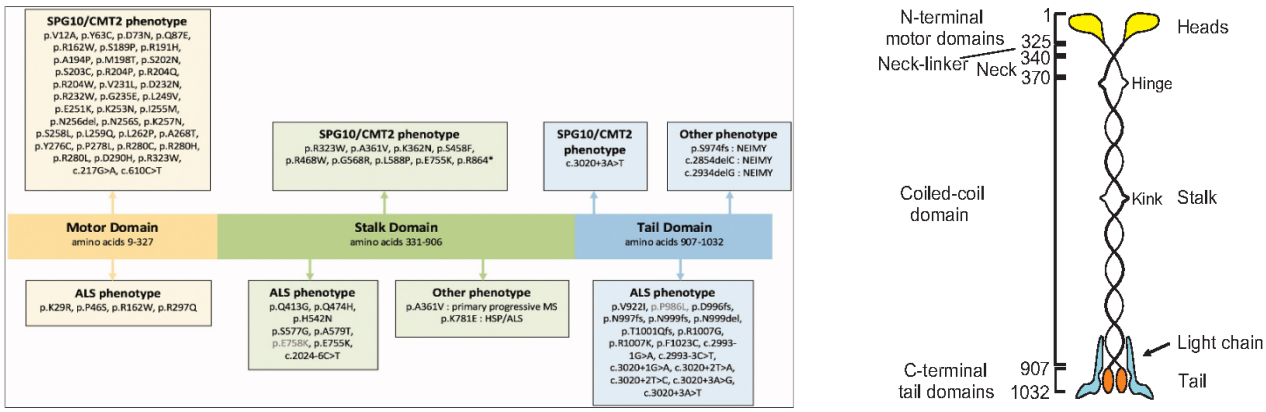

Fig. C KIF5A structure. **On the left**: Localization of reported *KIF5A* variants within the different regions of the gene and the associated phenotype (59). **On the right**: Structure of conventional kinesin tetrameric complex with two heavy chains (KIF5A) and two light chains. The different domains of KIF5A heavy chains are indicated (61).

The kinesin-1 motor proteins move toward the plus-ends of microtubules by processive motility, taking hundreds of sequential 8-nm steps, with multiple gating strategies responsible for an efficient movement. The two kinesin heads exert a "hand-over-hand" motion: at each step they exchange leading and trailing positions, hydrolysing ATP alternatively (62).

Several works conducted in Drosophila, mice and *in vitro* models showed that KIF5A is essential to supply constant energy to neurons, representing a structural scaffold for the elongation and maintenance of axon growth (63–65). For this reason, growing evidence suggest that defects in the axonal transport machinery or impairment in the axonal transport process could impair neuronal homeostasis, finally leading to neuronal degeneration.

2. ALS pathomechanisms

More than 30 causative genes have been associated to ALS so far and they have helped understand all the molecular mechanisms potentially leading to neurodegeneration also in sporadic ALS. These genes are involved in different cellular and molecular pathways, including RNA metabolism, protein quality control, autophagy, cytoskeletal dynamics and axonal transport, mitochondrial functionality, oxidative stress and DNA damage repair (66). I will specifically focus my attention on three ALS-related pathomechanisms: DNA damage and DNA damage response (DDR), cytoskeleton alterations and axonal transport.

2.1. DNA damage and DNA damage response (DDR)

DNA damage is a common event in cells and every cell is estimated to experience $10^4/10^5$ DNA lesions per day. Despite mutations are necessary to drive evolution, genomic instability has in most cases adverse effects on cell viability and human health. DNA damage can arise by both endogenous causes, such as spontaneous base modifications, replication errors or reactive oxygen species (ROS) production, and exogenous ones, such as genotoxic chemical agents or ultraviolet and ionizing radiations. Multiple types of DNA damage exist, including base modifications, base insertions-deletions or substitutions, formation of abasic sites, pyrimidine dimers, DNA adducts, DNA cross-links and DNA breaks, that can be single-strand breaks (SSB), if they involve just one chain, or double-strand breaks (DSB) (67). Depending on the extent of the damage and the risk of mutation, the cell activates DNA repair pathways or, following chronic activation of DNA damage response (DDR), induces apoptosis as a protective mechanism. The formation of SSBs or DSBs activates phosphorylation of the histone subunit H2AX (γH2AX), that initiates the recruitment of ATM (Ataxia-Telangiectasia Mutated) and ATR (Ataxia Telangiectasia and Rad3-related) proteins, triggering the DDR (68). PARP (Poly ADP-Ribose Polymerase) and 53-BP1 (p53 Binding Protein) are other important sensors that signal DNA damage during DDR. Depending on the type of DNA damage, the DDR can activate several different DNA repair pathways. SSBs are repaired primarily by excision repair mechanisms, whereas DSBs are repaired by either homologous recombination (HR) or non-homologous end-joining (NHEJ). However, in neurons, NHEJ is the primary mechanism, because HR requires active progression through the cell cycle (69). Another important player in DDR is represented by the nucleolus, because it contains over 160 DNA repair proteins and is responsible for the biogenesis of ribosomes and the regulation of response to stress (70). However, it is unclear

whether the nucleolus is simply a storage hub for DDR proteins or if these proteins have specific roles in DNA repair in the nucleolus.

Neurons are generally considered to be more vulnerable to DNA damage than other cell types, because of their high metabolic rate and their reliance on oxidative phosphorylation for energy production that leads to very high ROS levels. A further explanation is their post-mitotic status, that makes them more likely to accumulate DNA damage compared to mitotic cells.

DNA damage and impaired DDR have been implicated to play a role in multiple neurodegenerative disorders, including Alzheimer's, Parkinson's and Huntington's diseases, as well as in ALS. DNA damage and DDR defects were established to be involved in ALS pathogenesis two decades ago, when increased levels of oxidative DNA damage and reduced levels of factors involved in DDR were identified in both FALS and SALS autoptic spinal cord motor neurons (71). Subsequently, the discovery that many important ALS causative genes are involved in DDR reinforced the idea of defective DNA repair as a novel ALS pathogenetic mechanism. SOD1 protein, with its antioxidant activity, protects DNA from oxidative DNA damage and its mutations result in increased ROS production, thus favoring DNA insults (72). Indeed, *SOD1*-mutated spinal motor neurons from post-mortem tissues displayed increased DNA damage and motor neuron degeneration (73). Interestingly, in mutant *SOD1* iPSC-motor neurons DNA repair capacity was not affected, suggesting that vulnerable ALS neurons accumulate DNA damage and strongly activate response and DNA repair genes effectors (73). It has also been demonstrated that the nuclear FUS RNA-binding protein indirectly regulates HR and NHEJ in primary mouse neurons and increased expression of γH2AX has been found in the motor cortex of ALS patients with *FUS* mutations (74). This evidence indicates that FUS could be involved in DNA damage signaling and suggests that the formation of pathological FUS aggregates into the cytoplasm may affect the prevention and/or repair of aberrant transcription associated to DNA damage. Although a possible function of TDP-43 in the regulation of transcription-associated DNA damage has been suggested (75), a convincing role for TDP-43 in DNA repair has not been demonstrated yet.

Other ALS genes have also been related to DNA damage and DDR, among which *C9ORF72* (see below paragraph 2.1.1.) and other minor genes such as *NEK1* (76) and the risk factor *C21ORF2* (77), which act together in DNA damage repair, and *SETX*, a DNA helicase associated also to R-loops resolution (78).

2.1.1. C9ORF72 gene in DNA damage and DDR

Major evidence of *C9ORF72* gene involvement in DNA damage and DDR was gained when increased DNA damage levels were found in autoptic spinal cord motor neurons (79,80) and iPSC-motor neurons (iPSC-MN) from *C9ORF72* patients in an age-dependent manner (81,82), compared to *wild-type* healthy controls. Products of *C9ORF72* HRE, the toxic HRE-containing RNA and DPRs, have been suggested as the primary effectors through which *C9ORF72* mutations lead to increased DNA damage, as their sole expression in different neuronal cell models is sufficient to induce DSB (79,81,83). The expression of the HRE-containing RNA or of the DPR poly(GA) in human immortalized cell lines was able to favor DSB via increased formation of R-loops, naturally occurring RNA-DNA hybrids that are known to favor DNA strand breaks. Accordingly, overexpression of *SETX*, also mutated in some FALS cases, partially rescued DNA damage levels, as well as cell death (84). Moreover, R-loops, in parallel to DNA damage, were shown to be increased in *C9ORF72* patient's post-mortem spinal cord tissue (80). Expression of the DPR poly(GR) in iPSC-MN derived from *wild-type* controls, instead, induced DNA damage via increased production of ROS (81). Moreover, increased ROS levels in an age-dependent manner were found in *C9ORF72* patient-derived iPSC-MN and, accordingly, the treatment of these iPSC-MN with an antioxidant partially rescued DNA damage levels (81). iPSC-MN from *C9ORF72* patients showed increased DNA damage levels not only in basal conditions, but also after induction of DNA damage by γ-irradiation, suggesting an impaired DDR (82). Chromatin compaction and the expression of histone-modifying factors that promote this process are increased in *C9ORF72* patients' autoptic spinal cord MN and in cells transfected with the DPR poly(GA), which could further inhibit the access of repair factors to DNA. Accordingly, induction of chromatin relaxation in poly(GA)-transfected cells was able to reduce DNA damage levels and cell death (80). While poly(GA), poly(GR) and poly(PR) expression in human immortalized cell lines all caused DNA damage, the dipeptide proteins showed different effects on DDR (85). While cells transfected with poly(GA) showed reduced levels of pATM-positive foci, cells transfected with poly(GR) and poly(PR) showed increased levels of pATM, suggesting that poly(GA) DPRs sequester pATM in the cytoplasm, preventing its recruitment to DNA damage sites (86). Moreover, poly(GA), poly(GR) and poly(PR) were shown to affect non-homologous recombination and single-strand annealing, while having no effect on homologous recombination (83).

2.2. Nucleocytoplasmic transport (NCT)

Nucleocytoplasmic transport (NCT) is a tightly regulated process that controls the exchange and the cellular distribution of proteins and RNA molecules between the nucleus and the cytoplasm. NCT function is regulated by three main group of proteins, including:

1) nucleoporins, that constitute the nuclear pore complex (NPC), acting as a tightly controlled barrier for the shuttling of high molecular weight proteins in and out of the nucleus. In this context, the nuclear lamina interacts with both the nucleoporins on the nucleoplasmic side, mediating their positioning and anchoring to the nucleus, and with the cell cytoskeleton on the cytoplasmic side through its interaction with the LINC (LInker of Nucleoskeleton and Cytoskeleton) complex (87).

2) the Nuclear Transport Receptors (NTRs), which drive RNA and protein cargo through the selective permeability barrier of the NPC.

3) the small GTPase RanGAP1 (Ran with associated GTPase-Activating Protein) or RanGEF/RCC1 (Ran Guanine nucleotide Exchange Factor), which are responsible for the directionality of transport and regulate NTR-specific cargo loading and release in the nucleoplasm and cytoplasm (88).

In ALS, abnormal protein aggregation, oxidative stress and cytoskeletal dysregulation may directly or indirectly cause NCT defects, such as loss of nuclear pores and nucleoporin aggregation, altered nuclear morphology and impaired nuclear transport, contributing to protein mislocalization between the nuclear and cytoplasmic compartments (89). The first evidence linking NCT machinery defects to ALS pathogenesis was from the observation of nuclear membranes with an abnormal shape and aberrant NTRs distribution in spinal motor neurons from SALS and FALS patients carrying *SOD1* mutation (90). Another study showed that fibroblasts from TDP-43-mutated and SALS patients were characterized by abnormal nuclear shape and nucleoporin distribution (91). The NCT defects are caused by the presence of pathological TDP-43 inclusions that sequester nucleoporins into aggregates, preventing their normal localization and function (91). In contrast to TDP-43, there is currently little evidence that FUS pathology directly induces NCT defects, although FUS cytoplasmic mislocalization in ALS has been well studied (92). It is known that the silencing of Exportin-1, which mediates the nuclear export of proteins, significantly reduced the propensity of both *WT* and mutant FUS to form cytoplasmic granular inclusions upon stress induction with sodium arsenite (93), suggesting that NCT proteins can modulate FUS subcellular localization and aggregation, thus affecting its cell toxicity.

Overall, all this evidence suggests that NCT defects represent a common hallmark in ALS pathobiology, even if the molecular mechanisms regulating NPC stability and function triggering NCT disruption have not been explored yet.

2.2.1. C9ORF72 gene in NCT disruption

As mentioned before, C9ORF72 protein activity has not been fully elucidated yet. However, it has been demonstrated that the short C9ORF72 protein isoform localizes at the nuclear membrane in healthy neurons, with an apparent relocation at the plasma membrane in ALS motor neuron (94). Co-immunoprecipitation experiments also demonstrated that both long and short C9ORF72 isoforms interact with Ran and importin-1, suggesting that C9ORF72 protein isoforms could have a role in nucleocytoplasmic shuttling. Further evidence demonstrated that the HRE can physically bind to and sequester RanGAP1, which formed large perinuclear puncta in Drosophila HRE-expressing cells, in iPSC-derived neurons and in the motor cortex of *C9ORF72* ALS/FTD patients (95). Disrupting the interaction between RanGAP1 and HRE rescued NCT defects, suggesting the first possible mechanistic link between *C9ORF72* mutation and NCT dysfunction (95). Another study conducted in HRE-overexpressing fly models and in *C9ORF72* iPSC-derived neurons reported a direct connection between *C9ORF72* pathology and NCT defects including NPC disruption, RanGAP mislocalization and nuclear protein import inhibition (96).

The link between DPR toxicity and NCT defects emerged from a genetic screening in yeast which identified potent modifiers of DPR toxicity, including karyopherins and effectors of Ran-mediated NCT (97–99). Of note, transportin-1 was also identified as one of the strongest suppressors of toxicity in yeast and Drosophila models of poly(PR) pathology (97,99). Moreover, the DPR poly(PR)50 has been shown to increase the permeability of NPC (100). Taken together, these studies demonstrate that pathological *C9ORF72* HRE RNA as well as DPR-mediated toxicity can cause NCT defects both in cellular and animal models.

2.2.2. NCT defects and DNA damage linked to cytoskeletal alteration

Although NCT defects such as decreased NPC numbers, nuclear lamina disruption and impaired nuclear import rates have been extensively described in different ALS models, the causes and the consequences of such defects are not fully understood. In recent years, several studies have hypothesized a disease-relevant association between cytoskeletal structures and disruption of nuclear pore stability and function. Mutations in many

cytoskeletal-related genes are, in fact, causative of FALS, including actin-binding Profilin-1 (*PFN1*), Tubulin alpha-4A (*TUBA4A*) and *KIF5A* (101). In particular, *PFN1* mutations have been shown to cause subtle changes to actin polymerization, leading to reduced F-actin levels in motor neurons growth cones and reduced axonal outgrowth *in vitro* (102). Supporting this evidence, another work demonstrated that alterations to actin polymerization caused by mutant *PFN1* or Latrunculin A, a selective actin depolymerizing drug, in primary motor neurons and patient-derived cells lead to defects of nuclear morphology, lamin structure, localization of nucleoporins at the nuclear envelope and nuclear import rates. Furthermore, promotion of actin polymerization by pharmacological (i.e. Intramimic01 drug-IMM01-) or genetic induction of formins (i.e. GFP-mDia1) mitigates many of the defects observed in mutant *PFN1* cells and also in mutant *C9ORF72* patient-derived fibroblasts (103). Similarly, actin depolymerization via Latrunculin A treatment in healthy neurons disrupted the normal nucleocytoplasmic Ran gradient and RanGAP1 localization to the nuclear envelope, suggesting that modulation of actin can directly affect the NCT process. Although decreased levels of C9ORF72 protein have been found to be associated with reduced actin dynamics in iPSC-neurons (104), the mechanisms linking *C9ORF72* mutation to actin cytoskeleton defects, especially in post-mitotic neurons, is currently unknown. One suggested hypothesis is their association via the LINC complex, because it connects to both the cytoskeletal components from the cytoplasmic side and to the nuclear lamina from the nucleoplasmic side, transmitting the tensile force generated from the cytoskeleton or the extracellular environment to the nucleus to modulate nuclear morphology and function (105). Among nuclear mechanics alterations induced by actin modulation, DNA damage incidence and DDR have gained increasing interest. In particular, it has already been demonstrated that MCF-7 cancer cells treated with Latrunculin B and pectenotoxin-2, two actin-depolymerization drugs, displayed higher levels of DNA damage compared to untreated cells (106). To reinforce this idea, dos Santos et al. showed that cisplatin-treated cells grown on soft surfaces, where the nuclear tension is low due to reduced cytoskeletal forces, have lower levels of the DNA damage marker γH2AX (107). Overall, these data suggest an important effect of cytoskeleton alteration on nuclear changes, including DNA damage induction, even if the functional mechanisms, especially in post-mitotic motoneurons, are still unknown.

2.3. Axonal transport

Growing evidence suggests that axonal transport defects can impair neuronal homeostasis and lead to neurodegenerative diseases and motor neuron degenerations in ALS and HSP. The first evidence linking ALS pathogenesis to axonal transport defects revealed abnormal accumulations of phosphorylated neurofilaments (a pathological hallmark of neurodegenerative disorders), mitochondria and lysosomes in axons of post-mortem ALS motor neurons (108). Other studies reported a significant reduction in the anterograde transport (slow and fast) of cytoskeletal components and mitochondria in both mutant *SOD1* transgenic mouse (109–111) and in primary cortical neurons expressing mutant *SOD1* (111). Also TDP-43, which is actively transported along motor neuron axons (112), was shown to alter the stability of neurofilament light chain (NF-L) mRNA when mutated (113) and to impair the anterograde transport of ribonucleoprotein (RNP) granules (114). A very recent work demonstrated impaired microtubule-based transport in iPSC-motor neurons from *C9ORF72* patients, probably due to the association of arginine-rich DPRs with microtubules and motor proteins, as shown by interaction studies (115). Moreover, several cytoskeleton-related proteins have been associated to ALS pathogenesis, such as PFN1, Tubulin Alpha 4a (*TUBA4A*), neurofilament heavy subunit (*NEFH*) and peripherin (*PRPH*) (102,116–118). When also *KIF5A* was identified as a novel ALS causative gene (52), the evidence that a defective axonal transport might be implicated in ALS pathogenesis and might contribute to motor neuron death was reinforced, although the molecular mechanisms associated to different *KIF5A* mutations in ALS and HSP are still unclear.

2.3.1. KIF5A gene in axonal transport defects

Several works have already studied the functional consequences of the *KIF5A* variants differently localized in the gene and their association with ALS or HSP phenotype, in order to better elucidate the different pathomechanisms underlying *KIF5A*-related disorders.
Mutations in the C-terminal cargo-binding domain of *KIF5A* gene are causative of ALS (51,52) (see paragraph 1.5) and generate an aberrant KIF5A protein (*KIF5A* ΔExon27). A previous study conducted in zebrafish showed that the loss of KIF5A C-terminal cargo domain resulted in the disruption of axonal localization of mitochondria, suggesting a defective *KIF5A*-mediated transport (63). HEK293T cells and primary neurons overexpressing *KIF5A* ΔExon27 showed mutated KIF5A cytoplasmic aggregation which also had a dominant negative effect on the *wild-type* protein, thus preventing KIF5A function and triggering cellular toxicity. Moreover, *KIF5A* ΔExon27 accumulated in granules along

neurites and at plus-ends of microtubules of primary neurons overexpressing the mutant *KIF5A*, suggesting an aberrant motility of the protein and/or association of the mutant protein along microtubules (119,120). The same groups also demonstrated that ectopic expression of *KIF5A* ΔExon27 in Drosophila caused wing defects, motor impairment, paralysis and premature death (119,120). A very recent study confirmed these observations and demonstrated that *KIF5A* C-terminal mutant sequence relieved motor domain autoinhibition, increased motor self-association and led to drastically enhanced processivity on microtubules, thus displaying a toxic gain-of-function mechanism (60). The ALS phenotype associated to *KIF5A*-related mutations is consistent with classical ALS, but is associated with lower age of onset (around 46.5 years) and increased survival (nearly 10 years) (121). Mutations in the N-terminal motor domain of *KIF5A* gene are instead causative of the SPG10 form of HSP, so that *KIF5A* represents a genetic link in the phenotypic continuum between ALS and HSP diseases.

Functional alterations associated to N-terminal *KIF5A* mutations included both a decreased flux of cargo and a reduced velocity of the axonal cargo transport, probably due to a lower microtubule binding affinity, decreased microtubule gliding velocity, reduced ATP hydrolysis, impaired motor domain dimerization and altered order-disorder transition of the neck linker (which hampers the directionality and processivity of kinesin) (122). Overall, studies conducted in Drosophila and mouse models carrying *SPG10*-associated mutations support a loss of endogenous KIF5A function and a consequent disruption of axonal transport, leading to the formation of axonal swellings, synapse alterations, behavioral deficits, and increased mortality (64,123).

The association between the localization of *KIF5A* pathogenetic variants (motor vs cargo domain), their nature (missense vs loss-of-function variants) and the different clinical phenotypes associated (ALS vs SPG10) is currently not clear, but it is likely that both common and distinct mechanisms lead to *KIF5A*-dependent neurodegeneration.

3. Patient-derived cell models in ALS

3.1. Patient-derived induced Pluripotent Stem cells (iPSC)

The study of neurodegenerative disorders has always been hampered by the impossibility to obtain patient-derived neurons as suitable *in vitro* models. In the past years, different disease models have been used including animals, immortalized cell lines and human or murine primary cell cultures, each of which has its advantages and limitations. Patient-derived primary fibroblasts or peripheral blood mononuclear cells (PBMC) have revealed to be good *in vitro* models as they have the advantage of maintaining the patient's genetic background. However, they have the limit to be peripheral tissue cells, not representing the neuronal and glial cells affected in the neurodegenerative diseases.

The quite recent possibility to obtain human neurons from induced Pluripotent Stem Cells (iPSC) has completely changed the experimental approach to study neurodegenerative diseases and, in particular, motor neuron disorders. iPSC can be obtained from differentiated somatic cells (fibroblasts, PBMC) by the exogenous expression of four transcription factors Oct3/4, Sox2, Klf-4 and c-Myc to reprogram them back into an uncommitted and stem cell phenotype (124).

Given the possibility to obtain a partial reprogramming efficiency or the insertion of unwanted genetic variants, it is fundamental to characterize the newly reprogrammed iPSC for their morphology, expression of specific stemness and pluripotency markers, capacity to spontaneously differentiate into the three germ-layers cells and genome integrity (karyotype and, possibly, WES). Once generated, iPSC can be differentiated towards a more neural phenotype, such as the multipotent Neural Stem Cells (iPSC-NSC), or into multiple mature neuronal cell types, including motor neurons (iPSC-MN) and cortical neurons (iPSC-CN), and into glial cells (astrocytes, microglia, oligodendrocytes). iPSC and differentiated iPSC-neurons can therefore be used for disease modeling, drug screening or cell therapy with a personalized medicine approach. Compared to other non-human experimental models, they have the advantage of being obtained directly from patients carrying all their causative and risk factors. iPSCs can be genetically modified by gene editing technologies, such as CRISPR/Cas9, to generate the isogenic *wild-type* line, that represents the ideal experimental control, or to introduce a target mutation that needs to be studied, and to make cell therapy approaches and autologous transplantation more feasible.

An important advantage of iPSC-neurons is also represented by the possibility to make 2D co-cultures with other differentiated cell types, including glial cells and muscle cells, or to

generate of 3D organoids, thus mimicking the complexity of the human brain and the neuronal circuitry (125).

Nevertheless, iPSC and iPSC-neurons have some disadvantages and limitations that still need to be overcome. Firstly, the cost for their generation and handling is high and not always affordable. Moreover, the different iPSC reprogramming efficiency and the use of multiple protocols both for iPSC generation and differentiation lead to dissimilarities among laboratories or even among iPSC originated from the same donor sample. The use of standardized protocols and quality control processes are therefore highly needed (126). A further important limitation includes the difficulty to mimic the process of ageing and the environmental influence *in vitro*, two factors that are crucial in the etiology of neurodegenerative diseases such as ALS.

3.2. iPSC to study C9ORF72 and KIF5A-related pathomechanisms

A range of animal and cellular models have been developed to understand the pathological mechanisms underlying mutations in *C9ORF72* and *KIF5A* gene in ALS.

As regards *C9ORF72*, valuable insights have been obtained using C. elegans, Zebrafish, Drosophila and transgenic mice expressing three human BACs (Bacterial Artificial Chromosomes). All these mice developed RNA foci and DPR in the CNS, but they did not show any TDP-43 inclusion or neuronal loss, suggesting that their phenotype was not fully recapitulating all ALS or FTD pathological signs (127–129).

In this context, patient-derived iPSC-neurons and iPSC-motor neurons have the great advantage to derive from both FALS and SALS patients and to properly mimic the disease being the mutant *C9ORF72* gene expressed at physiological level. However, there is an open debate regarding the genomic stability of the HRE in *in vitro* cultures: the group of Almeida S (45) has shown that iPSC reprogramming or culturing could affect the stability of the repeat, while Cohen-Hadad Y et al (130) reported that the HRE is maintained stable in these cell models after reprogramming. In our lab we have evidence that HRE size is stable up to 40 passages *in vitro* although, given high somatic mosaicism of the original fibroblasts/PBMCs, it is possible to obtain iPSC clones with different HRE lengths from the same patient (*unpublished data*).

Almeida and colleagues were the first to utilize human iPSC from two patients with *C9ORF72* HRE to generate a neuronal cell population expressing the telencephalic marker BF1 (FOXG1) (45). They demonstrated that *C9ORF72* iPSC were able to efficiently differentiate into neurons similarly to *wild-type* controls, but they showed the presence of

RNA foci and DPR, thus recapitulating the pathological findings seen in *C9ORF72* ALS patients (45). Moreover, *C9ORF72* iPSC and iPSC-MN displayed the typical expression profile observed in blood, such as the decrease of the main isoform V2 and the increase of the V1 and V3 ones (45).

The use of iPSC and iPSC-neurons has helped to study several cellular pathways disrupted by *C9ORF72* mutation, such as NCT defects (see paragraph 2.2.1.), vulnerability to endoplasmic reticulum stress, oxidative stress, abnormal neuronal excitability, persistent glutamate-mediated excitotoxicity, DNA damage (see paragraph 2.1.1.) and axonal transport impairment (see paragraph 2.3) (66,131,132).

Since *KIF5A* was found to be a novel causative gene for ALS, the generation of patient-derived iPSC lines carrying different *KIF5A*-associated mutations has been recently reported (133,134). However, one recent study has also generated, by CRISPR/Cas9 gene-editing, an iPSC line with the ALS-related *KIF5A* mutation c.R1007K to perform functional studies (60). In particular, immunoprecipitation and mass spectrometry analysis showed that the ALS-mutated KIF5A alters the binding of several proteins involved in RNA transport, neuromuscular junction (NMJ) function and neurite outgrowth, which might in turn contribute to ALS pathogenesis (60). The same group also identified a mislocalization and an altered function of RBM24, an RNA-binding protein essential for cell fate decision and differentiation, because of its aberrant interaction with the mutant KIF5A protein (60). So far, the use of human iPSC has helped study the disease phenotype associated to ALS *KIF5A* mutations, but further studies on patient-derived iPSC-neurons are necessary to confirm the aberrant functions of mutated KIF5A observed in animal models and *in vitro* overexpression systems, as well as to decipher the different pathomechanisms associated to C-term mutations in ALS and to N-term mutations in SPG10.

3.3. iPSC to test therapeutic approaches for C9ORF72 pathology

Therapeutic approaches aimed at preventing the pathogenic effects caused by mutations in the main ALS genes *C9ORF72* and *SOD1* have already been developed. A way to treat genetically defined diseases is to target the mutant mRNA with antisense oligonucleotides (ASOs) that recruit enzymes, such as RNAse-H, to specifically degrade the pathological transcript. The first applications of ASOs in ALS were developed on the evidence that *SOD1* mutations cause neuronal death through a GOF mechanism (135). After years of experiments on animal models indicating improvement of neuromuscular function and decrease of mutated SOD1 protein in cerebrospinal fluid using ASOs, a phase III trial on

SOD1 mutated patients is now ongoing (VALOR SOD1-ALS trial; Biogen) (136). ASOs to knock-down pathological *C9ORF72* transcripts harboring the HRE have been subsequently developed and they have been demonstrated to reduce RNA foci number in *C9ORF72* iPSC-MN (95,137) and also DPR in *C9ORF72* BAC transgenic mice (127,138). Two different ASOs, WVE-004 and BIIB078, entered in phase I trial (NCT04931862) and phase I/II trial (NCT03626012), respectively. Unfortunately, BIIB078 tested by Biogen did not demonstrate any clinical benefits during the 6-month experimental period, and the research program was withdrawn (Biogen, 2022). The WVE-004 trial is still ongoing.

Another strategy used for *C9ORF72* is the use of chemical compounds that target the secondary structure of *C9ORF72* HRE-containing RNA to prevent the sequestration of nuclear RNA-binding proteins and splicing factors and/or RAN translation. Small molecules (i.e. 1a-CA-Biotin and DB1273) have been shown to efficiently reduce the production of RNA foci and toxic DPR aggregates in *C9ORF72* iPSC-neurons (139,140). Another tested strategy is gene silencing of the transcription elongation factor *SPT4*, which resulted in decreased levels of both sense and antisense *C9ORF72* HRE-containing transcripts and in an improvement of the disease phenotype in *C9ORF72* iPSC-neurons (141). Recently, Disney et al. have identified a potent, selective, and brain-penetrant small molecule which is able to directly interact with the pathological HRE, promoting the specific degradation of the intronic RNA sequence containing the HRE by native RNA quality control mechanisms (142). Elimination of the HRE-containing introns decreased the downstream pathology in *C9ORF72* iPSC-derived spinal neurons and in two *C9ORF72* mouse models (142). These results represent a significant advancement in the field of small molecules targeting *C9ORF72* pathological RNA, demonstrating that such molecules can be potentially designed to selectively degrade toxic RNAs in a mechanistically defined manner.

Nevertheless, it is fundamental to test novel molecules targeting the pathological RNA for their therapeutic long-lasting effects, especially in post-mitotic motor neurons, with the final aim to develop an effective treatment for ALS/FTD patients carrying *C9ORF72* mutations.

AIM OF THE THESIS

My PhD project had the objective to use patient-derived iPSC and iPSC-motoneurons as *in vitro* platforms to model ALS-related pathogenetic mechanisms and to test new personalized therapeutic strategies at pre-clinical level for ALS patients carrying *C9ORF72* gene mutation.

In particular in my work I addressed the following three specific aims:

1. To evaluate DNA damage and DNA damage response (DDR) associated to mutant *C9ORF72* gene in iPSC-neural stem cells and iPSC-motoneurons at different maturation stage, and to assess if there is a link between DNA damage, DDR and actin cytoskeleton dynamics.
2. To test the efficacy of a novel RNA-based therapeutic approach to reduce pathological RNA foci in *C9ORF72* iPSC-motoneurons by using a modified spliceosomal U1 small nuclear RNA (U1snRNA), already proved to be effective in mice models of Spinal Muscle Atrophy and Familial dysautonomia.
3. To establish a new patient-derived iPSC line carrying the novel mutation (p.R17Q) in *KIF5A* gene and its isogenic *wild-type* line by CRISPR/Cas9, in order to perform functional studies and elucidate the different pathomechanisms underlying *KIF5A*-related disorders.

MATERIALS AND METHODS

1. Reagents

Cell cultures reagents	
DMEM, high glucose medium	Gibco (Thermo Fisher Scientific)
DMEM/F-12	Gibco (Thermo Fisher Scientific)
Neurobasal™ medium	Gibco (Thermo Fisher Scientific)
Essential 8™ medium	Gibco (Thermo Fisher Scientific)
StemFlex™ medium	Gibco (Thermo Fisher Scientific)
Opti-MEM™ Reduced Serum Medium	Gibco (Thermo Fisher Scientific)
Fetal Bovine Serum (FBS)	Sigma-Aldrich
Amphotericin B	Gibco (Thermo Fisher Scientific)
Penicillin- Streptomycin 100X	Gibco (Thermo Fisher Scientific)
Sodium Pyruvate 100 mM	Gibco (Thermo Fisher Scientific)
hESC-Qualified Matrix	Corning
UltraPure™ 0.5M EDTA, pH 8.0	Gibco (Thermo Fisher Scientific)
Poly(2-hydroxyethyl methacrylate)	Sigma-Aldrich
KnockOut™ Serum Replacement	Gibco (Thermo Fisher Scientific)
L-Glutamine (200 mM)	Gibco (Thermo Fisher Scientific)
MEM Non-essential Amino Acid Solution (100×)	Gibco (Thermo Fisher Scientific)
2-Mercaptoethanol (50 mM)	Gibco (Thermo Fisher Scientific)
Matrigel Matrix Basement Membrane	Corning
PSC Neural Induction Medium	Gibco (Thermo Fisher Scientific)
StemPro™ Accutase™	Gibco (Thermo Fisher Scientific)
N-2 Supplement (100X)	Gibco (Thermo Fisher Scientific)
B-27™ Supplement (50X)	Gibco (Thermo Fisher Scientific)
Heparin sodium	Gibco (Thermo Fisher Scientific)
Trypsin-EDTA (0.25%), phenol red	Gibco (Thermo Fisher Scientific)
Bovine Serum Albumin (BSA)	Sigma-Aldrich
DNase I recombinant, RNase-free	Sigma-Aldrich
Poly-D-lysine hydrobromide	Sigma-Aldrich
GlutaMAX™ Supplement	Gibco (Thermo Fisher Scientific)
Y-27632 2HCl (ROCK inhibitor)	Selleckchem
SB 431542	Tocris Bioscience
SML0559 - LDN193189 hydrochloride	Sigma-Aldrich
Ascorbic acid (AA)	BDH Chemicals (VWR)
Retinoic acid = 98 HPLC	Sigma-Aldrich
SAG Supplier	Tocris Bioscience
Purmorphamine - Smoothened Receptor Agonist	Sigma-Aldrich
Recombinant human GDNF	PeproTech
Recombinant human CTNF	PeproTech
Recombinant human FGF	PeproTech
Recombinant human BDNF	PeproTech
Laminin, mouse	Corning
Doxycycline hyclate	Sigma-Aldrich

γ-Secretase Inhibitor XXI, Compound E	Merck Millipore
RevitaCell™ Supplement (100X)	Gibco (Thermo Fisher Scientific)
Other reagents	
TRIzol™ Reagent	Invitrogen (Thermo Fisher Scientific)
Chloroform	Carlo Erba
DNase I	Invitrogen (Thermo Fisher Scientific)
RNasin® Ribonuclease Inhibitor	Promega
Random primers	Invitrogen (Thermo Fisher Scientific)
dNTPs (Deoxynucleotide Triphosphates)	Invitrogen (Thermo Fisher Scientific)
Super Script II Reverse Transcriptase	Eurofins Genomics
Oligo(dT) primer	Invitrogen (Thermo Fisher Scientific)
GoTaq G2 DNA Polymerase	Promega
Agarose GellyPhor®	EuroClone
Midori Green Advance – nucleic acid stain	NIPPON genetics
SYBR Green qPCR Master Mix	Applied Biosystem
Paraformaldehyde solution in 4% PBS	Santa Cruz Biotechnology
Triton X-100	Sigma-Aldrich
PBS (10X), pH 7.4	Gibco (Thermo Fisher Scientific)
OmniPur® Dextran Sulfate Sodium	Calbiochem (Merck Millipore)
Formamide	IBI Scientific
Tween-20	Sigma-Aldrich
Amersham ECL rainbow molecular weight markers	Cytiva lifesciences
NuPAGE™ MOPS SDS Running Buffer (20X)	Invitrogen (Thermo Fisher Scientific)
Tris Buffered Saline	Santa Cruz Biotechnology
Normal Goat Serum (NGS)	Gibco (Thermo Fisher Scientific)
Methanol	Carlo Erba
FluorSave™ Reagent	Merck Millipore
Lipofectamine™ 2000 Transfection Reagent	Invitrogen (Thermo Fisher Scientific)
CytoTune®-iPSC 2.0 Sendai Reprogramming Kit	Invitrogen (Thermo Fisher Scientific)
Pierce BCA Protein Assay Kit	Thermo Fisher Scientific
Pierce™ ECL Western Blotting Substrate	Thermo Fisher Scientific
Amaxa Human Stem Cell Nucleofector	Lonza
Synthemax II-SC Substrate	Sigma-Aldrich
Synthetic sgRNA CRISPR kit	Integrated DNA Technologies
Alt-R S.p. HiFi Cas9 Nuclease V3	Integrated DNA Technologies
Alt-R HDR Enhancer	Integrated DNA Technologies
Molecules	
Neocarzinostatin from *Streptomyces carzinostaticus*	Millipore Sigma
Latrunculin B supplier	Tocris Bioscience
IMM01/mDia agonist	AxonMedchem

2. Samples supply

Skin biopsies and clinical data for this study were provided by the Neurology Unit at Istituto Auxologico Italiano (for ALS-*C9ORF72* and *wild-type* control patients) and Instituto Neurologico "Carlo Besta" (for HSP-*KIF5A* patient). The informed consent for research purpose was obtained from each participant according to the ethic committee of the respective Institute (Approval number 2022_03_15_12 for IRCCS Istituto Auxologico Italiano; Approval number 64 for IRCCS Instituto Neurologico "Carlo Besta").
Commercially available i^3-iPSC lines (one ALS-*C9ORF72* and one isogenic control) were acquired at Infinity BiologiX company by Professor Claudia Fallini and used in her lab at University of Rhode Island (USA). All the research has been performed in accordance with the Declaration of Helsinki and with relevant guidelines and regulations for the use of patient-derived cells.

3. Cell cultures

All the cell cultures are maintained at 37°C and at 5% CO_2 concentration.

Generation and maintenance of Induced Pluripotent Stem Cell (iPSC)

iPSC clones were obtained by reprogramming of primary fibroblasts collected from skin biopsies and cultured in DMEM high glucose medium with 20% Fetal Bovine Serum (FBS), 1 mM sodium pyruvate, 100 U/ml penicillin, 100 µg/ml streptomycin and 2,5 µg/ml amphotericin. At first passages $3X10^5$ fibroblasts were seeded in 6-well plates. When fibroblasts reached a confluence of approximately 40-60%, they were transduced using the CytoTune®-iPSC 2.0 Sendai Reprogramming Kit (Thermo Fisher Scientific) that uses a modified, non-transmissible form of Sendai virus to deliver and to transiently express the four Yamanaka factors (Oct3/4, Sox2, Klf-4 and cMyc). The day of reprogramming, the viruses were diluted according to manufacturer's instruction in fresh fibroblast medium that was then used to replace the spent medium. 24 hours after transduction (day 1), the medium was replaced with fresh fibroblast medium and cells were then cultured for 6 more days, replacing the medium every other day. At day 7, fibroblasts were split and plated in fresh fibroblast medium onto a new well of a 6-well plate pre-coated with iPSC Matrigel. The day after, the fibroblast medium was replaced with Essential 8 medium for the following 3-4 weeks, monitoring for the emergence of iPSC colonies. When emerged colonies reached the appropriate size, clones were picked and transferred onto new Matrigel pre-coated well

in E8 medium, where they were expanded for at least six passages. 80-90% confluence iPSC were split as follows: after the spent medium was removed and the well was washed with PBS, cells were incubated with EDTA 0.5 mmol/L solution for 4-5 minutes at room temperature (RT). The colonies were checked under a microscope and when they start to separate and round up, EDTA solution was removed. 1 ml of Essential 8 medium was added to the 6-well plate, gently pipetting cells up and down few times. Cells were splitted 1:10 and transferred onto a new iPSC Matrigel-coated 6-well plate with 2 ml of Essential 8 medium.
iPSC clones were therefore fully characterized for the expression of stemness markers (OCT3/4, SOX2, NANOG) and for their pluripotency to spontaneously differentiate into the three germ layers. Karyotype analysis was also performed to confirm the absence of chromosomal rearrangements. iPSC were subsequently differentiated or subjected to experiments.

iPSC in vitro spontaneous differentiation

To test the *in vitro* spontaneous differentiation of the established iPSC, embryoid bodies (EBs) were generated by gently resuspending iPSC colonies in HuES medium (DMEM/F12, 20% KnockOut serum replacement, 200mM L-Glutamine 1.5 %, 1% MEM Non-Essential Amino Acids solution, 100 U/ml penicillin, 100µg/ml streptomycin, 1% 2- Mercaptoethanol 1000X), with the addition of 20ng/ml Rho-associated kinase (ROCK) inhibitor Y27632 (20μM) and fibroblast growth factor (FGF) (Peprotech) to promote single cell survival. iPSC were plated onto a 60 mm low-adhesion Petri dish pre-coated with 10 mg/ml poly-HEMA to further promote cell suspension growth. The poly-HEMA coating was performed as follows: poly-HEMA was diluted in 96% ethanol pre-heated at 56 °C, the solution was filtered, distributed in the dish and let evaporate under the hood for approximately 3 hours.
At day 7, EBs were collected and plated on Matrigel-coated 24 multi-well coverslips in Essential 8 medium. The medium was changed every day until the EBs started to spontaneously differentiate. Expression of the three germ layers specific markers was evaluated by immunofluorescence (alpha-fetoprotein for endoderm, desmin for mesoderm and βIII tubulin for ectoderm).

Gene-editing by CRISPR/CAS9

CRISPR/Cas9 system was used to correct the *KIF5A* mutation into a *wild-type* sequence using recombinant Cas9 protein and RNA guides (all provided by Integrated DNA

technologies-IDT). The gRNA sequence used was GAGAAACTTTTCAATGCGTT TGG, targeting a region in the first intron of *KIF5A* gene containing the mutation c.50G>A.
We used the following single-stranded oligo donor (ssODN) sequence to introduce the *wild-type* KIF5A sequence (c.50G):
AGACCAACAACGAATGTAGCATCAAGGTGCTCTGTCGATTCCGGCCCCTGAACCAGG CTGAGATTCTGCGGGGAGACAAGTTC.
The first day, iPSC were split with PBS/EDTA in wells of a 6-well plate as previously described. The day after, iPSC at about 50% confluence were washed with PBS and incubated with Accutase for 5 minutes at 37 °C. The Accutase was then neutralized with Neurobasal medium and cells were counted. 800.000 cells were placed into a new tube and centrifuged for 5 minutes at 500 rpm. The supernatant was removed and the cell pellet was resuspended in the nucleofection solution, composed by 18 ul of Supplement Solution 1 and 82 ul of Solution 2. This mix was then transferred into a tube containing the RNP complex solution, which was previously incubated at RT for 45 minutes and was composed of 16 ug of synthetic sgRNA, 20 ug of Alt-R HiFi Cas9 nuclease V3, 4 uM of Eletroporation Enhancer and 200 pmol of single-stranded oligodeoxynucleotides Alt-R ssODN (used as donor template). The iPSC solution mix was then placed into the proper cuvette and a specific program for iPSC transfection in the Amaxa nucleofector was set. The nucleofected cells were cultured into one Matrigel-coated well of 6-well plate in StemFlex medium and 3 nM Alt-R HDR enhancer (IDT) was added, in order to improve transfection efficiency. Cells were then incubated at 32 °C, 5% CO_2 for 48 hours, and then at 37 °C for the rest of the protocol. 24 hours after nucleofection, the media was replaced with fresh StemFlex medium, then the medium was changed every other day until day 10. At day 11, iPSC colonies were detached with Accutase as previously described, and a clonal dilution was performed to obtain single cells. Single iPSCs were plated into a Cell Bind surface 100 mm culture dish previously coated with Synthemax II-SC substrate (Corning) for 24 hours at 37 °C and Revitacell was added to StemFlex medium in order to promote single cell survival. The medium was then changed every other day until day 21. When colonies reached approximately 1 mm of diameter, they were ready to be picked. Single colonies were picked at approximately day 22, transferred into 96 multi-well U-bottom plate, triturated and then placed into 96-multi well flat-bottom plate previously coated with iPSC-matrigel. They were let grown until they reached confluence, then they were detached both for being analyzed with Sanger sequencing and for being further expanded.

Differentiation and maintenance of iPSC-Neural Stem Cells (iPSC-NSC)

iPSC-Neural Stem Cells (iPSC-NSC) differentiation was performed using the iPSC Neural Induction Medium protocol (Gibco). At day 0, iPSC were plated at 15-25% confluence onto iPSC-Matrigel pre-coated wells. After 24 hours (day 1), the medium was replaced with Neural Induction Medium (NIM), composed by 98% of Neurobasal medium and 2% of Neural Induction Supplement (Gibco), and it was then replaced again at days 3, 4 and 5. At day 7, iPSC-NSCs were detached with Accutase, centrifuged and plated onto iPSC-Matrigel pre-coated wells in Neural Expansion Medium (NEM), composed by 49% of Neurobasal medium, 49% of Advanced DMEM/F-12 and 2% of Neural Induction Supplement. The medium was replaced twice a week and cells were expanded for at least six passages before being characterized or subjected to experiments.
80-90% confluence NSC were split as follows: after the spent medium was removed and the well was washed with PBS, cells were incubated with Accutase for 5 minutes at 37 °C. The Accutase was then neutralized with Neurobasal medium and cells were centrifuged for 5 minutes at 500 rpm. The surnatant was removed and the cell pellet was resuspended in Neural expansion medium, pipetting cells up and down to obtain single cells. Cells were splitted 1:10 and transferred onto a new iPSC Matrigel-coated 6-well plate with 2 ml of Neural Expansion Medium.
To characterize NSC, cells were plated onto iPSC-Matrigel pre-coated glasses in wells of a 24-well plate and subjected to immunofluorescence staining. For neocarzinostatin (NCS) treatment, cells were plated at a density of 70’000 cells/well and treated with NCS the day after.

Differentiation and maintenance of iPSC-motoneurons (iPSC-MN)

iPSC-motoneurons (iPSC-MN) were differentiated from iPSCs using a modified protocol from Amoroso (143), that included the formation Embryoid Bodies (EBs) and their subsequent dissociation and differentiation with specific factors.
In detail, iPSC were plated onto a 100 mm low-adhesion Petri dish pre-coated with 10 mg/ml poly-HEMA and cultured in HuES medium (day 0), as previously described. To replace the medium, EBs were collected with a pasteur pipette, centrifuged at 300 x g for 3 minutes and then re-plated onto the same dish. The medium was changed as follows:

- day 1: medium replacement with HuES with addition of 20 ng/ml bFGF, 20 μM ROCK inhibitor, 10 μM SB431542 and 0,2 μM LDN193189, to induce neuralization

- day 2: addition of 20 ng/ml bFGF and 20 μM ROCK inhibitor to the medium, without replacing it
- day 3: medium replacement with the same medium as day 1
- day 4: medium replacement with NIM, composed of DMEM/F12, 1% L-glutamine, 0,1% Penicillin 10.000 U/ml and streptomycin 10 mg/ml, 1 % MEM Non-Essential Amino Acids solution, 2 μg/ml heparin, 1% N2 supplement with addition of 20 μM ROCK inhibitor, 10 μM SB431542, 0,2 μl LDN, 10 ng/ml brain-derived neurotrophic factor (BDNF) and 0,4 μg/ml ascorbic acid (AA)
- day 7: medium replacement with the same medium as day 4, but with the addition of 1 μM retinoic acid (RA)
- days 9/11/14/16/18: medium replacement with NIM with addition of 20 μM ROCK inhibitor, 10 ng/ml BDNF, 0,4 μg/ml ascorbic acid (AA), 1 μM retinoic acid (RA), 1 μM smoothened agonist (SAG), 0,5 μM purmorphamine (Pur)

At day 21, EBs were collected and incubated with pre-heated 0.05% trypsin to disgregate EBs, obtaining only the external ectodermal cells. 2 ml of FBS and 4 ml of pre- heated wash buffer CTWM (composed by 25 mM glucose, 0,1% BSA, 2% B27 supplement, 1% N2 supplement, 2 mM MgCl2, EDTA 1:1460, FBS 1:40, DNase 1:1000) were then added and the solution was centrifuged at 1000 x g for 5 minutes. The pellet was resuspended in 3 ml of wash buffer: the big cellular aggregates were let sediment, while the supernatant was transferred into a new tube and centrifuged at 1000 x g for 5 minutes. The obtained cellular pellet was resuspended in Neural Differentiation Medium (NDM), composed of Neurobasal Medium, 1% L-glutamine 200mM, 0.1% Penicillin 10.000 Units/ml and 10 mg/ml streptomycin, 0.1 mM MEM NEAA, 1% N2 supplement with the addition of 20 μM ROCK inhibitor, 10 ng/ml BDNF, 0,4 μg/ml AA, 1 μM RA, 1 μM SAG, 2% B27, 1 μg/ml laminin (lam), 25 μM glutamate (Glu), 1X β-mercaptoethanol, 10 ng/ml glial-derived neurotrophic factor (GDNF), 10 ng/ml ciliary neurotrophic factor (CTNF).

20’000 cells per wells of a 24-well plate and 90’000 cells per well of a 6-well plate were plated in wells pre-coated with Poly-D-lysine (50 μg/ml)/PBS for three days and laminin (15/μg)/PBS for 1 hour at 37° C.

At days 23, 25, 28, 30, 32 half of the medium was replaced with NDM with addition of 0,4 μg/ml AA, 2% B27, 1 μg/ml lam, 25 μM glu, 10 ng/ml GDNF and 10 ng/ml CTNF. iPSC-MN were then analyzed at day 13 and 33 from EBs dissociation.

Differentiation and maintenance of iPSC-cortical neurons (iPSC-CN)

iPSC-cortical neurons (CN) were differentiated from already available i^3- iPSC (integrated, inducible, isogenic), obtained by CRISPR/Cas9 mediated DNA integration of the cortical dopaminergic differentiation factor neurogenin2-NGN2 (pUCM-AAVS1-TO-hNGN2, plasmid #105840, Addgene) into a safe-harbour locus in the genome. The expression of NGN2 can be induced by doxycicline and in only 14 days is possible to obtain functionally mature glutamatergic cortical neurons, making this differentiation rapid and one-step (144).
At day 1, hIPSC were washed with PBS and then incubated with PBS/EDTA solution for 10 minutes to obtain single cells. When the cells began to detach, DMEM/F12 medium was added into the well and cells were triturated 3-4 times. 1X106 cells per 100 mm well plate were counted, transferred into a 15 ml conical tube and centrifuged for 5 minutes at 300 g. After centrifugation, cells were resuspended in 2 ml of StemFlex medium with 10 uM of ROCK inhibitor and then placed into a 100 mm well plate previously coated with iPSC-matrigel. 24 hours later, the medium was replaced with induction media (IM), which was composed by DMEM/F12, 1% N2 supplement, 1% MEM Non-Essential Amino Acids solution, 1% GlutaMax with the addition of 10 nM ROCK inhibitor, 2 ug/ml Doxycycline and 0,2 uM Compound E. At day 3, differentiated cells were checked under an inverted microscope and half of the medium volume was replaced with fresh IM media. The day after, partially differentiated cells were transferred to motor neurons culture conditions: cells were detached with 2 ml of Accutase and then triturated with 10 ml of PBS 4-5 times, to obtain single cells. The cell solution was passed through a 40 um cell strainer to ensure full dissociation and then centrifuged 5 min at 500 x g. The supernatant was discarded, and the cell pellet was resuspended in freshly made IM media. 250'000 cells were plated in pre-coated Poly-Lysin/Laminin glass into wells of 12-multi well plate. 24 hours later, IM media was changed with motoneuron media (CNM), which was composed by Neurobasal media, 2% B27 supplement, 1% N2 supplement 1:100, 1% MEM Non-Essential Amino Acids solution and 1% GlutaMax with the addition of 1ug/ml Laminin. Half of MN media was then changed every two days until day 13, when cells were subjected to treatments with actin-modifier drugs and/or Neocarzinostatin.

iPSC-MN infection

Third generation lentiviruses containing GFP-tagged U1C or U1G sequence were provided by Franco Pagani at ICGEB in Trieste (*sequence under patent*). The obtained viral title (TU/ml) corresponded to $1X10^9$ TU/ml.

At day 47 of MN differentiation, *C9ORF72* iPSC-MN were infected with the GFP-U1-C/G lentiviruses: NDM medium was replaced with 300 μL of fresh medium and the viruses were directly added into the well. $2X10^7$ TU/ml was used to infect 60'000 iPSC-MN per wells of a 24-well plate, and $5X10^7$ TU/ml to infect 150'000 iPSC-MN per well of a 6-well plate. 24 hours later, the medium was completely removed and replaced with fresh NDM medium. After four days, cells were checked for the integration of the viruses through the fluorescent expression of GFP, then fixed and analyzed for FISH.

HEK293T cell

The human embryonic kidney 293 (HEK293) cell line was cultured in DMEM high glucose supplemented with 10% fetal bovine serum (FBS), 1 mM sodium pyruvate, 100 U/ml penicillin, and 100 μg/ml streptomycin. Cells were mechanically detached and seeded at a concentration of 10^5 cells/mm^3 every three days. For each experimental condition, 60.000 cells were plated in duplicate in 24-well plates and transfected with plasmid DNA as following described.

HEK293T cell transfection

Transient transfections were performed with Lipofectamine Plus reagent following manufacturer instruction (Invitrogen). Briefly, 0,7 μg of plasmid DNA were incubated 15 minutes at RT with 2 μl of Lipofectamine Plus, using OptiMEM medium. The DNA/Lipofectamine solution was then added to sub-confluent HEK cells (around 60%) cultured in complete medium without antibiotics. Cells were fixed 24 hours after transfection to perform the following experiments.

Cell treatment

Cell treatment with neocarzinostatin (NCS, Sigma) was performed as follows: the spent medium was replaced with the appropriate fresh medium (NEM for NSC, NDM for MN, CNM for CN, DMEM for HEK cells) in which NCS was diluted at a final concentration of 50 ng/ml. Cells were exposed to NCS for 20 minutes, at the end of which they were either analyzed by IF or subjected to rescue experiments. Rescue experiments were performed replacing the media containing NCS with fresh media and restoring normal cell growth conditions for different time frames (4, 6, 8, 10 or 24 hours), at the end of which cells were fixed and analyzed by IF.

HEK cells and iPSC-CN were treated with actyin-modifier drugs in basal condition or after 20 minutes of exposure to NCS: the medium containing NCS was replaced with fresh medium containing Latrunculin B or Intramimic drug diluted at a final concentration of 0,5 μM and 0,1 μM, respectively. After 6 hours, cells were fixed and analyzed by IF.

4. RNA analysis

RNA extraction and quantification

The dried cell pellet was resuspended in 1 ml of TRIzol and incubated at RT for 5 minutes to lysate it. 100 µl of 100% chloroform per 500 µl of TRIzol was added, mixed and incubated for 3 minutes. After centrifugation at 12'000 x g at 4 °C for 30 minutes, three phases were visible: an upper aqueous phase containing the RNA, an intermediate phase containing the denatured proteins and a lower phenol-chloroform phase containing soluble proteins and DNA.
The aqueous phase was collected and RNA was precipitated by incubating samples with 250 µl of 100% isopropanol per 500 µl of TRIzol and with 1 µl of glycogen for 20 minutes at -80 °C. Subsequently, the sample was centrifuged at 12'000 x g for 30 minutes at 4°C, the supernatant was discarded and 1 ml of cold 75% ethanol was added to wash the RNA pellet. The sample was then centrifuged again at 7500 x g for 10 minutes at 4°C, the supernatant was removed and the RNA dry at RT. RNA was finally resuspended in an appropriate volume of DEPC H_2O and stored at -80°C. Nanodrop instrument was used to perform the RNA quantification.

Reverse transcription PCR (RT-PCR)

The extracted and quantified RNA was retrotranscribed into complementary DNA (cDNA) through a three steps process: DNA removal, RNA retro-transcription into cDNA and cDNA amplification.
4 µl of a solution composed by 3 µl of First Strand Buffer 5x, 0,5 µl of DNAse and 0,5 µl of ribonuclease inhibitor (RNAsin) were added to the RNA to perform the DNA removal. H_2O was added to reach a final volume of 15 µl. The sample was then run at the thermocycler with the following program: 20 minutes at 37°C and 2 minutes at 94°C.
The samples were then incubated with 13 µl of a solution composed by 3 µl of First Strand Buffer 5x, 3 µl of 0,1 M dithiothreitol (DTT), 1 µl of Random Primers 200 ng/µl, 1,5 µl of deoxynucleotide triphosphates (dNTPs), 0,5 µl of RNAsin and 4 µl of H_2O for 10 minutes at

RT. 1 µl of Super Script II Reverse Transcriptase and 1 µl of oligoDT were then added and the sample was run at the thermocycler for 40 minutes at 42°C and 15 minutes at 70°C, to retro-transcribe the RNA. The cDNA was amplified by incubating the sample with a mix composed by 1x buffer, 0,3 mM dNTPs, 1,25 µM Forward primers, 1,25 µM Reverse primers (**Table 1**) and 0,025 U/µl Taq polymerase (GoTaq G2 DNA Polymerase, Promega). The sample was run at the thermocycler with the protocol in the **Scheme 1**.

Gene	Forward primer	Reverse primer
ChAT	TGAGTACTGGCTGAATGACATG	AGTACACCAGAGATGAGGCT
hRPL10	CAAGAAGCTGGCCAAGAAGTATG	TCTGTCATCTTCACGTGAC

Table 1: Primers used for step 3 RT-PCR

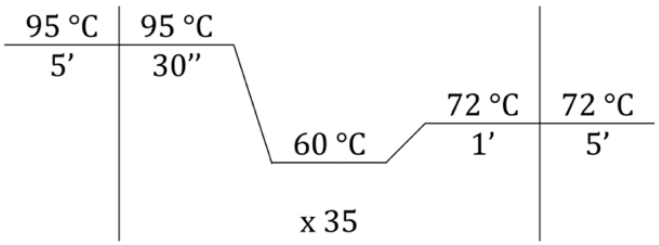

Scheme 1: Protocol used for RT-PCR step 3

Agarose gel electrophoresis

Agarose gel electrophoresis was performed on a 1,5% agarose gel prepared in TAE (Tris-acetate-EDTA) 1x buffer and using 5 µl of Midori Green Advance per 50 ml of gel, a commercial nucleic acid stain. The electrophoretic run was performed at 100 mV, using a 100 bp marker. The gel bands were visualized at the transUV illuminator.

Quantitative real-time PCR (qPCR)

Quantitative real-time PCR was performed loading on a MicroAmp Fast 96-weel reaction 50ng/µl of cDNA to 23 µl of a mix composed by 8,5 µl of H2O, 0,75 µl of Oligonucleotide Forward 10 uM, 0,75 µl of Oligonucleotide Reverse 10 uM and 12,5 µl of SybrGreen 2x (an asymmetrical cyanine dye able to bind to double stranded DNA). The plate was closed with the MicroAmp Optical Adhesive Film and run at the thermocycler with the protocol shown in **Scheme 2**. The oligonucleotides used are depicted in **Table 2**. The results were analysed by normalizing the mean cycle threshold (Ct) against the internal control (Ct of the gene of

interest – Ct of internal control RPL10) and then against the isogenic sample (Ct of the sample of interest – Ct of the isogenic sample) obtaining the ΔCt. The ΔΔCt was calculated as follows: $2^{-\Delta Ct}$.

Gene	Forward primer	Reverse primer
KIF5A	CAGAGACTGAGCACCTGTCCTCC	GGGGAAGAGGATGAAGGATGAGC
Sox2	TTGCGTGAGTGTGGATGGGATTGGTG	GGGAAATGGGAGGGGTGCAAAAGAGG
Oct3/4	GACAGGGGGAGGGGAGGAGCTAGG	CTTCCCTCCAACCAGTTGCCCCAAAC
Nanog	CAGCCCTGATTCTTCCACCAGTCC	GTTCTGGAACCAGGTCTTCACCTG

Table 2: oligonucleotides used in qPCR

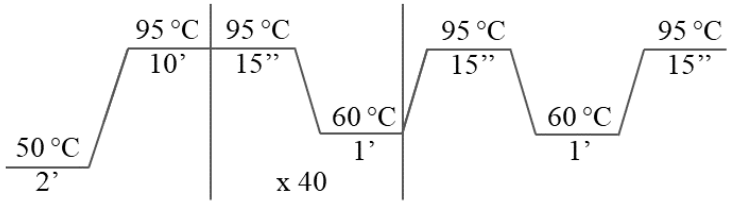

Scheme 2: Protocol used for qPCR

Fluorescence in situ hybridization (FISH)

Fluorescence In Situ Hybridization (FISH) was performed in a RNAse free-environment and using sterile material, in order to preserve RNA integrity. Cells plated onto glasses in wells of a 24-well were washed twice for 5 minutes with 1X PBS, they were fixed with 300 µl of 4% paraformaldehyde at dark for 20 minutes and then washed again twice for 5 minutes with 1X PBS. Cells were permeabilized with 500 µl of 0,2% Triton for 10 minutes and then washed twice for 5 minutes with 1X PBS. After being dehydrated with 70% ethanol, they were transferred into a desiccant chamber with drierite. Non-specific sites were blocked with 200 µl of hybridization buffer (composed by 10% SSC 20X, 5% sodium phosphate 1X, 10% dextran sulfate and 50% formamide) at 66° C for 1 hour in a humid incubation chamber containing saline-sodium citrate 2x (SSC), to prevent buffer evaporation. Hybridization was performed using a 30 nM 5′ TYE-563-labelled locked nucleic acid (LNA) (CCCCGG)3 probe complementary to the sense RNA foci containing the GGGGCC-repeats (Exiqon Qiagen). The probe was denatured at 80° C for 75 seconds and it was then maintained in ice at dark for 75 seconds. It was then diluted in 200 µl per well of hybridization

buffer and vortexed for 20 seconds. Glasses were incubated with hybridization buffer containing the probe in the incubation chamber containing SSC 2X at 66° C overnight. The following day, glasses were washed once for 5 minutes with 500 µl of Wash I solution, composed by 90% DEPC H_2O, 10% SSC 20X and 0,1% Tween-20, and then four times for 10 minutes at 65° C with 500 µl of Wash II solution, composed by 99,5% DEPC H_2O and 0,5% SSC 20X. Nuclei were stained with 500 µl of DAPI for 10 minutes and glasses were then washed three times with DEPC H_2O for 5 minutes. They were dehydrated as previously described and they were finally mounted on microscope slides.

5. Immunofluorescence

Cells plated onto glasses in wells of a 24-well plate were washed twice for 5 minutes with PBS 1X, fixed with 300 µl of paraformaldehyde 4% for 20 minutes at dark and then washed twice with PBS 1X for 5 minutes.

To visualize the mitochondria, cells were previously incubated for 15 minutes at dark with Mitotracker Red CMX Ros 1 mM (excitation wavelength range 579/599), diluted in Neurobasal medium to a final concentration of 10 nM. The medium containing Mitotracker was then removed and cells could be either analysed through time-lapse imaging or they could be fixed for immunofluorescence.

The immunofluorescence procedure started by washing cells plated onto glasses in wells of a 24-well twice for 5 minutes with 300 µl of a solution composed by PBS 1X and 10% Normal Goat Serum (NGS) (PBS-NGS). The cells were then permeabilized with 300 µl of cold 100% Methanol (-20°C) for 5 minutes and then with 300 µl of a solution composed by PBS-NGS 10% and Triton 0,3% for 5 minutes. Non-specific sites were blocked with 300 µl of PBS-NGS 10% for 20 minutes. Subsequently, the cells were transferred into a humid chamber to prevent antibody evaporation and were incubated with 60 µl of the chosen primary antibody diluted at the required concentration (**Table 3**) in PBS-NGS 10% at 37°C for 90 minutes. After the incubation with primary antibody, glasses were washed twice with PBS-NGS 10% for 5 minutes and then incubated for 45 minutes at dark with 300 µl of the proper secondary antibody diluted at the required concentration (**Table 4**) in PBS-NGS 10%. After this phase, the cells underwent a series of 5 minutes long washes at dark: two with 300 µl of PBS-NGS 10%, two with 300 µl of PBS 1x and two with 300 µl of distilled H_2O. Nuclei were stained by incubating them with 300 µl of DAPI for 10 minutes and glasses were then washed once for 5 minutes with 300 µl of H_2O. They were then mounted on microscope slides using 7 µl of FluorSave Reagent.

Primary Antibody (Abl)	Specie	Dilution
53-BP1 (*53BP1 Antibody #4937, Cell Signaling*)	rabbit	1:1000
γH2AX (*Anti-phospho-Histone H2A.X (Ser139) Antibody*, *clone JBW301, Sigma-Aldrich*)	mouse	1:800
Nestin (*Anti-Nestin Antibody*, clone 10C2, *Chemicon)*	mouse	1:100
Alkaline phosphatase (*Alkaline phosphatase, ab108337 Abcam*)	rabbit	1:250
SSEA-4 (*SSEA4 monoclonal antibody, eBioMC-813-70, eBioscience™*)	mouse	1:100
TRA-1-60 (*TRA-1-60, Podocalyxin, monoclonal, eBioscience™*)	mouse	1:125
βIII-tubulin (*Anti-beta III Tubulin antibody [EP1569Y], ab52623 Abcam*)	rabbit	1:500
HB9 (*monoclonal, DSHB, NIH*)	mouse	1:100
MAP2 (*monoclonal*, *MAB3418 Chemicon*)	Mouse	1:100
SMI-312 (*SMI-312 antibody, monoclonal, SIG-32248 Covance*)	mouse	1:1000
KIF5A (*KIF5A antibody, polyclonal, A3303 Abcloncal*)	rabbit	1:100

Table 3: Primary antibodies used for IF experiments

Secondary Antibody (Ab II)	Specie	Dilution	Absorbance	Emission
M488 (*Alexa Fluor™ 488 goat anti-mouse IgG (H+L)*, *Life Technologies*)	mouse	1:500	488 nm	500 nm
R488 (*Alexa Fluor™ 488 goat anti-rabbit IgG (H+L)*, *Life Technologies*)	rabbit		488 nm	500 nm
M555 (*Alexa Fluor™ 555 goat anti-mouse IgG (H+L)*, *Life Technologies*)	mouse		561 nm	570 nm
R555 (*Alexa Fluor™ 555 goat anti-rabbit IgG (H+L)*, *Life Technologies*)	rabbit		561 nm	570 nm

Table 4: Secondary antibodies used for IF experiments

6. Protein analysis

Protein extraction and dosage

The dried cell pellet was resuspended in 20 µl of lysis buffer composed by 20 mM of Tris-HCl pH 7,5, 150 mM of NaCl, 1 mM of EDTA, 1 mM of EGTA, 1% Triton and H_2O, then it was sonicated 5 times for 10 seconds while being kept on ice.
Pierce BCA Protein Assay Kit was used to quantify the extracted proteins. A standard curve of absorbance was created using a series of solutions with known dilutions of albumin and 10 µl of each were loaded on a 96-well plate. 9 µl of H_2O and 1 µl of sample were then loaded onto the plate. 200 µl of a standard working solution composed by the reagents A and B of the kit (50:1) were added in each well. The plate was covered by parafilm and silver foil and incubated at 37°C for 30 minutes. The plate was then analysed at the spectrophotometer.
The concentration of the sample (µg/µl) was then calculated interpolating the obtained absorbance of the sample protein with the known absorbance of the standard curve.

Western Blot

The desired quantity of extracted protein (ug) was diluted with Loading buffers (1x, 2x and 3x) and DTT 1 M and then incubated at 99 °C for 10 minutes.
The marker (Full Range Rainbow) and samples were loaded on a 3-8% or 10% (based on the molecular weight of interest) polyacrylamide gel. Tris-acetate 1X or MOPS (3-N-morpholino propanesulfonic acid) 1X were used as running buffers. Electrophoresis was performed at 120 mV for approximately 1.5 hours.
Gels were then transferred to a nitrocellulose membrane using iBlot (Invitrogen). The membrane was incubated with 5% milk in TBST (Tris Buffered Saline + 0,1% Tween) buffer or in 5% BSA (Bovine Serum Albumin) in TBST for 1 hour at RT to block the unspecific protein binding sites. The membrane was then incubated overnight at 4°C with the primary antibody diluted at the required factor (**Table 5**) in 5% BSA/TBST or milk/TBST.
The membrane was washed 4 times with TBST for 5 minutes and incubated 1 hour with the horse-radish peroxidase (HRP)-conjugated secondary antibodies, diluted at the required factor (**Table 6**) in 5% BSA/TBST or milk/TBST. The membrane was washed 4 times with TBST for 5 minutes.

Signals were detected with Western Enhanced Chemiluminescence (ECL) Substrate (containing HRP substrate) 5 minutes at dark, and X-ray films exposed for different times (1 minute-45 minutes) depending on the primary antibody.
Densitometric analyses of the bands were performed with the QuantityOne software. Bands intensities were normalized against the background noise of the film. The primary and secondary antibodies used are listed in table.

Primary Antibody (Abl)	**Specie**	**Dilution**	**WB Molecular weight**
KIF5A	Rabbit	1:500	130 kDa
Tubulin	Mouse	1:1000	52 kDa

Table 5: Primary antibodies used for Western Blot experiments

Secondary Antibody (Abll)	**Specie**	**Dilution**
Anti-mouse (*Anti-mouse IgG, peroxidase antibody, goat, A9309 Sigma)*	mouse	1:20000
Anti-rabbit (*Anti-rabbit IgG, HRP-linked antibody, goat, 7074S Cell Signaling)*	rabbit	1:2000

Table 6: Secondary antibodies used for Western Blot experiments

7. Image acquisition and analysis

Confocal microscopy

The confocal microscope A1R FRET FLIM with a 60x oil-immersion objective was used to acquire the images.
The DAPI signal was acquired using a 408 nm laser, the fluorophore 488 signal with a 488 nm laser and the fluorophore 555 signal with a 561 nm laser. The images were acquired with a scanning velocity of 1/16 pixel/second and a resolution of 1024-pixel. A Z-stack mode was used for the acquisition of the images, taking approximately 10 stacks with a distance of 0,5 μm among them. A minimum of 5 images from different fields were taken for each glass.

Immunocytochemical image analysis

The ImageJ software was used to analyse the acquired images. Different analyses have been performed:

- % of γH2AX DNA damage foci+ cells and medium number of DNA damage foci. The multiple stacks of each channel were firstly summed to each other, and cell nuclei were then selected as region of interests (ROI). The number of γH2AX and 53BP1 foci in the selected ROI was quantified using the "Find Maxima" function, setting a prominence value for each experiment.
- % of *C9ORF72* foci+ cells and medium number of *C9ORF72* foci. The multiple stacks of each channel were combined to each other using the maximum intensity criterion. Channels were split and the one corresponding to RNA foci was binarized using the "Adjust Threshold" function, by selecting an appropriate threshold value for each experiment. The number of RNA foci was quantified using the "Analyze Particles" function, with parameters of size and circularity set at 0,05-100 and 0-1, respectively.
- Mean fluorescence intensity. The multiple stacks of each channel were combined to each other using the sum slices criterion. For the DNA damage analysis, the mean fluorescence intensity was quantified on the selected ROI using the "measure" function. For the KIF5A analysis, the mean fluorescence intensity signal was measured on specific segments areas of the neurons. The "Rectangle" function was used to select a defined area of the neurites, which was measured with the "Measure" function.
- Mitochondrial morphology and density. The multiple stacks of each channel were combined to each other using the maximum intensity criterion. The "Segment line" function, with a width of 15, was used to select the segments of interest. The "Line to area" function allowed to obtain an area and the "Measure" function quantified the selected area. The channels were split and the channel corresponding to mitochondria was binarized using the "Adjust Threshold" function, setting the appropriate threshold. The mitochondria were analysed using the "Analyze particles" function, setting the size as 5-infinity, whose output included the particle counting and the total area occupied by the particles. Moreover, the area, the mean fluorescence intensity, the major (width) and the minor (height) parameter were given for each particle. The analysis was performed to determine the aspect ratio (width/height) and the mitochondrial density (mitochondrial area/segment area).

Live imaging acquisition and analysis

The confocal microscope Nikon Eclipse Ti with a 20x objective was used to perform the live imaging. The cells chamber conditions were set at 5% CO_2, 37 °C, 95% RH. Two image frames were acquired every 3 minutes.
For cells plated on 35 mm FluorDish with glass bottom cover, a minimum of 5 images from different fields were taken.
The ImageJ software was used to analyse the acquired images. The "Segmented line" function, with a width of 15, was used to select segments of interest. The "MTrackJ" plugin was used to perform the analysis: using its "Add" function every single mitochondrial particle is marked and then analysed through the "Measure" function, whose output included the minimum velocity (micron/second), maximum velocity (micron/second) and mean velocity (micron/second).

8. Statistical analysis

Statistical analysis of data was performed using the GraphPad Prism software 9.0. Statistically significant differences were determined using the student's t-test (to compare two groups), the One-way ANOVA or Two-way ANOVA test (to compare two or more groups with one or more variables, respectively). Results were considered significative when p-value was <0,05. The statistical tests that were applied for each experiment and sample replicates are indicated in each figure.

RESULTS

1. DNA damage and DNA damage response in *C9ORF72* mutant patient-derived iPSC

1.1. Generation and characterization of C9ORF72 iPSC

The first aim of our study was to investigate DNA damage and DNA damage response (DDR) in mutant *C9ORF72* patient-derived iPSC.

To address this issue, iPSC lines from fibroblasts of 2 *C9ORF72* patients (C9#1, C9#2 and C9#3) carrying different HRE length (150u, 1200u, 630u, respectively) and 2 healthy control *wild-type (WT)* individuals (CNTRL#1 and CNTRL#2) were previously generated in our lab and were available at the time of the experiments (**Table 7**).

Sample	Phenotype	Sex	Age of onset	Age at collection	Disease duration (months)	*C9ORF72* HRE length
C9#1-1 **C9#1-2**	ALS	F	47	49	12	150u 1200u
C9#3	ALS	M	62	65	58	630u
CNTRL#1	-	M	-	37	-	-
CNTRL#2	-	F	-	45	-	-

Table 7. *iPSC available in the lab.* Features of the patients whose iPSC were available in our laboratory, including 2 *C9ORF72* mutant and 2 healthy control *WT* individuals**.** C9#1-1 and C9#1-2 are referred to two different iPSC clone carrying different expansion length derived from the same patient.

In particular, fibroblasts were reprogrammed using a commercial kit based on a modified non-transmissible form of Sendai virus for the delivery and the transient expression of the four Yamanaka factors Oct3/4, Sox2, Klf-4 and C-Myc (detailed protocol in Materials and Methods section) (**Fig. 1a**). iPSC lines have already been proven to be positive for the expression of the specific stemness transcription factors OCT3/4, SOX2 and NANOG, and of the pluripotency markers ALP (alkaline phosphatase), SSEA-4 (stage-specific embryonic antigen-4), and TRA-1-60 (podocalyxin) by immunofluorescence (IF) (**Fig. 1b**). In order to assess whether the three different *C9ORF72* iPSC lines recapitulated *C9ORF72* hallmarks, we analyzed the presence of pathological RNA foci by Fluorescence *In Situ* Hybridization (FISH), using a fluorescent 5' TYE 563 labelled oligonucleotide $(C_4G_2)_{2.5}$ for detecting the sense HRE-containing transcript (**Fig. 1c**). As a negative control, we used an iPSC line from a healthy control *WT* individual. We analyzed FISH images by quantifying the percentage of cells which were positive for RNA foci and the mean number of RNA foci per RNA foci-positive cells. Our results showed, as expected, the absence of RNA foci in control *WT* iPSC.

The three different *C9ORF72* iPSC showed a variable percentage of RNA foci-positive cells, that ranged from 3% to 20%, with a mean number of 1-3 foci per foci-positive cells. A correlation between HRE length and RNA foci formation was not observed (**Fig. 1d**).

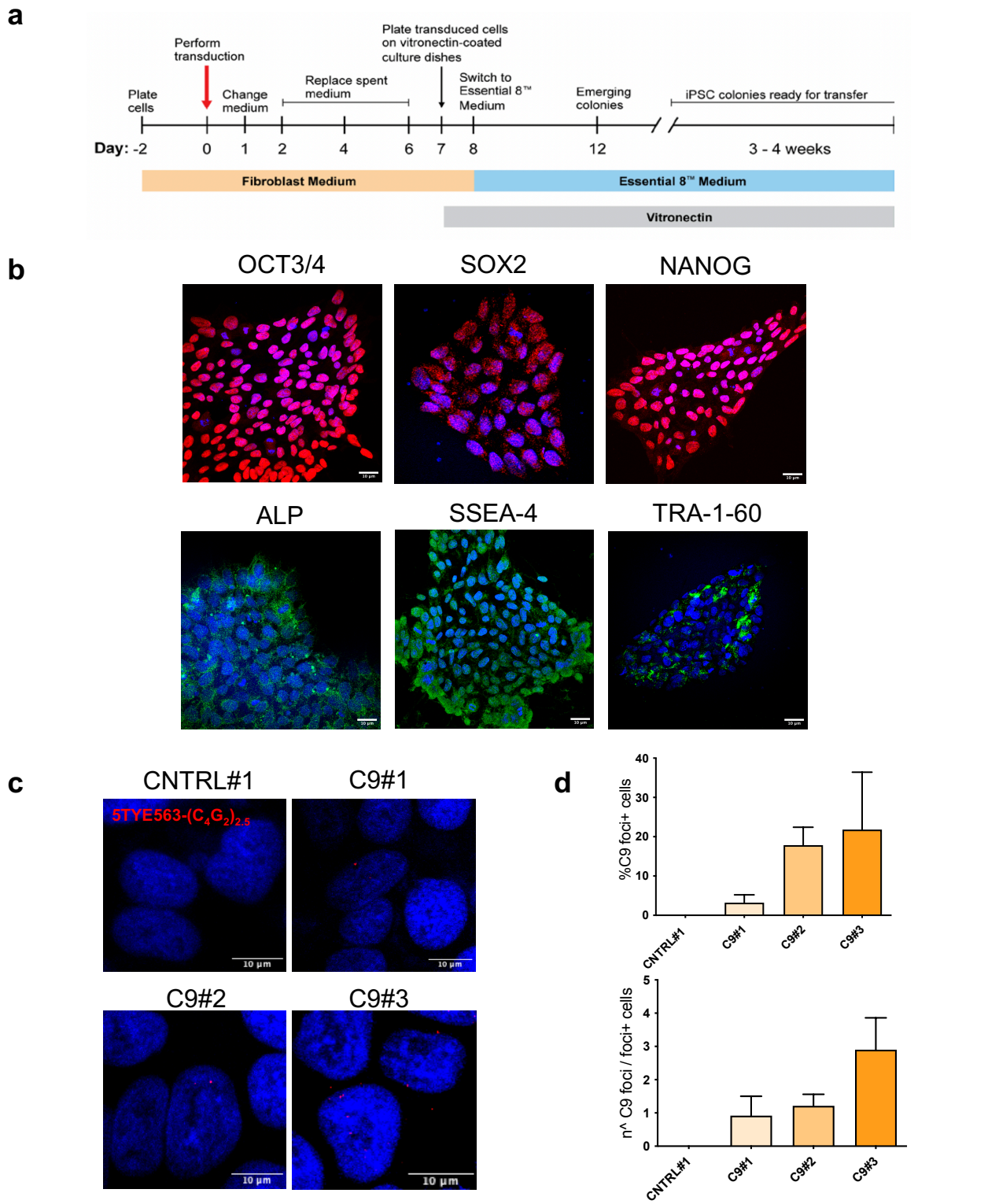

Fig.1 Generation and characterization of *C9ORF72* iPSC lines. a) Timeline of iPSC reprogramming from primary fibroblasts. **b)** Expression of the specific pluripotency markers OCT3/4, SOX2, NANOG (all in red), ALP, SSEA-4, TRA-1-60 (all in green) by IF. Cell nuclei were stained with DAPI (blue). Scale bar, 10 µm. **c)** Analysis of *C9ORF72* RNA foci (red) by FISH on a control *WT* iPSC (CNTRL#1) and the 3 *C9ORF72* iPSC. Cell nuclei were stained with DAPI (blue). Scale bar, 10 µm. **d)** Quantification of pathological *C9ORF72* RNA foci, represented as the percentage of RNA foci-positive cells (above) and the mean number of RNA foci per foci-positive cells (below). Mean±SEM; one-way ANOVA; Kruskall-Wallis test. (n=3, >50 cells per iPSC line were analyzed). ****p<0.0001, *** p<0.001, ** p<0.01, * p<0.05.

1.2. Evaluation of DNA damage and DDR in C9ORF72 iPSC-neural stem cells

We first investigated DNA damage and DDR in Neural Stem Cells (NSC) that, compared to the pluripotent iPSC, are multipotent and already committed towards a neural phenotype and can be further differentiated into neurons and glial cells. We therefore differentiated 3 mutant *C9ORF72* and 2 control *WT* iPSC into NSC (iPSC-NSC) by culturing them in neural induction medium for 7 days and in neural expansion medium for further 5 days (**Fig. 2a**). We next characterized the differentiated iPSC-NSC for the expression of the specific neural stem/progenitor cell marker Nestin by IF. Images showed positivity for the expression of the analyzed marker (**Fig. 2b**) in all iPSC-NSC, indicating a successful NSC differentiation.

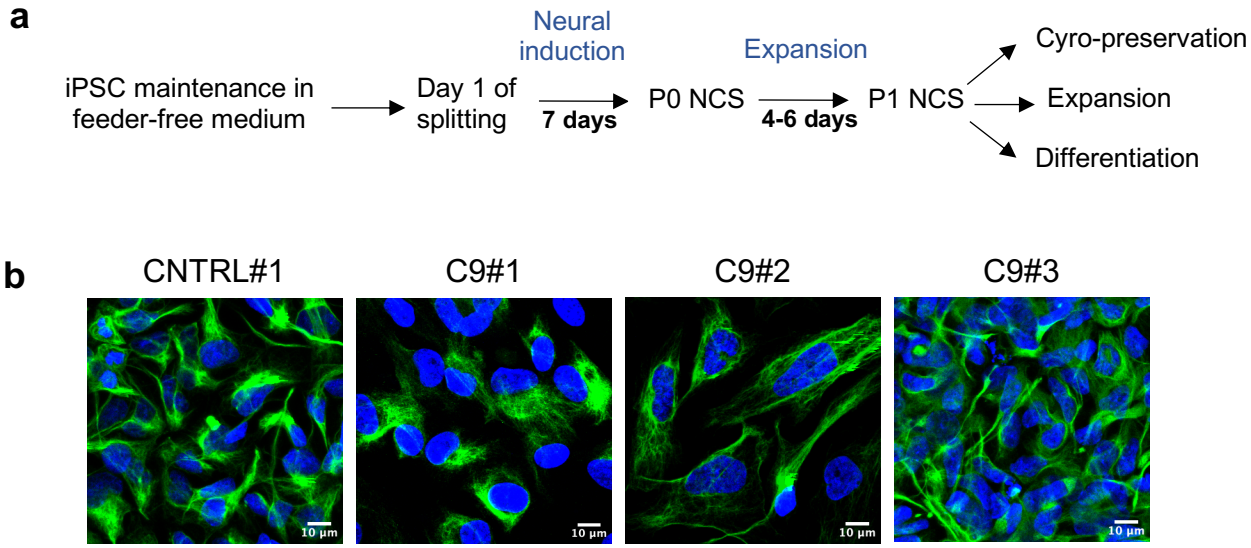

Fig.2 Generation and characterization of control *WT* and *C9ORF72* iPSC-neural stem cells. a) Timeline of iPSC differentiation into NSC (*adapted from Thermo Fisher Scientific protocol*). **b)** Expression of the neuronal marker Nestin (green) by IF for the control *WT* line (a representative image of one control is shown) and 3 *C9ORF72* iPSC-NSC lines. Cell nuclei were stained with DAPI (blue). Scale bar, 10 µm.

We next evaluated the DNA damage and DDR in 3 *C9ORF72* iPSC-NSC compared to the 2 control *WT* iPSC-NSC. To this end, we induced DNA double-strand breaks (DSB) with the radiomimetic agent neocarzinostatin (NCS) for 20 minutes. We then investigated DNA damage levels at basal condition, immediately after the treatment with NCS agent and at different rescue time points (4, 8 and 24 hours) after NCS removal (**Fig. 3a**), by performing IF staining for the phosphorylated form of the H2AX histone (γH2AX), a well-established marker of DSB, and the p53 binding protein 53BP1 (**Fig. 3b**).

We analyzed the images by quantifying the percentage of cells forming for γH2AX and the mean number of γH2AX foci per foci-positive cells.

Our results showed that, at basal level, both *C9ORF72* and control *WT* iPSC-NSC have a high percentage of γH2AX foci-positive cells ranging from 70% to 85%, without significant differences between the two groups. After the treatment with NCS agent, the percentage of γH2AX foci-positive cells significantly increased up to 100% and it then returned to the respective basal level 24 hours after NCS removal in all iPSC-NSC (**Fig. 3c**).

We also demonstrated that, at basal level, *C9ORF72* iPSC-NSC had a similar number of γH2AX foci per foci-positive cells compared to the control *WT* iPSC-NSC, normalizing all values to the untreated control *WT* iPSC-NSC (**Fig. 3d**). After DNA damage induction with NCS agent, the mean number of foci per foci-positive cell increased (2,3X and 3,1X for control and *C9ORF72*, respectively) and it then returned to the respective basal levels 24 hours after NSC removal, with no significant differences among groups (**Fig. 3d**).

We also classified cells into four arbitrary categories according to the number of foci they presented: from 2 to 5 foci, from 6 to 20 foci, from 21 to 30 foci and more than 30 foci. At basal level, the number of foci per foci-positive cells mainly belonged to the two smaller categories (2-5 and 6-20 foci/foci positive cells). After treatment, there was an increased representation of the two cell categories with higher numbers of γH2AX foci (21-30 and >30), but the distribution pattern then returned similar to the basal condition with no significant changes between control *WT* and *C9ORF72* iPSC-NSC (**Fig. 3e**).

Altogether, these results suggest that *C9ORF72* mutation has no effect on DNA damage and DDR in iPSC-NSC in our experimental conditions.

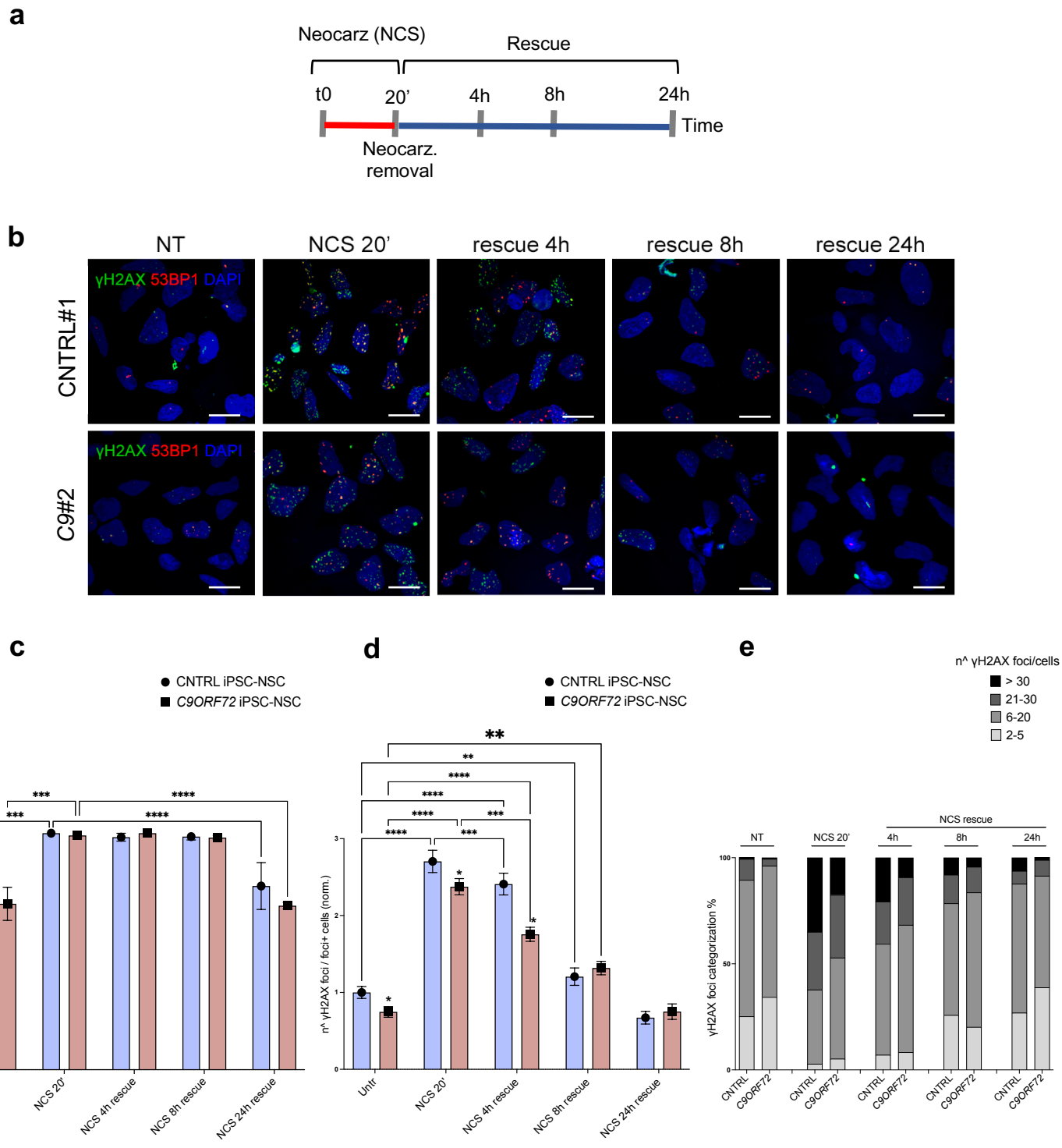

Fig.3 DNA damage and DDR in *C9ORF72* iPSC-neural stem cells. a) Timeline of the DNA damage experiment with neocarzinostatin (NCS). **b)** Evaluation of γH2AX (green) and 53BP1 (red) foci by IF. Cell nuclei were stained with DAPI (blue). Representative images of 1 control *WT* and 1 *C9ORF72* iPSC-NSC are shown for each condition. Scale bar, 10 μm. iPSC derived from 2 control *WT* and from 3 mutant *C9ORF72* ALS patients were used for comparison. Quantification of γH2AX foci after neocarzinostatin (NCS) treatment (20') and at different rescue time points (4-8-24h), represented as **c)** the percentage of γH2AX foci-positive cells, **d)** the mean number of γH2AX foci per foci-positive cells, normalized to the untreated control *WT* iPSC-NSC and **e)** the γH2AX foci number distribution in four arbitrary categories. Mean±SEM; two-way ANOVA and multiple comparison test on replicate measures for each cell line (n=3, 150 cells were analyzed for each line/condition). ****p<0.0001, *** p<0.001, ** p<0.01, * p<0.05.

1.3. Assessment of DNA damage and DDR in C9ORF72 iPSC-motoneurons

To investigate DNA damage and DDR in post-mitotic neuronal cells, we differentiated 2 mutant *C9ORF72* and 2 control *WT* iPSC into motoneurons (iPSC-MN), using a protocol that included the generation of embryoid bodies for 21 days and their subsequent dissociation and differentiation with specific factors (**Fig. 4a**).

At day 34, we characterized the newly differentiated iPSC-MN for the expression of the specific neuronal markers SMI-312 (neurofilaments, pan-axonal), MAP2 and βIII-tubulin (neuronal microtubules) and for the specific MN marker HB9 (homeobox transcription factor) by IF. Images showed positivity for the expression of all the analyzed markers, indicating a successful MN differentiation (**Fig. 4b**).

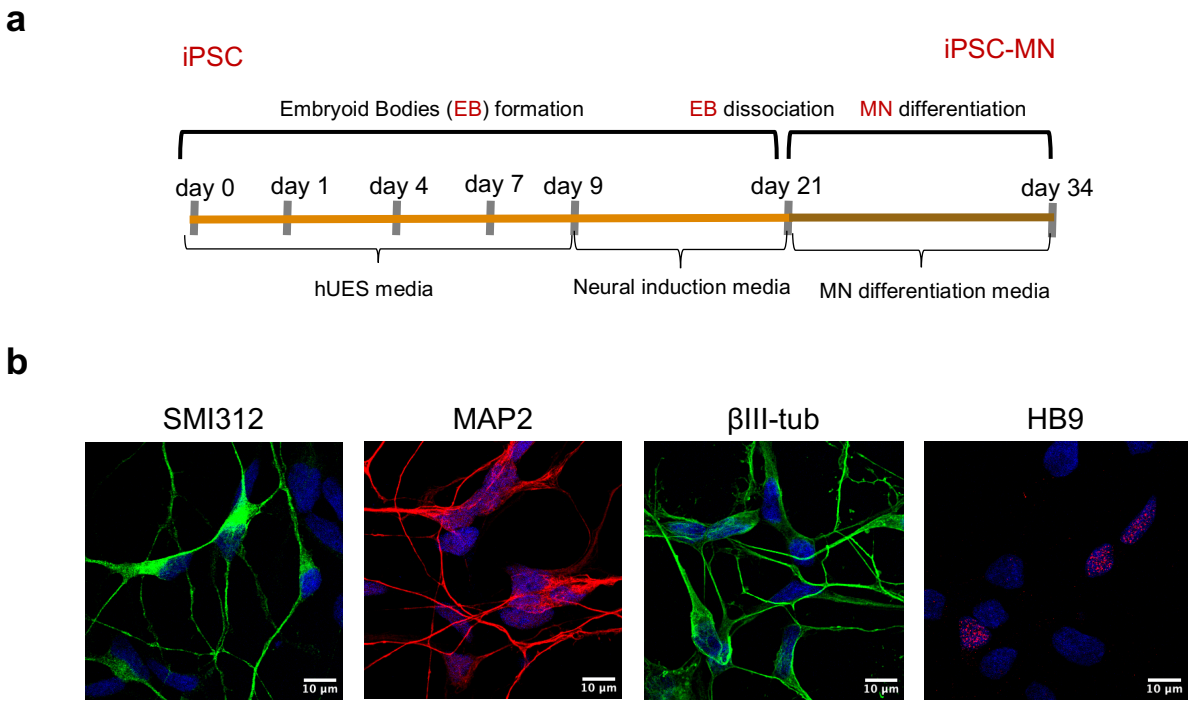

Fig.4 Generation and characterization of control *WT* and *C9ORF72* iPSC-MN. a) Timeline of iPSC-MN differentiation. **b)** Representative images showing the expression of the neuronal markers SMI-312 (green), MAP2 (red), βIII-tubulin (green), and of the specific MN marker HB9 (red) by IF; cell nuclei were stained with DAPI (blue). Scale bar, 10 µm. iPSC-MN derived from 2 control *WT* and from 2 mutant *C9ORF72* ALS patients were used for comparison.

To assess the extent of DNA damage and DDR in *C9ORF72* iPSC-MN, we used the same experimental paradigm of iPSC-NSC, inducing DSB with NCS agent for 20 minutes (**Fig. 5a**). The analysis of DNA damage in the newly differentiated iPSC-MN at physiological level revealed that *C9ORF72* iPSC-MN showed a significant higher percentage of γH2AX-positive cells (**Fig. 5b**) compared to control *WT* iPSC-MN. *C9ORF72* iPSC-MN present also a higher mean fluorescence intensity of γH2AX inside the nucleus (**Fig. 5c**) with a similar mean number of γH2AX foci (**Fig. 5d**) compared to the normalized control *WT* iPSC-MN, suggesting that *C9ORF72* iPSC-MN could form larger γH2AX foci. These results suggest that *C9ORF72* mutation could make iPSC-MN more vulnerable to DNA damage events in physiological conditions.

To study DDR, since in iPSC-NSC we observed that DNA damage levels were rescued between 8 and 24 hours, we decided to set the rescue time point at 6 hours (**Fig. 5a**), in order to better evidence possible differences in DDR during the recovery time.

Our results showed that after the treatment with NCS agent, the mean number of γH2AX foci, normalized to the untreated control *WT* iPSC-MN, increased both in *C9ORF72* (2,2X) and in control *WT* iPSC-MN (3X) compared to their basal condition (**Fig. 5e-f**). Upon 6 hours-rescue time from NCS treatment, both iPSC-MN groups significantly rescued the induced DNA damage without significant differences between the two groups (1.8 vs 1.9, respectively), although they did not return to the respective basal levels (**Fig. 5e-f**).

Altogether, these results indicate that in our experimental conditions the presence of *C9ORF72* mutation does not affect DDR even in iPSC-MN.

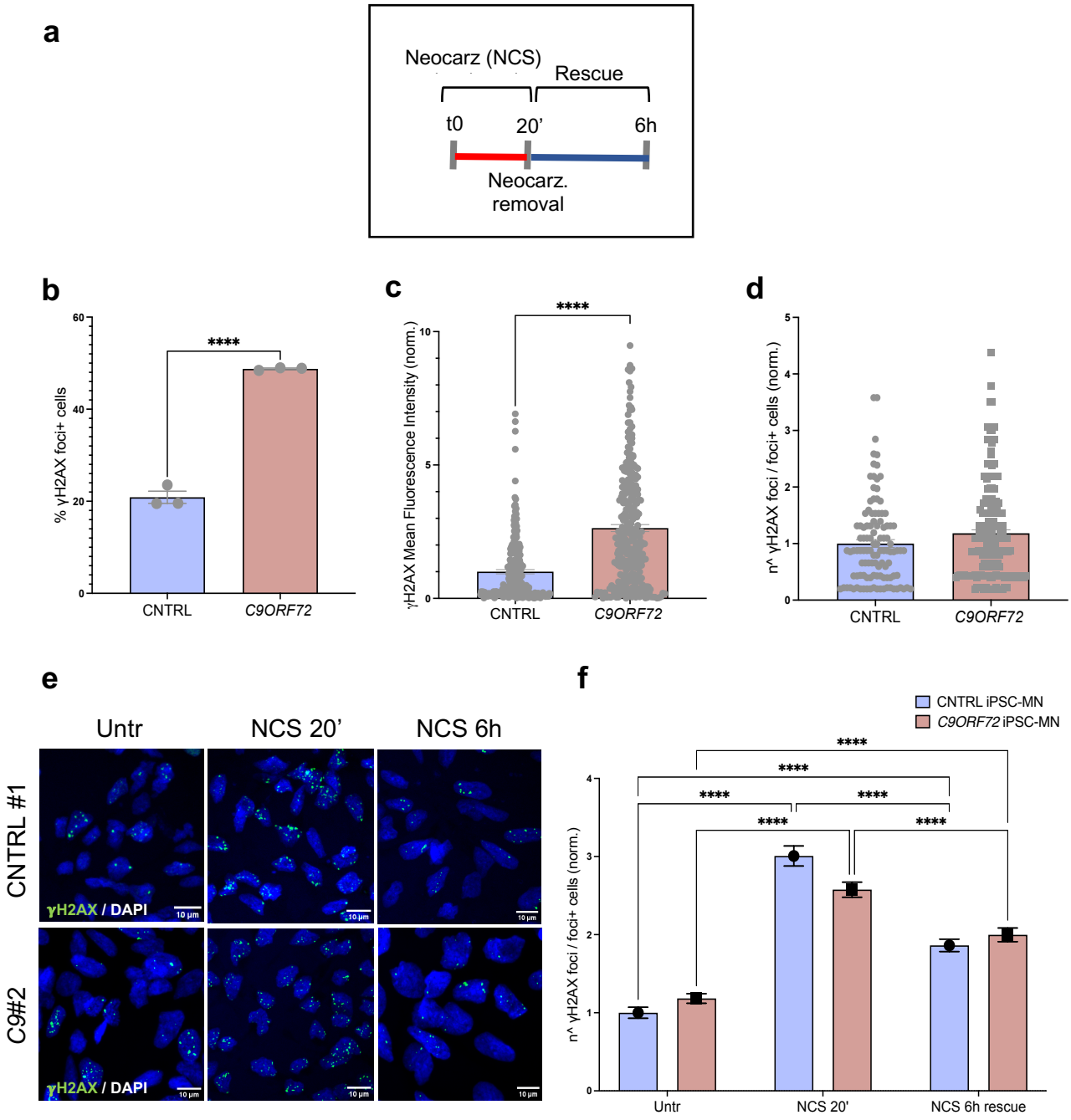

Fig.5 DNA damage and DDR in *C9ORF72* iPSC-MN. a) Timeline of the DNA damage experiments with neocarzinostatin (NCS). iPSC-MN from 2 control *WT* individuals and from 2 mutant *C9ORF72* ALS patients were used for comparison. Quantification of γH2AX foci at physiological level, represented as **b)** the percentage of γH2AX foci-positive cells, **c)** the mean fluorescence intensity of γH2AX in the cell nucleus and **d)** the mean number of γH2AX foci per foci-positive cells, normalized to the control *WT* iPSC-MN. Mean±SEM; Unpaired t-test (n=3, 150 cells were analyzed for each iPSC-MN line). **e)** Evaluation of γH2AX (green) foci by IF. Cell nuclei were stained with DAPI (blue). Representative images of 1 control *WT* and 1 *C9ORF72* iPSC-MN are shown for each condition. Scale bar, 10 µm. **f)** Quantification of γH2AX foci after neocarzinostatin (NCS) treatment (20') and at 6h rescue, represented as the mean number of γH2AX foci per foci-positive cells, normalized to the untreated control *WT* iPSC-MN. Mean±SEM; two-way ANOVA and multiple comparison test on replicate measures for each cell line (n=3, 150 cells were analyzed for each line/condition). ****p<0.0001, *** p<0.001, ** p<0.01, * p<0.05.

1.4. Study of DNA damage and DDR in aged C9ORF72 iPSC-motoneurons

Given that ALS is an adult-onset disease, we then wanted to better mimic the aging process by differentiating motoneurons for a longer time until day 56, following the same experimental paradigm of DNA damage induction shown in (**Fig. 5a**).

We found that in physiological condition *C9ORF72* iPSC-MN present a trend, although not significant, of a higher percentage of γH2AX-positive cells (**Fig. 6a**).

Moreover, the mean number of γH2AX foci per cells (**Figure 6b**) and mean fluorescence intensity of γH2AX inside the nucleus (**Fig. 6c**) were significantly higher in aged *C9ORF72* compared to the normalized control *WT* iPSC-MN. These results suggest that the higher susceptibility of mutant *C9ORF72* iPSC-MN to DNA damage is maintained during aging in culture.

When we treated iPSC-MN with NCS, the DNA damage was induced as expected in both experimental groups (**Fig. 6d**), but with a significant fold increase in the number of γH2AX foci per cells (**Fig. 6e**) and mean fluorescence intensity of γH2AX (**Fig. 6f**) in *C9ORF72* iPSC-MN compared to control ones, normalizing all values to the untreated control *WT* iPSC-MN. At 6h after NCS treatment, both control *WT* and *C9ORF72* iPSC-MN rescued the induced DNA damage, even if *C9ORF72* iPSC-MN still presented a significant higher level of DNA damage compared to the control (**Fig. 6e-f**), suggesting that *C9ORF72* mutation could impair the ability of more “aged” iPSC-MN to activate DNA damage response pathways.

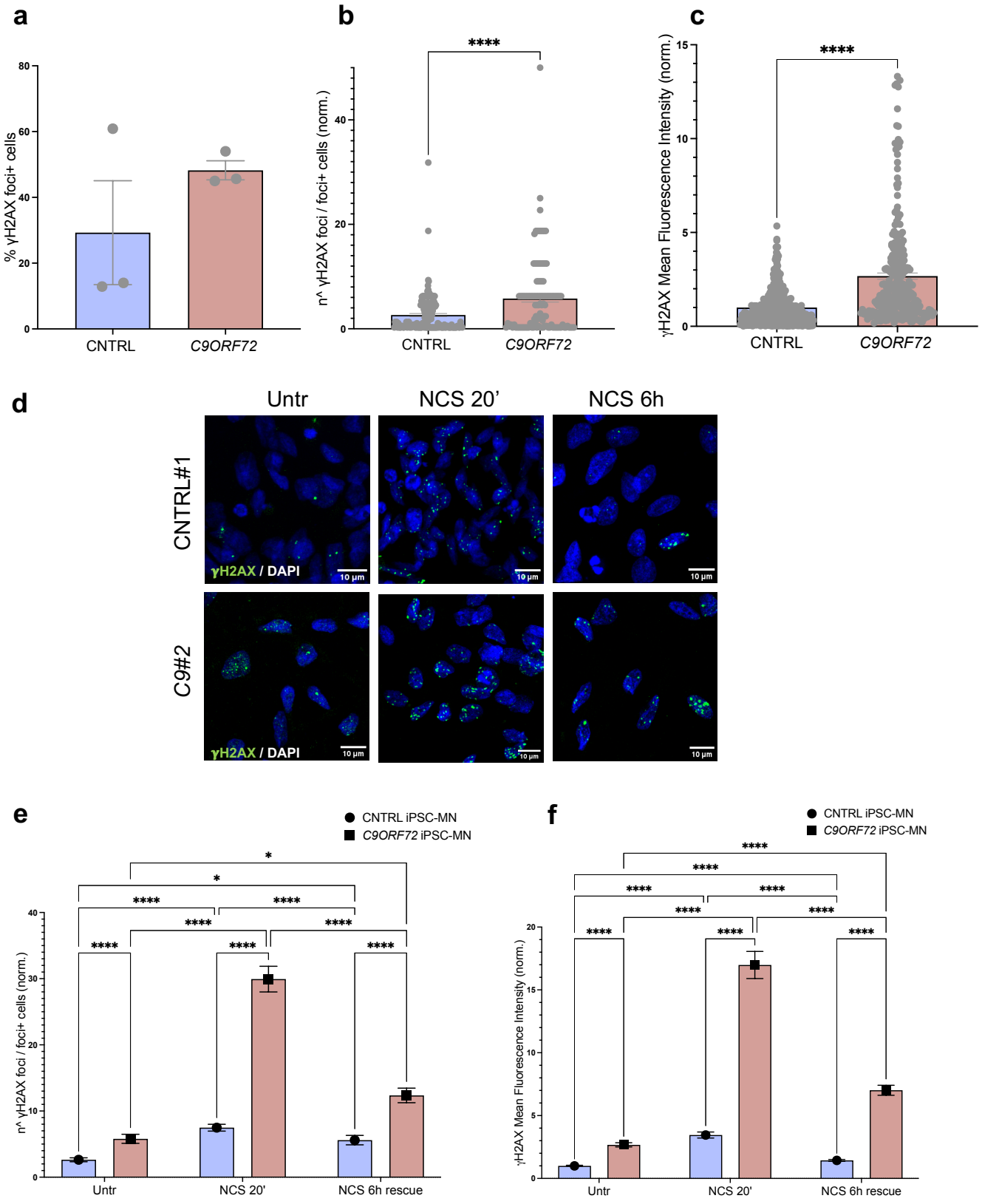

Fig.6 DNA damage and DDR in *C9ORF72* aged iPSC-MN. iPSC-MN from 2 control *WT* individuals and from 2 mutant *C9ORF72* ALS patients were used for comparison. Quantification of γH2AX foci at physiological level, represented as **a)** the percentage of γH2AX foci-positive cells, **b)** the mean number of γH2AX foci per foci-positive cells and **c)** the mean fluorescence intensity of γH2AX in the cell nucleus, normalized to the control *WT* iPSC-MN. Mean±SEM; unpaired t-test (n=3, 150 cells were analyzed for each line/condition). **d)** Evaluation of γH2AX (green) foci by IF. Cell nuclei were stained with DAPI (blue). Representative images of 1 control *WT* and 1 *C9ORF72* iPSC-MN are shown for each condition. Scale bar, 10 µm. Quantification of γH2AX foci after neocarzinostatin (NCS) treatment (20') and at 6h rescue, represented as **e)** the mean number of γH2AX foci per foci-positive cells and **f)** the mean fluorescence intensity of γH2AX in the cell nucleus, normalized to the untreated control *WT* iPSC-MN. Mean±SEM; two-way ANOVA and multiple comparison test on replicate measures for each cell line (n=3, 150 cells were analyzed for each line/condition). ****p<0.0001, *** p<0.001, ** p<0.01, * p<0.05.

2. Impact of actin cytoskeleton modulation on DNA damage in *C9ORF72* iPSC

2.1. DNA damage and DDR following actin modulation in HEK293T cells: a pilot study

During my 3-months internship at Dr. Claudia Fallini's lab (University of Rhode Island, USA), I investigated the existence of a possible crosstalk between cytoskeleton forces and DNA damage, by studying how modulation of the actin cytoskeleton impacts on the incidence of DNA damage in *C9ORF72* patient-derived cells. To modulate actin cytoskeleton, we used two drugs: Intramimic (IMM) to induce polymerization of unbranched actin filaments, and Latrunculin B (LATR), which induces actin filament depolymerization.

We first conducted a pilot study to assess the action of these opposite actin-modifier drugs treating HEK293T cells with IMM 0,1 μM or LATR 0,5 μM for 6 hours (**Fig. 7a**). We found that IMM drug, but not LATR, significantly increased the mean fluorescence intensity of γH2AX (**Fig. 7b**), suggesting that induction of actin cytoskeleton polymerization is able to promote DNA damage in HEK293T cells.

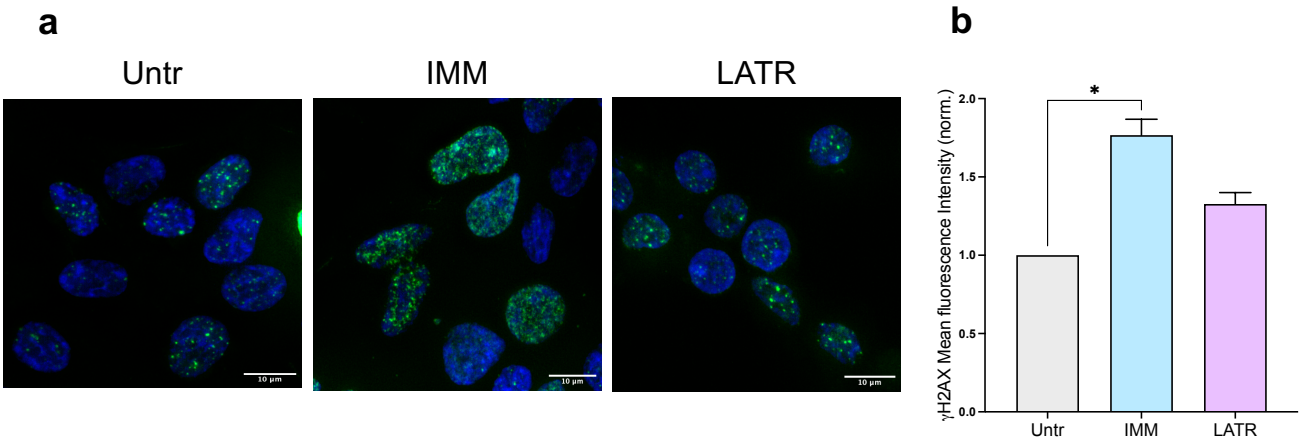

Fig.7 DNA damage in HEK293T cells upon actin modulation. a) Representative image of HEK293T cells in basal condition (Untr), after treatment with 0,1 μM Intramimic (IMM) or 0,5 μM Latrunculin (LATR) drugs, showing γH2AX (green) foci by IF. Cell nuclei were stained with DAPI (blue). Scale bar, 10 μm. **b)** Quantification of γH2AX foci upon actin-modifier drugs in HEK293T cells, represented as the mean fluorescence intensity of γH2AX, normalized to the untreated cells. Mean+SEM; one-way ANOVA, Kruskall-Wallis test. (n=3, 150 cells were analyzed for each condition). ****p value <0.0001, *** p<0.001, ** p<0.01, * p<0.05.

To analyze whether actin cytoskeleton modulation impacts on the capacity of HEK293T cell to respond to a DNA damage insult, we first induced DNA damage using NCS for 20 minutes, at the end of which we replaced the media with fresh media containing IMM or LATR drugs for 6 hours (**Fig. 8a**).

As expected, DNA damage levels significantly increased after 20 minutes of NCS treatment compared to the normalized untreated level. After 6 hours rescue from DNA damage

induction, we observed that in HEK293T cells treated with IMM the γH2AX mean fluorescence significantly increased compared to cells at 6h rescue without any drugs, while in cells treated with LATR DNA damage levels were comparable (**Fig. 8b**). Indeed, our results suggest that actin polymerization impairs the ability of HEK293T cells to DDR.

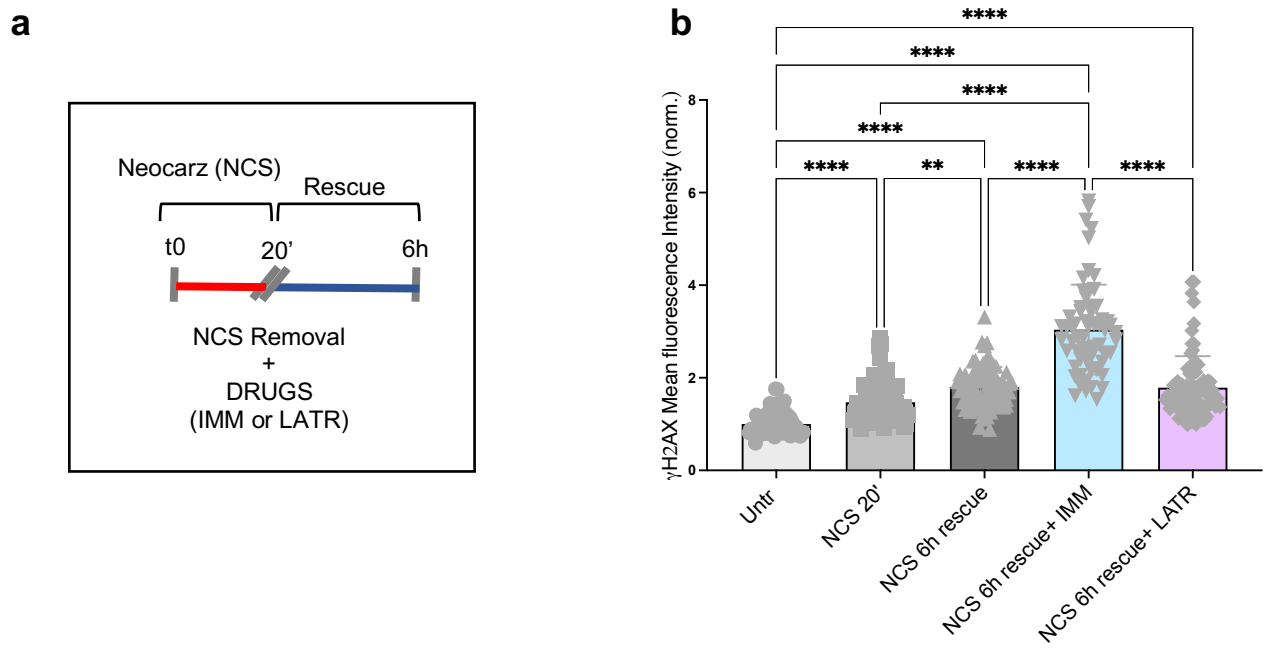

Fig.8 DDR in HEK293T cells upon actin modulation. a) Timeline of the DNA damage experiments. **b)** Quantification of γH2AX foci represented upon neocarzinostatin (NCS) treatment (20') and at 6h rescue in presence of actin-modifier drugs (IMM 0,1 μM or LATR 0,5 μM). All values were normalized to the untreated cells. Mean+SEM; one-way ANOVA, Kruskall-Wallis test. (n=3, >150 cells were analyzed for each condition). ****p value <0.0001, *** p<0.001, ** p<0.01, * p<0.05.

2.2. *DNA damage and DDR following actin modulation in C9ORF72 i^3-cortical neurons*

We validated the results obtained in HEK293T cells in i^3-cortical neurons (i^3-CN) differentiated from 1 isogenic *WT* and 1 *C9ORF72* i^3-iPSC lines, using the novel method described by Dr. Ward with minor modifications, which is schematized in (**Fig. 9a**) and explained in detail in the Materials and Methods section. This method relies on the integration of the gene expression cassette containing the glutamatergic cortical factor neurogenin2 (NGN2) in a safe harbor locus into the genome and produces >90% pure cortical populations (144). We assessed the differentiation efficiency of i^3-CN visualizing their positivity to the most commonly used cortical neurons markers (**Fig. 9b**).

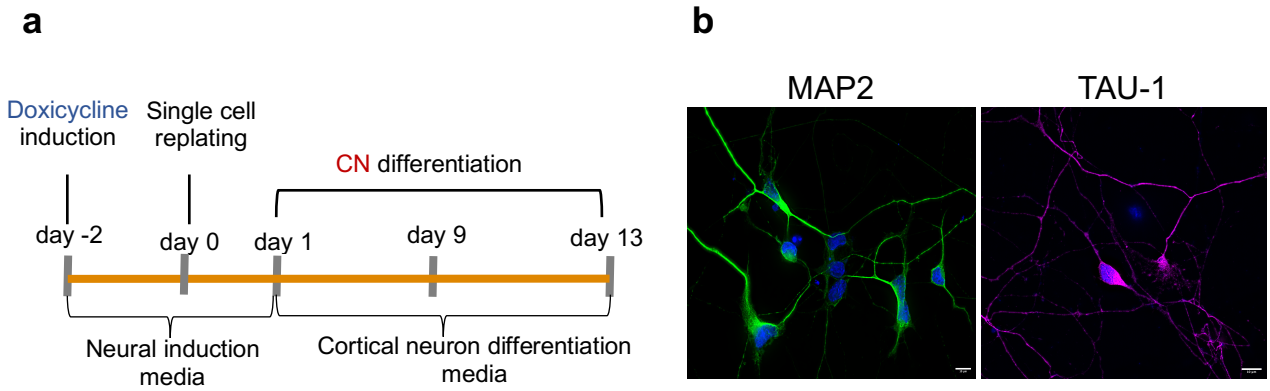

Fig.9 Differentiation and characterization of i^3-cortical neurons (i^3-CN) derived from 1 isogenic *WT* and 1 *C9ORF72* i^3-iPSC line. a) Timeline of i^3-CN differentiation (adapted from Ward et al., 2020) **b)** Representative image showing the expression of the neuron MAP2 marker (green) and the specific glutamatergic cortical neuron TAU-1 marker (purple), by IF; cell nuclei were stained with DAPI (blue). Scale bar, 10μm.

We evaluated the extent of DNA damage and DDR comparing the mutant *C9ORF72* i^3-CN with the isogenic *WT* by measuring the mean fluorescence intensity of γH2AX (**Fig. 10a**), normalized to the untreated isogenic iPSC-MN values. We showed that, in contrast to iPSC-MN, *C9ORF72* mutation did not increase physiological DNA damage in i^3-CN (**Fig. 10b**). Because of this similar behavior, we believed that i^3-CN could represent a suitable cell model to study the effects caused by actin modulation on DNA damage and DDR in mutant and control human neurons.

We treated i^3-CN with the agent NCS to induce DNA damage and with IMM or LATR to modulate actin cytoskeleton dynamics, using the same experimental paradigm previously shown for HEK293T cells (**Fig. 8a**). Our results showed that after 6 hours of DNA damage rescue from NCS treatment, *C9ORF72*-i^3-CN presented a higher level of γH2AX marker

compared to the isogenic *WT* i^3-CN (**Fig. 10a-b**), suggesting that *C9ORF72* i^3-CN are more susceptible to DNA damage accumulation than control *WT* i^3-CN.

After 6 hours rescue in presence of each actin-modifier drug (IMM or LATR), we observed a further significant increase of DNA damage levels in the isogenic *WT* i^3-CN with both drugs, indicating that changes in F-actin polymerization may influence DDR. Interestingly, *C9ORF72*-i^3-CN didn't respond to the two actin-modifier drugs (**Fig. 10a-b**), suggesting that cytoskeleton dynamics is already impaired in mutant *C9ORF72*-i^3-CN.

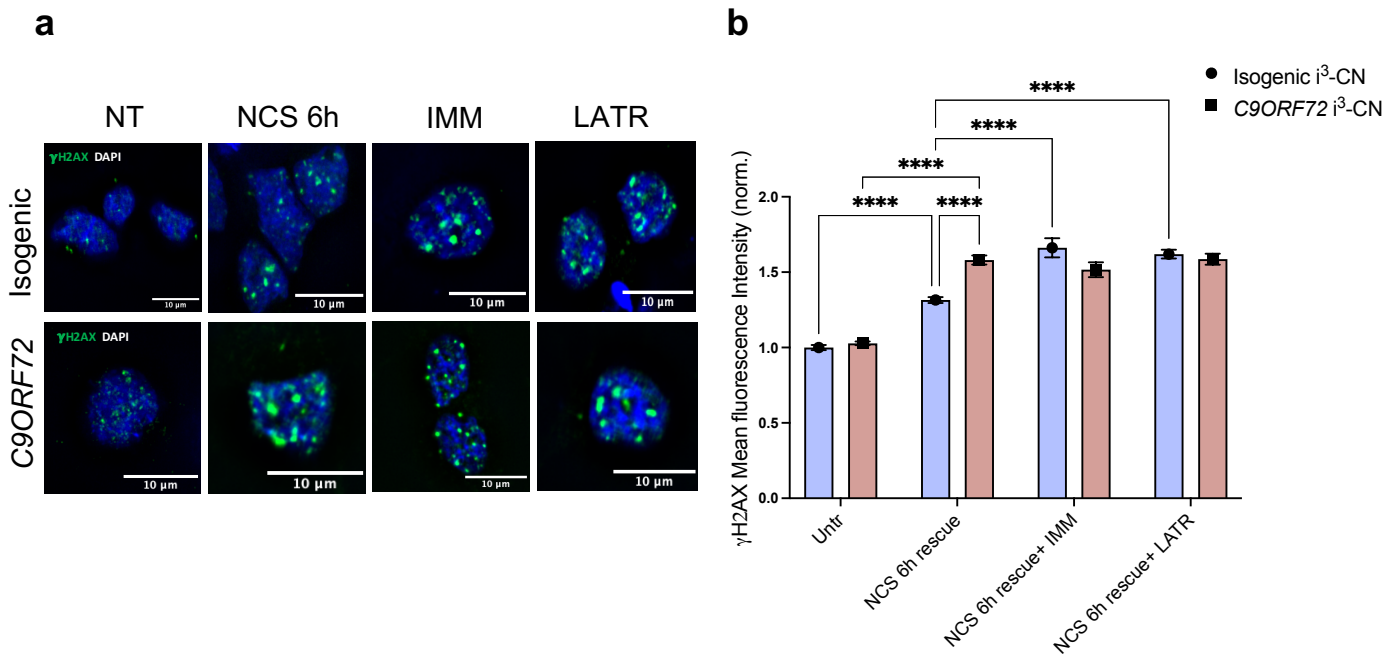

Fig.10 Impact of actin modulation on DDR in *C9ORF72* i^3-CN. a) Evaluation of γH2AX (green) foci by IF upon neocarzinostatin (NCS) treatment at 6h rescue (NCS 6h) in presence of actin-modifier drugs (IMM or LATR). Cell nuclei were stained with DAPI (blue). Scale bar,10 µm. i^3-CN from 1 isogenic *WT* individual and from 1 mutant *C9ORF72* ALS patient were used for comparison. **b)** Quantification of γH2AX foci represented as the mean fluorescence intensity of γH2AX, upon neocarzinostatin treatment at 6h rescue (NCS 6h) in presence of actin-modifier drugs (IMM 0,1 µM or LATR 0,5 µM). All values were normalized to the untreated isogenic *WT* i^3-CN. Mean±SEM; two-way ANOVA and multiple comparison test on replicate measures for each cell line (n=3, >80 cells were analyzed for each line/condition). ****p<0.0001, *** p<0.001, ** p<0.01, * p<0.05.

2.3. Chromatin remodeling following actin modulation in C9ORF72 i^3-iPSC-CN

We then investigated if modifications to the F-actin cytoskeleton may induce also changes in chromatin organization. We analyzed the mean fluorescence intensity of H3K9me3 (Histone 3 lysine 9 trimethylation), an epigenetic marker associated to changes in chromatin remodeling at the periphery of the nucleus.

We observed a higher level of H3K9me3 in *C9ORF72*-i^3-CN compared to the isogenic *WT* cells (**Fig. 11a-b**). We then assessed if modulation of F-actin polymerization also affects the distribution of peripheral chromatin in i^3-CN. We treated i^3-CN with IMM and LATR for 6 hours and we found that the two actin-modifier drugs increased the level of H3K9me3 in both the isogenic *WT* and the *C9ORF72*-i^3-CN (**Fig. 11a-b**).

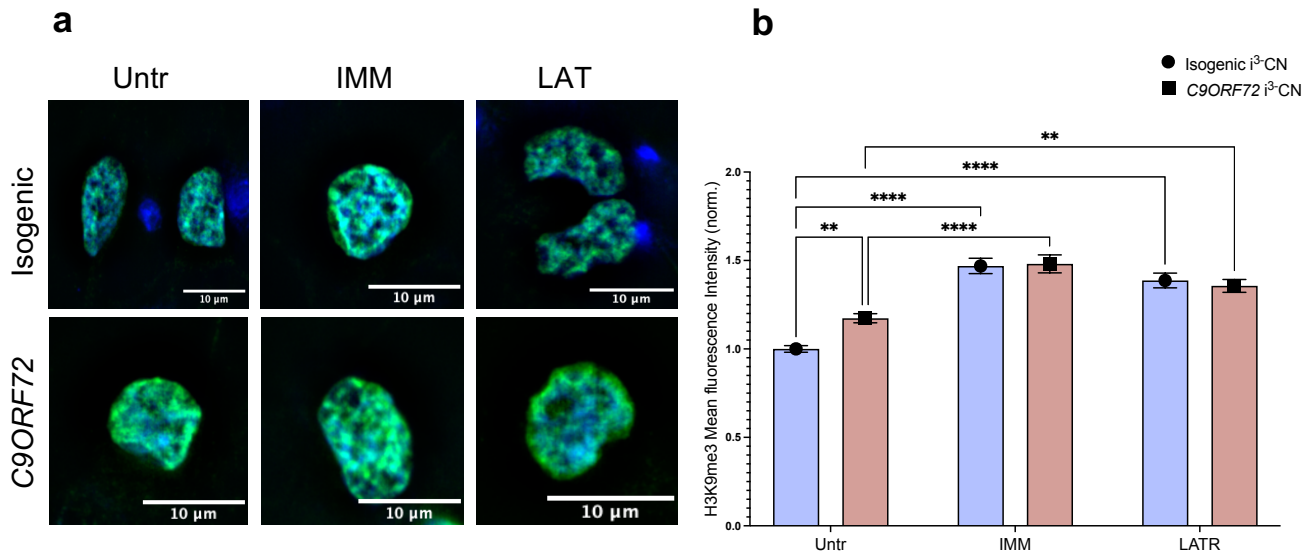

Fig.11 Impact of F-actin modulation on chromatin remodeling in *C9ORF72* i^3-CN. a) Evaluation of H3K9me3 (green) staining by IF. Cell nuclei were stained with DAPI (blue). Scale bar,10 µm. i^3-CN from 1 isogenic *WT* individual and from 1 mutant *C9ORF72* ALS patient were used for comparison. **b)** Quantification of H3K9me3 represented as the mean fluorescence intensity of H3K9me3, upon actin-modifier drugs (IMM 0,1 µM or LATR 0,5 µM) treatment for 6 hours. All values were normalized to the untreated isogenic *WT* i^3-CN. Mean±SEM; two-way ANOVA and multiple comparison test on replicate measures for each cell line (n=3, >80 cells were analyzed for each line/condition). ****p<0.0001, *** p<0.001, ** p<0.01, * p<0.05.

3. New RNA-based therapeutic approach to decrease *C9ORF72* pathology

In this part of my thesis, I tested a new RNA-based therapeutic approach which consists in a modified spliceosomal U1 small nuclear RNA (U1 snRNA) designed by our collaborator Dr. Franco Pagani (ICGEB, Trieste) to specifically identify and bind the *C9ORF72* repeat sequence in the pre-mRNA, by means of its engineered 5' tail. In particular, two U1 snRNA have been generated, the U1C and U1G, which bind the pathological pre-mRNA four nucleotides before the HRE with two different binding efficiency.

These U1 snRNA were hypothesized to block RNA polymerase II activity, thus preventing transcription and formation of pathological RNA foci and, consequently, their translation into DPR (**Fig. 12a-b**).

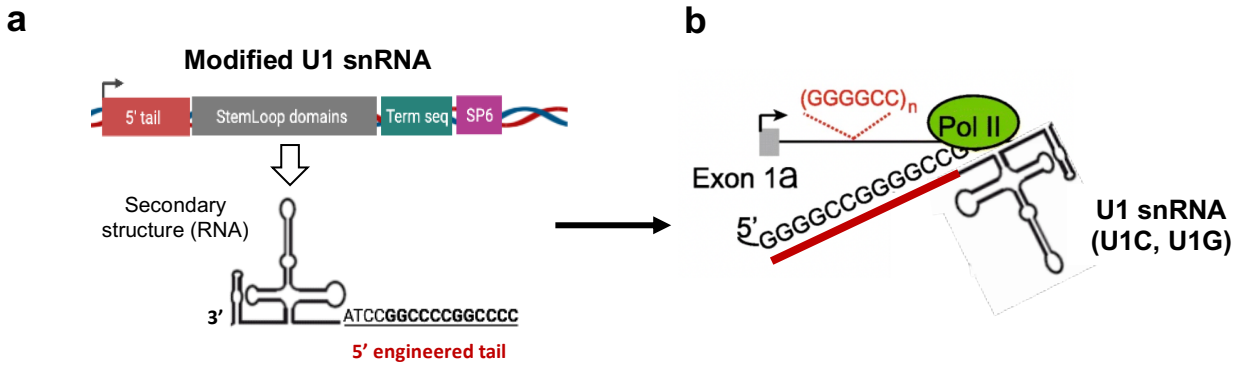

Fig.12 U1 snRNA design and mechanism of action. a) Schematic sequence of modified plasmid U1 snRNA and RNA secondary structure, including a 5' engineered tail. **b)** Possible mechanism of action of two the U1 snRNA, U1C and U1G, that directly bind the pathological HRE-sequence with different efficiencies, acting similarly to an ASO.

3.1. Preliminary assessment of U1-snRNA efficacy on C9ORF72 pathology in HEK293T

We conducted a pilot study in HEK293T cells to preliminary test whether the two modified U1 snRNA U1C and U1G are able to reduce *C9ORF72*-associated formation of RNA foci.

The U1C and U1G constructs and the U1 mock designed on an unrelated sequence were transfected into HEK293T cells overexpressing the *C9ORF72* HRE $(GGGGCC)_{66}$. The formation of RNA foci was visualized by fluorescence in situ hybridization (FISH) using a specific fluorescent probe against the sense hexanucleotide repeat sequence (5TYE563-$(C_4G_2)_{2.5}$) (**Fig. 13a**). We quantified the percentage of HEK293T cells containing RNA foci and we found that both U1 snRNA constructs significantly decreased the number of cells with RNA foci compared to U1 mock-transfected cells (**Fig. 13b**).

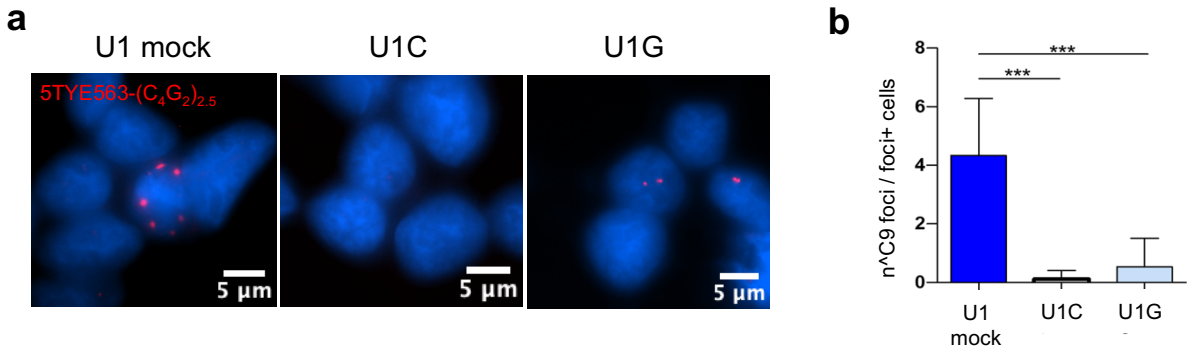

Fig.13 U1 snRNA efficacy on *C9ORF72* RNA foci formation in HEK293T cells. a) Analysis of pathological *C9ORF72* RNA foci (red) by FISH, upon transfection with the control U1 mock, U1C or U1G plasmids. Cell nuclei were stained with DAPI (blue). Scale bar, 5 µm. **b)** Quantification of pathological RNA foci, represented as the mean number of RNA foci per foci-positive cells. Mean±SEM; one-way ANOVA, Kruskall-Wallis test (n=3, >100 cells were analyzed for each condition). ****p<0.0001, *** p<0.001, ** p<0.01, * p<0.05.

To assess whether the observed decrease in *C9ORF72* RNA foci was associated also to a decreased synthesis of dipeptide proteins (DPR), we used a previously reported cell-based assay (145). In particular, we transfected HEK293T cells with a plasmid containing $(G_4C_2)_{58}$ repeats upstream GFP devoid of the AUG sequence to detect RAN translation, and with the plasmid construct AUG-RFP to detect canonical translation (**Fig. 14a**). Upon cotransfection with the U1 snRNA plasmids, we performed quantitative analysis by measuring the ratio between GFP and RFP mean fluorescence intensity (**Fig. 14b**), and we found that in presence of both U1C and U1G snRNA a significant reduction of GFP/RFP ratio was observed compared to the U1 mock transfected cells, suggesting that U1 snRNA have a downstream effect also on RAN translation (**Fig. 14b-c**).

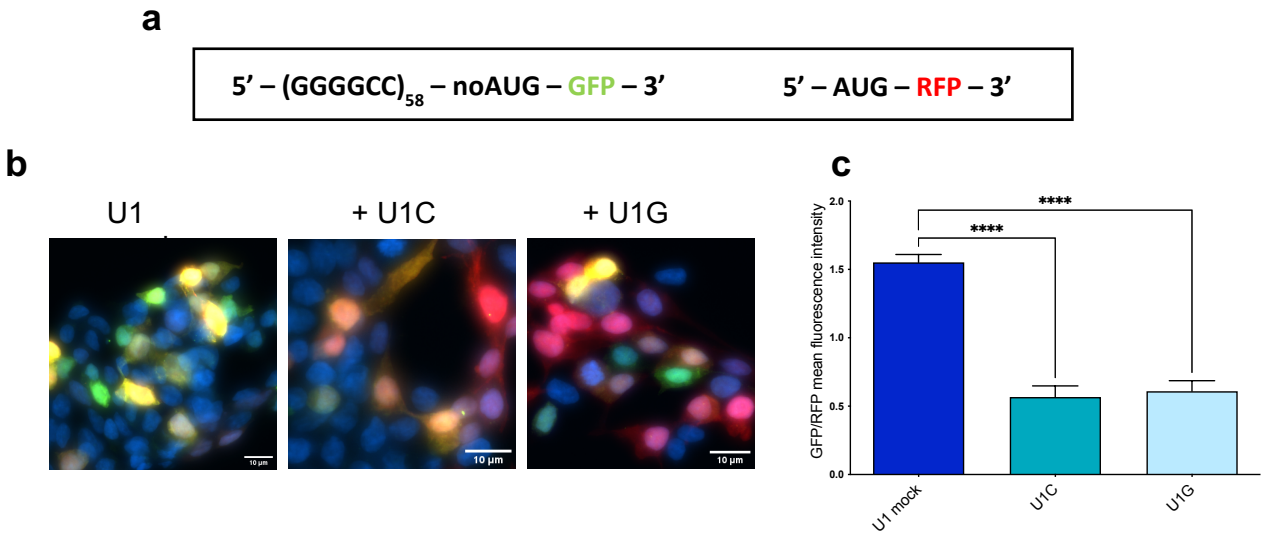

Fig.14 U1 snRNA efficacy on dipeptide protein (DPR) formation in HEK293T cells. a) Schematic representation of the constructs utilized in the cell-based assay for RAN translation. The first construct contains $(G_4C_2)_{58}$ repeats upstream GFP devoid of the AUG sequence in the dipeptide frame, to detect RAN translation. The second construct AUG-RFP is used as positive control of canonical translation. **b)** Representative image of cells undergoing RAN translation (green) and/or canonical translation (red) upon U1 constructs transfection for 48 hours. Cell nuclei were stained with DAPI (blue). Scale bar,10 µm. **c)** Quantification of RAN translation events, represented as the ratio between GFP and RFP mean fluorescence intensity, in U1 mock-transfected cells or upon U1C or U1G transfection. Mean±SEM; one-way ANOVA, Kruskall-Wallis test (n=3, >100 cells were analyzed for each condition). ****p<0.0001, *** p<0.001, ** p<0.01, * p<0.05.

3.2. *Validation of U1 snRNA efficacy in C9ORF72 iPSC-motoneurons*

To validate our results in patient-derived cells, we transfected the previously obtained *C9ORF72* iPSC-NSC (*See Results 1.2.)* with GFP-labelled U1C or U1G snRNA. However, when we performed a co-FISH analysis to quantify GFP-transfected cells forming pathological RNA foci, we failed to detect green fluorescence because the formamide used in the FISH protocol bleached the GFP signal (*data not shown*). Therefore, as we obtained ~70% transfection efficiency with a high cell mortality, we revised our experimental plan and decided to deliver GFP-tagged U1 snRNA-containing lentiviral vectors directly into *C9ORF72* patient-derived iPSC-MN. Third generation lentiviral vectors were generated cloning the U1 mock or U1G-GFP expression cassette into pRRL human immunodeficiency virus-derived backbone. We infected *C9ORF72* iPSC-MN carrying 1200 HRE units at day 47 of differentiation with U1 mock or U1G-GFP lentiviral vectors. After 5 days infection we obtained about 95% of infection efficiency for both constructs (**Fig. 15a**). Subsequent FISH analysis revealed a significant decrease in the number of *C9ORF72* RNA foci per cells (2,7 vs 1,5) (**Fig. 15b-c**) and a decrease in the percentage of cells containing *C9ORF72* RNA foci (46,9% vs 9,5%) (**Fig. 15d**), suggesting that U1G snRNA decreased the content of pathological RNA foci in *C9ORF72* mutant iPSC-MN.

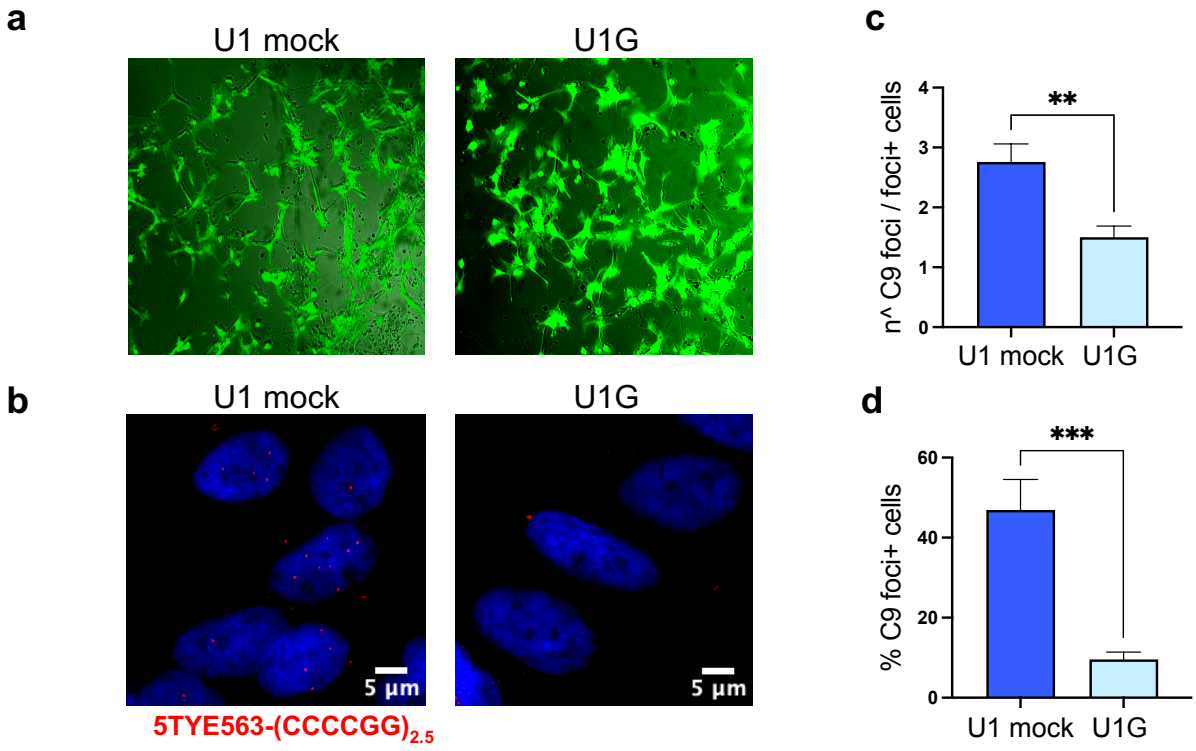

Fig.15 U1 snRNA efficacy on *C9ORF72* RNA foci formation in *C9ORF72* iPSC-MN. a) *C9ORF72* iPSC-MN at day 47 of differentiation were infected with lentivirus-containing GFP-tagged U1 mock or U1G snRNA. The infection efficiency was visualized five days later (green). **b)** Analysis of *C9ORF72* RNA foci (red) by FISH, upon infection with U1 mock or U1G lentiviral vector. Cell nuclei were stained with DAPI (blue). Scale bar, 5 µm. Quantification of *C9ORF72* RNA foci, represented as **c)** the mean number of RNA foci per foci-positive cells, and **d)** the percentage of RNA foci-positive cells. Mean±SEM; paired t-test (n=3, >100 cells were analyzed for each condition). ****p<0.0001, *** p<0.001, ** p<0.01, * p<0.05.

4. Axonal transport in mutant *KIF5A* patient-derived iPSC

4.1. Generation and characterization of mutant KIF5A iPSC derived from a HSP patient and its isogenic iPSC line

Given the central role of axonal transport in ALS, we aimed to elucidate the biological impact of *KIF5A* gene mutations which, based on their localization in the gene, are specifically associated to ALS (C-term cargo-binding domain) or to HSP (N-term microtubule-binding domain). Our collaborator Dr. Franco Taroni (Istituto Neurologico "Carlo Besta", Milan) recently identified a novel *KIF5A* missense mutation (p.R17Q) in the N-term region at the predicted ATP-binding domain in heterozygous state, in a HSP patient. We reprogrammed the HSP patient's fibroblasts into iPSC using the CytoTune®-iPS 2.0 Sendai kit as described in Materials and Methods section, and we obtained 9 mutant *KIF5A* iPSC clones. One iPSC clone was selected to perform gene editing by CRISPR/Cas9 to generate the isogenic *WT KIF5A* iPSC line (Iso), as well as an iPSC line with a loss-of-function mutation (Lof) (p.Asn20Lysfs*4) in heterozygous state, as confirmed by Sanger sequencing (**Fig. 16a**). Cytogenetic analysis by G-banding confirmed a normal karyotype and no gross rearrangements in the generated *KIF5A* iPSC lines and its gene-edited derivatives (data not shown). All *KIF5A* iPSC lines tested positive for the expression of specific stemness markers by both immunofluorescence (TRA-1-60, SSEA-4) (**Fig. 16b**) and RT-PCR (OCT3/4, SOX2 and NANOG) (**Fig. 16c**), confirming their proper reprogramming.

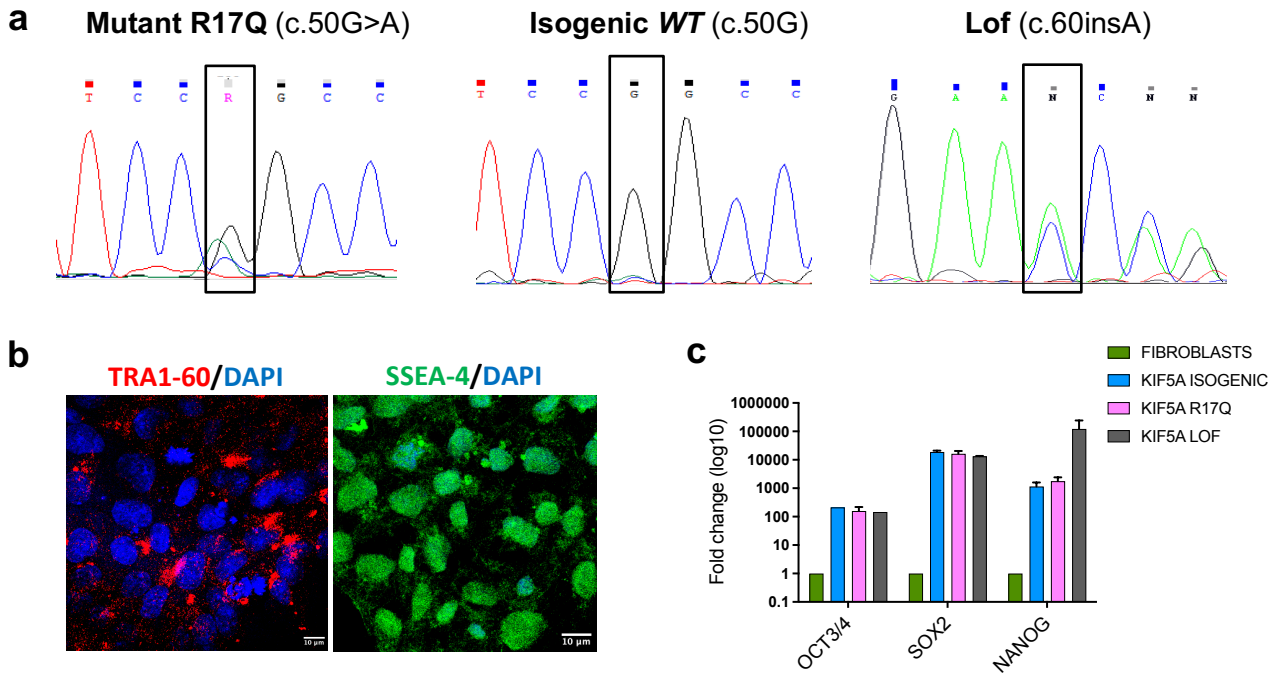

Fig.16 Generation and characterization of mutant *KIF5A* (p.R17Q), isogenic *WT* and loss-of-function iPSC lines. **a)** DNA electropherograms of the *KIF5A* R17Q, isogenic *WT* and Lof iPSC. **b)** Representative image showing the expression of TRA-1-60 (red) and SSEA-4 (green) markers by IF. Cell nuclei were stained with DAPI (blue). Scale bar,10 µm. **c)** Expression of the stemness transcription factors OCT3/4, SOX2 and NANOG by qPCR in patient's fibroblasts and in the isogenic *WT*, mutant R17Q and lof *KIF5A* iPSC-MN, normalized to markers expression in *KIF5A* fibroblasts (n=1).

4.2. Evaluation of KIF5A protein level and distribution in iPSC-motoneurons

We differentiated the three *KIF5A* iPSC lines into iPSC-MN as described in **Fig. 4a**. At day 34 of MN differentiation, the isogenic *WT*, mutant R17Q and Lof *KIF5A* motoneurons were tested for the expression of specific neuronal (SMI312, MAP2 and βIII-tubulin) and motoneuronal markers by IF (HB9) (**Fig. 17a**) by RT-PCR (ChAT) (**Fig. 17b**). The positivity for all these markers proved the successful differentiation of all the KIF5A iPSC lines into MN.

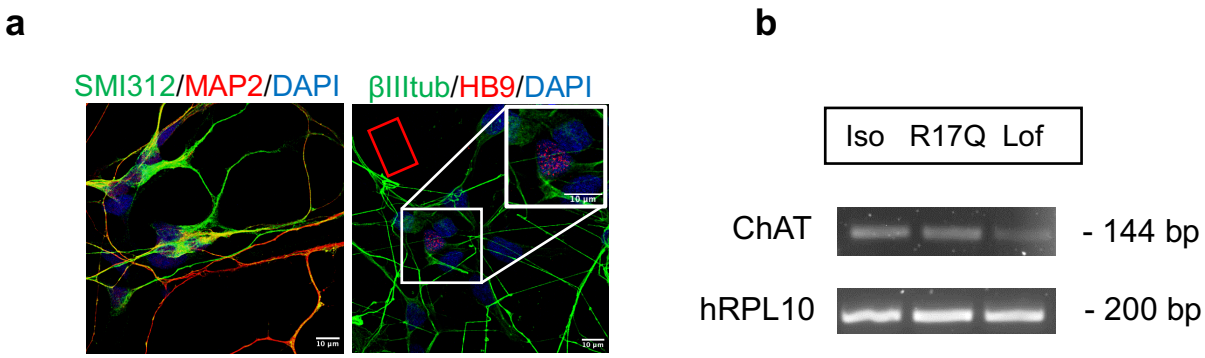

Fig.17 Characterization of *KIF5A* iPSC-MN. a) Representative images of differentiated *KIF5A* iPSC-MN expressing neuronal markers SMI312 (green), MAP2 (red) and βIII-tubulin (green) and the specific motoneuronal marker HB9 (red) by IF. Cell nuclei were stained with DAPI (blue). Scale bar, 10 μm. **b)** Expression of the specific motoneuronal marker ChAT in *KIF5A* isogenic *WT*, mutant R17Q and Lof iPSC-MN by RT-PCR (n=1).

To assess if *KIF5A* R17Q mutation could impair the stability of KIF5A protein, we next indirectly analyzed KIF5A protein levels by western blot (WB). The mutant R17Q *KIF5A* iPSC-MN didn't show any difference compared to the isogenic *WT* line, whereas in the Lof iPSC-MN KIF5A protein content was significantly reduced by half, as expected (**Fig. 18a**). Since KIF5A is involved in the axonal anterograde transport, we investigated whether R17Q *KIF5A* mutation is associated with alterations in the distribution of KIF5A protein along neurites. To this purpose, we performed IF staining for KIF5A protein and we measured the mean fluorescence intensity (MFI) in different areas: soma, neurite segments nearby soma (5-20 μm long) and neurite segments far ~50 μm from the soma (40-60 μm long), normalizing all values to the isogenic *WT KIF5A* iPSC-MN (**Fig. 18b**). We then calculated the ratio of the KIF5A MFI localized nearby soma and the KIF5A MFI of the soma to evaluate the fraction of KIF5A protein which is able to exit from the soma cytoplasm into neurites (**Fig. 18c**). Lof iPSC-MN showed a significant reduction in the quantity of KIF5A protein localized in the proximity of the cell soma compared to the isogenic *WT* and the mutant iPSC-MN (**Fig. 18c**). To assess the ability of the mutant and Lof KIF5A protein to distribute along neurites, we also determined the ratio between KIF5A MFI nearby soma and along neurites

(**Fig. 18d**). We observed a decreased ratio of KIF5A protein level in the proximity of the soma in Lof iPSC-MN compared to control WT and mutant R17Q *KIF5A* iPSC-MN, although the difference was significant only compared to the mutant R17Q *KIF5A* iPSC-MN, suggesting that Lof *KIF5A* iPSC-MN have an increased KIF5A distribution along neurites (**Fig. 18d**). These results overall suggest that *KIF5A* haploinsufficiency, but not the R17Q mutation, can impact on KIF5A distribution in iPSC-MN neurites.

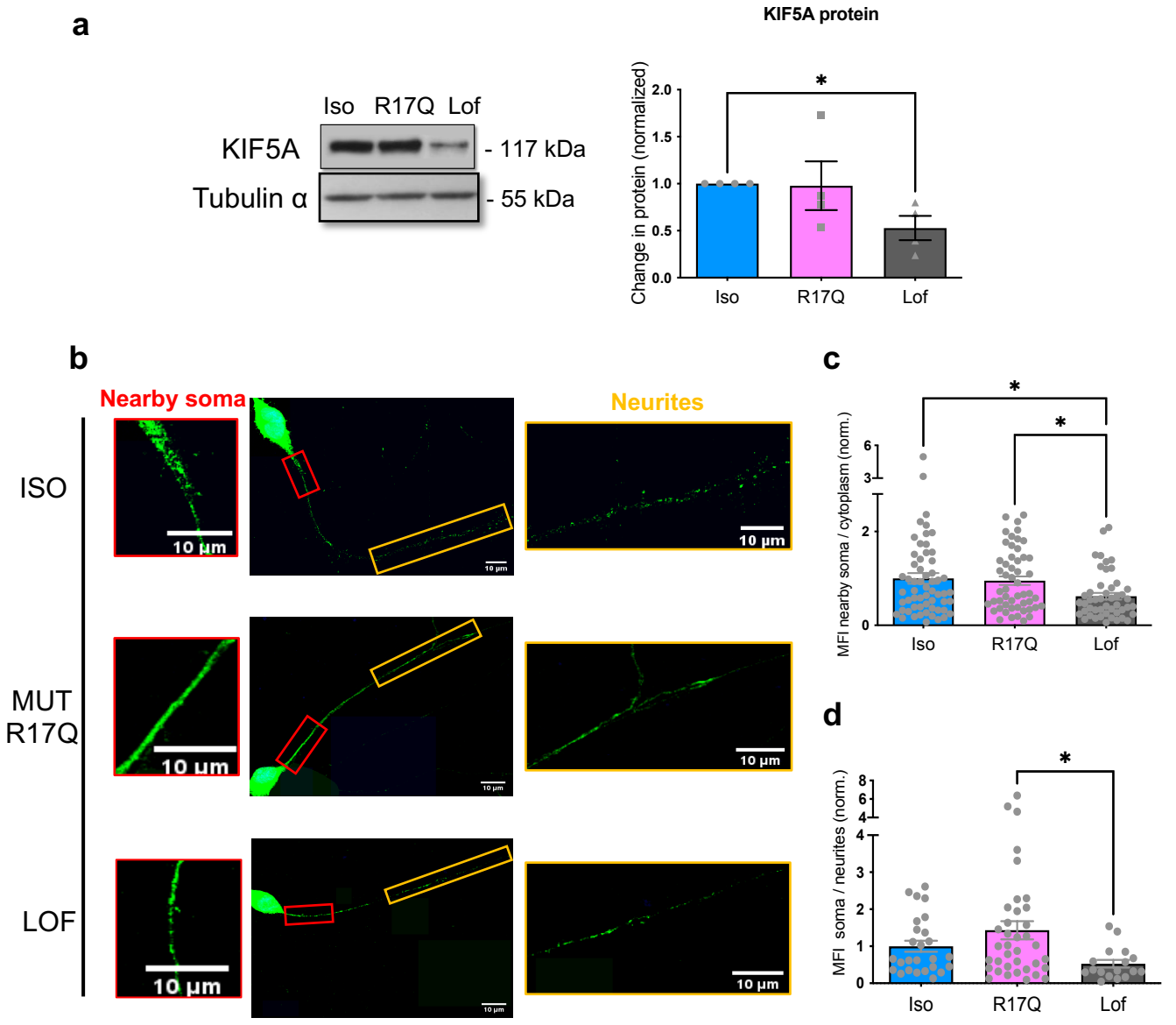

Fig.18 KIF5A protein level and distribution in iPSC-MN. a) KIF5A protein expression in isogenic *WT*, mutant R17Q and Lof *KIF5A* iPSC-MN by WB (on the left). Quantitative analysis of KIF5A protein, normalized to the isogenic *WT KIF5A* iPSC-MN values. MEAN±SEM; one-way ANOVA, Kruskal-Wallis test (n=4) (on the right). **b)** Staining of KIF5A (green) by IF. Cell nuclei stained with DAPI (blue). Scale bar, 10 µm. KIF5A distribution was analyzed in different neuronal areas (nearby soma, soma and neurites) in isogenic *WT*, mutant R17Q and Lof *KIF5A* iPSC-MN. **c)** Ratio of KIF5A mean fluorescence intensity (MFI) in segments nearby soma (5-20 µm long) over the soma cytoplasm. **d)** Ratio of the KIF5A MFI in segments nearby soma over the segments in neurites far ~50 µm from the soma (40-60 µm long). All measurements were normalized to the isogenic *WT KIF5A* iPSC-MN values. Mean±SEM; one-way ANOVA, Kruskal-Wallis test (n=3, ~15 cells/line were analyzed). ****p<0.0001, *** p<0.001, ** p<0.01, * p<0.05.

4.3. Analysis of mitochondria dynamics and transport in KIF5A iPSC-motoneurons

Since KIF5A is involved also in the anterograde axonal transport of mitochondria (63), we investigated the impact of *KIF5A* mutation on mitochondrial morphology, density and transport velocity. It is known that defects in neuronal mitochondrial morphology are linked to HSP and that mitochondrial morphology depends on mitochondrial dynamics (146). To this end, we treated iPSC-MN with the mitochondrial stain Mitotracker Red CMX Ros and we analysed mitochondria morphology within neurite segments distinguishing them in two groups, similarly to our previous analysis: nearby soma (5-20 μm long) and far ~50 μm from the soma (40-60 μm long) (**Fig. 19a**).

We calculated the mitochondrial aspect ratio (AR) (width/height), a commonly used quantitative parameter of mitochondrial dynamics. We observed a significant higher AR in both mutant R17Q and Lof *KIF5A* iPSC-MN, both nearby the soma and along neurites (**Fig. 19b**), suggesting an impact of *KIF5A* mutation on mitochondrial morphology.

To investigate the mitochondrial density parameter, we calculated the ratio of the total area occupied by the mitochondria in a specific segment over the total segment area, using the "analyse particle" function of *ImageJ* software. The results showed a trend, although not significant, of an increased mitochondrial density nearby soma in both mutant R17Q and Lof *KIF5A* iPSC-MN compared to isogenic *WT* iPSC-MN (**Fig. 19c**). The mitochondrial density along neurites was instead similar in all the analysed *KIF5A* iPSC-MN (**Fig. 19c**). In order to study the mitochondrial transport velocity, we set up and preliminary performed time-lapse imaging assays, after treating iPSC-MN with Mitotracker Red CMX Ros for 15 minutes at dark (**Fig. 19d, left**). Images (time=5min, frame count=2sec) were then analysed by the "MTrackJ" plug-in of ImageJ software. We preliminary observed no differences between the three *KIF5A* iPSC-MN (n=1) (**Fig. 19d, right**). Although further statistical confirmation is needed, our data suggest that neither the R17Q *KIF5A* mutation nor haploinsufficiency seem to impact on the transport velocity of the motile mitochondria.

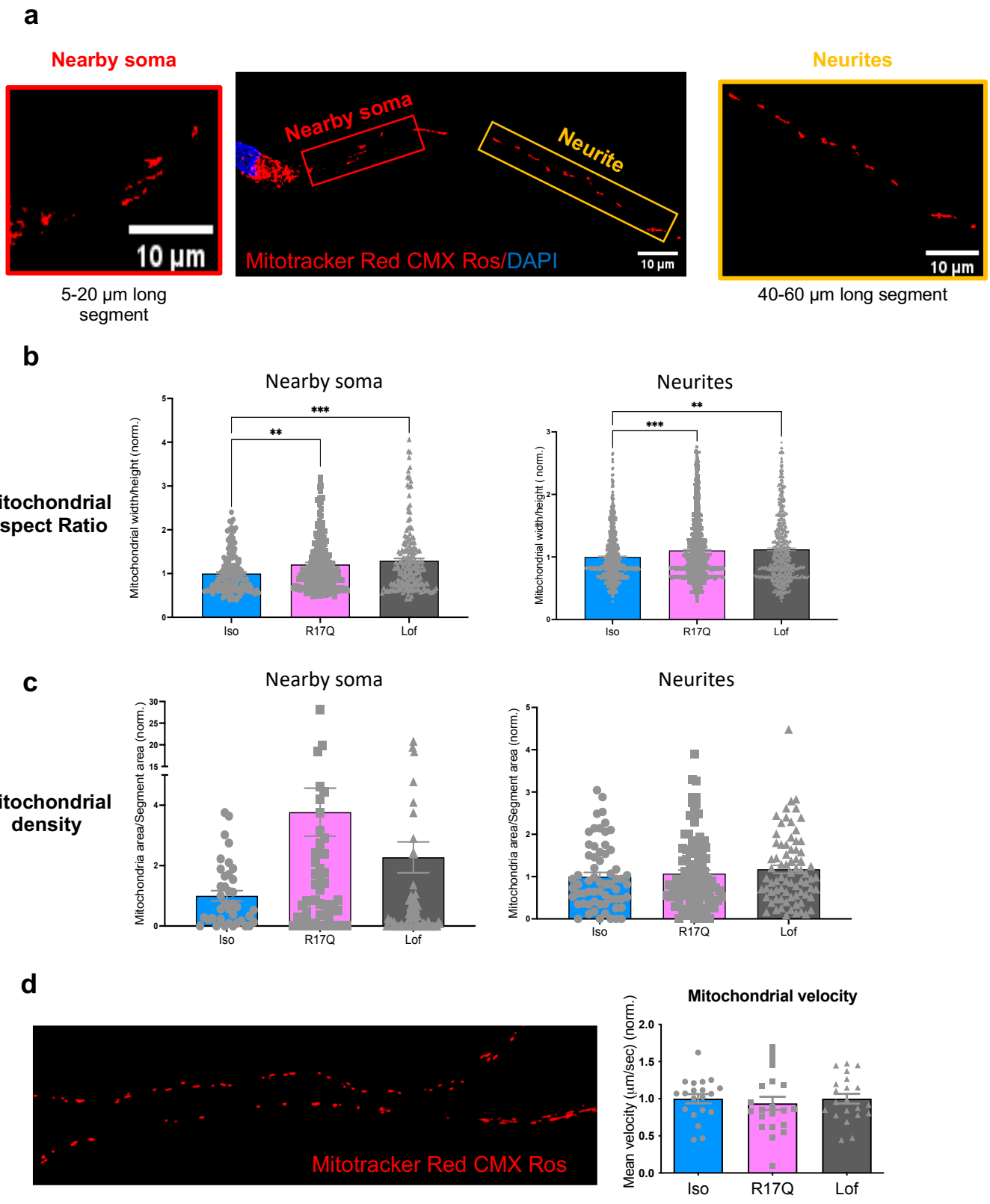

Fig. 19 Mitochondrial dynamics transport in *KIF5A* iPSC-MN. a) Representative images of *KIF5A* iPSC-MN treated with Mitotracker Red CMX Ros 10 nM (red) for 15 minutes at dark. Cell nuclei stained with DAPI (blue). Scale bar,10 µm. Different areas were selected: neurite segments near the soma (5-20 µm long) and neurite segments far ~50 µm from the soma (40-60 µm long). **b)** Analysis of mitochondrial aspect ratio in isogenic *WT*, mutant R17Q and Lof *KIF5A* iPSC-MN, nearby soma (left) and along neurites (right). **c)** Analysis of mitochondrial density in isogenic *WT*, mutant R17Q and Lof *KIF5A* iPSC-MN, nearby soma (left) and along neurites (right). All measurements were normalized to the isogenic *WT KIF5A* iPSC-MN values. Mean±SEM; one-way ANOVA, Kruskal-Wallis test (n=3, ~50 neurite segments/line were analyzed). **d)** Time-lapse imaging with Mitotracker Red CMX Ros (red) (left) and quantitative analysis of the mitochondrial transport velocity in isogenic *WT*, mutant R17Q and Lof *KIF5A* iPSC-MN. Mean±SEM; one-way ANOVA, Kruskal-Wallis test (n=1, n= ~10 mitochondria/line). ****p<0.0001, *** p<0.001, ** p<0.01, * p<0.05.

DISCUSSION

Patient-derived iPSC have revolutionized the field of neurodegenerative disease modelling, as they provide an ideal *in vitro* platform to conduct functional studies of multifactorial disorders whose genetic causes are hard to model in any other experimental model.

In this PhD project we successfully used iPSC and differentiated iPSC-MN derived from different ALS patients carrying *C9ORF72* gene mutation to study some ALS pathomechanisms associated to DNA damage, DNA damage response and actin cytoskeleton modulation, and to test a novel therapeutic approach to counteract *C9ORF72* pathology. We also established new iPSC lines from a HSP patient carrying a novel mutation in *KIF5A* gene, thus generating *in vitro* models to investigate *KIF5A*-specific defects in ALS and HSP disorders.

Modelling *C9ORF72* pathology *in vitro* and *in vivo* is still very challenging because mutated patients may carry HRE of different size and so far the link between repeat expansion length and clinical phenotype is not so clear in ALS/FTD if compared to other repeat expansion disorders. The use of *C9ORF72* patient-derived iPSC has the advantage to reproduce *in vitro* the high variability observed in HRE size (>30-4000 units) and, given the high somatic mosaicism, to obtain iPSC clones carrying different HRE length from the same patient as we recently showed (147).

When we characterized our three *C9ORF72* patient-derived iPSC lines with different HRE size (150-1200 units), we observed that they recapitulate the formation of pathological HRE-containing RNA foci, even if at a different extent among the three *C9ORF72* iPSC lines as regards both the number of RNA foci/cell and the percentage of cells with RNA foci. RNA foci are an important hallmark of *C9ORF72* pathology as they are detectable in all tissues and cells, including peripheral blood leukocytes and fibroblasts, in contrast to DPR which are brain- and testis-specific (19,148,149). In our *C9ORF72* iPSC cohort, RNA foci formation seems not to directly correlate with HRE length, an issue which is still unclear in literature (43,46). Epigenetic modifications, including *C9ORF72* promoter methylation, were shown to down-regulate the expression of the V1 and V3 isoforms that give rise to RNA foci and therefore they might contribute to influence RNA foci formation, regardless HRE size.

In our study we used iPSC derived from two healthy patients as controls who were already tested for the absence of pathogenetic variants in 30 ALS gene by next generation sequence (NGS) gene panel in our lab. The use of an appropriate control line is important when using iPSC but, in the case of *C9ORF72* HRE, it is particularly difficult to excise the large HRE by conventional CRISPR/Cas9 technology, in contrast to point mutations, in order to obtain

isogenic lines with the same genetic background. Moreover, given the nature of the *C9ORF72* mutation and the so far unknown genetic/epigenetic factors that can influence RNA foci formation and DPR synthesis, the use of iPSC lines from different patients with different HRE and genetic assets may represent a valuable experimental design to take this high variability into account. Nonetheless, two groups have recently reported the generation of isogenic iPSC lines from their *C9ORF72* iPSC lines using CRISPR/Cas9-mediated HDR to replace the pathogenic expansion with a donor template carrying a normal HRE repeat size, thus providing further models to study the effects of HRE in the same genetic background of the original mutant *C9ORF72* iPSC (150,151).

In this project, to study DNA damage and DDR, we decided to first differentiate our *C9ORF72* iPSC lines into NSC before generating motor neurons, a process that is time-consuming and expensive. iPSC-NSC have the advantage, compared to the pluripotent iPSC, to be still multipotent, but already committed towards a neural phenotype, and can be further differentiated into neurons and glial cells (152). We used the phosphorylated H2AX at Ser 139 (γH2AX) as the most effective readout to detect the DNA breakage foci, indicative of both the extent of DNA damage and the recruitment of proteins involved in DDR (153). Our results showed that *C9ORF72* mutation did not impact either on DNA damage at physiological lever or on DDR after treatment with the genotoxic agent neocarzinostatin (NCS) compared to *wild-type* cells. Of note, we observed a high percentage of both *C9ORF72* and control iPSC-NSC positive for γH2AX in basal conditions (70-85%), suggesting that these cells, although more committed towards a neuronal phenotype compared to iPSC, still remain actively dividing stem cells that intrinsically undergo genomic damages. This could also explain why iPSC-NSC require at least 8 hours to recover from DNA damage induction and to recruit factors that mediate the resolution of the damage. We hypothesize that the already compromised genomic stability in the highly-mitotic iPSC-NSC could mask the possible effect of *C9ORF72* mutation on DDR. To support this idea, a previous study also reported that iPSC derived from an ALS *C9ORF72* patient did not show increased DNA damage, neither at basal condition nor after DNA damage induction with γ-irradiation, compared to iPSC derived from *wild-type* healthy individuals (82). Differences emerged instead in differentiated iPSC-MN, suggesting that post-mitotic and more differentiated cells would be more vulnerable to DNA damage than the actively dividing iPSC (82).

When we differentiated the three *C9ORF72* and the two wild-type iPSC lines into motor neurons using a modified protocol from Amoroso et al (143) for 34 days (day 13 from EB

dissociation), we, too, observed a higher extent of DNA damage in *C9ORF72* iPSC-MN compared to controls, confirming that *C9ORF72* mutation confers susceptibility to an increased genomic instability in post-mitotic neurons. However, both *C9ORF72* and control iPSC-MN were able to recover from the induced DNA damage after 6-hours rescue with no differences between them. This result seems instead to be in contrast with the one previously reported by Higelin et al where they found an impaired rescue of *C9ORF72* iPSC-MN 24 hours after the genotoxic γ-radiation treatment compared to *wild-type* cells (82).

As ALS is an age-related disease, it is important to assess if DNA damage is also age-dependent *in vitro* by using a differentiation protocol that mimics, as close as possible, the motoneuronal aging process. Regarding this issue, Lopez-Gonzalez et al indeed observed increased DNA damage levels in 4-months-old *C9ORF72* iPSC-MN generated using a modified protocol by Amoroso compared to control cells, while these differences were absent in younger, 2-weeks old, iPSC-MN (81,143). However, by using another differentiation protocol (154), Lopez-Gonzalez et al described the presence of a higher DNA damage level in 2-months old *C9ORF72* iPSC-MN, that was absent in 1-month old iPSC-MN (81). Higelin et al (82) found similar results after 42 days of MN differentiation using another modified protocol (155). Although the protocols used in all these articles and in our experiments to obtain MN are different and therefore the time points can not be compared, our 34-days old iPSC-MN could be still too young to see the effect elicited by *C9ORF72* mutation on DNA repair mechanisms as observed by Higelin et al (82). We therefore cultured *C9ORF72* iPSC-MN for a longer time until day 56 (day 23 from EB dissociation) and at this differentiation time we observed that, although *C9ORF72* iPSC-MN were able to rescue the induced DNA damage after 6 hours, they still presented a significant higher level of DNA damage compared to control cells, suggesting that *C9ORF72* mutation affects the ability of aged iPSC-MN to respond efficiently to induced DNA damage.

A limitation we encountered in maintaining prolonged *in vitro* cultures is the propensity of iPSC-MN to detach from the substrate, as they tend to fuse into large cell clusters with their processes fasciculated and organized into well-defined bundles (156). To further assess if aging is an importan factor in DDR, different methods that ameliorate iPSC-MN survival *in vitro* are now available, such as the use of dendritic polyglycerol amine (dPGA)-coated dishes as a substrate for culturing iPSC-MN(156) or the establishment of co-cultures with Schwann cells, that can release trophic factors ameliorating MN viability and axon growth (157).

Overall, we here report a detailed assessment of the impact of *C9ORF72* mutation on genomic integrity in patient-derived iPSC and iPSC-motoneurons based on γH2AX measurements as effective readout to detect DNA damage and DDR. We, however, plan to confirm our data investigating other DNA damage markers such as p-ATM, p-ATR and BP53 and to also elucidate if different DDR downstream pathways are affected by *C9ORF72* mutation.

During my 3-months internship in the USA, I studied if modulation of F-actin cytoskeleton dynamics might mediate and influence DNA damage and DDR. For this purpose, I used one *C9ORF72* and one isogenic *wild-type* i^3-iPSC lines already available in the host lab, that rely on the i^3 system that has been recently developed (144). It consists in the stable integration of the transcription factor Neurogenin 2 (*NGN2*) cassette into a safe-harbour site in the genome by iPSC transfection. By inducing *NGN2* expression by doxycycline, it is possible to obtain iPSC-cortical neurons in a very efficient and rapid way in only 14 days compared to 1-3 months of classical methods with a 100% culture purity (144).

For this reason, i^3-iPSC technology seems to overcome many limitations of the available protocols, making neuronal differentiation more standardized and implemented. However, the NGN2 cassette needs to be inserted in each iPSC line to be studied and this can represent a limit if handling several iPSC lines from different patients.

Previous work suggested an important effect of cytoskeleton alterations on nuclear activity and structure, including DNA damage induction (107,158), but if these mechanisms occur also in post-mitotic neurons is still unknown. We observed that both *C9ORF72* and the isogenic i^3-cortical neurons (i^3-CN) show a similar level of DNA damage at basal level, in contrast to what occurs in iPSC-MN. For this reason, i^3-CN represent a suitable model to study the effects of F-actin modulation on DNA damage and DDR in the two *C9ORF72* mutant and *wild-type* genetic backgrounds.

To modulate F-actin cytoskeleton, different kind of drugs were already used in literature. Formin proteins and CK66 molecule mediate the polymerization of unbranched or branched actin filaments by Arp2/3 induction or inhibition, respectively (159,160). Cytochalasin D and Latrunculin toxins are produces by fungi and sponges to promote the depolymerization of F-actin filaments (161). Rock inhibitor and Caliculin reduce or promote the interaction between F-actin and myosin, respectively (162,163).

For our purposes, we decided to use the formin agonist Intramimic drug (IMM01) and Latrunculin B (LATRB) to study the effects of two opposing actin modifier drugs on DDR. We observed that, while treatment of isogenic i^3-CN with both drugs caused a similar

increase of DNA damage, in *C9ORF72* i^3-CN both drugs were ineffective in influencing DDR. These data suggest that modulation of F-actin cytoskeleton may affect how the healthy neuron is capable of responding to DNA damage, while in *C9ORF72* i^3-CN the actin cytoskeleton may be already compromised and unable to respond to actin modifiers.

Of note, previous works have already demonstrated an alteration of the F-actin cytoskeleton dynamics in patient-derived *C9ORF72* fibroblasts and iPSC-neurons (103,104), but the molecular mechanisms linking *C9ORF72* mutation to actin cytoskeleton defects are currently unknown. We here reinforced the evidence of an impaired F-actin cytoskeleton dynamics linked to *C9ORF72* mutation and DDR. We also found that F-actin remodeling may influence chromatin remodeling by increasing H3K9me3 levels in both *C9ORF72* and isogenic i^3-CN. However, H3K9me3 is an epigenetic marker specifically associated with the formation of heterochromatin and gene silencing at the periphery of the nucleus (164) so that the study of other types of epigenetic markers will be necessary to understand the global epigenetic changes in the chromatin induced by actin cytoskeleton remodeling.

We hypothesize that the LINC complex could represent the mechanistic connection between actin cytoskeleton dynamics and nuclear changes, including DNA damage and chromatin remodeling, because it physically interacts with the nuclear lamina and DNA from the nucleoplasmic side and to the cytoskeleton on the cytoplasmic side (105). Future experiments will aim at further investigating the role of this complex in the crosstalk between cytoskeleton forces and nuclear alterations in *C9ORF72* patient-derived iPSC-neurons.

In the third part of my work I tested the efficacy of a novel RNA-based therapeutic approach to modulate the pathological transcript in *C9ORF72* iPSC-MN. A personalized therapy in *C9ORF72* mutation carriers must target the HRE-containg transcripts and up to date some antisense oligonucleotides (ASO) and small molecules have proven to be effective in *in vitro* and *in vivo* disease models (95,127,137,138,142). Since the BIIB078 ASO has been recently withdrawn from phase II clinical trial by Biogen and the WVE-004 trial is still ongoing, effective therapeutic approaches are needed and the field is still open to research.

In 2012 the group of our collaborator Dr Franco Pagani (ICGEB, Trieste) optimized a novel strategy to correct splicing defects based on modified U1 small nuclear RNA (U1 snRNA), part of the small nuclear ribonucleoprotein particles (snRNP). These modified U1 snRNA are designed to bind, by complementarity, to intronic sequences downstream the 5' splice site so to improve exon-intron definition and correct exon skipping caused by different types of mutations (165). In more recent years, they applied this strategy to several diseases, including spinal muscular atrophy, cystic fibrosis, Netherthon syndrome (a genodermatosis),

haemophilia B and familial dysautonomia characterized by splicing defects (166–170). One important aspect of this U1 snRNA molecules is represented by the possibility to insert the modified U1 snRNA cassette (650 pb) into viral vectors, which are currently used in gene therapy. AAV vectors, in particular, have long-lasting expression in post-mitotic cells including motor neurons, and AAV9-U1s have already been shown to be effective and safe in a mouse model of the motor neuron disease Spinal Muscle Atrophy (171,172).

In collaboration with Dr Franco Pagani we therefore proposed to use the modified U1 snRNA as an alternative therapeutic strategy for *C9ORF72* pathology in ALS/FTD patients. U1 snRNA have been designed to identify and directly bind the *C9ORF72* repeat sequence in the pre-mRNA by means of their engineered 5' tail. In particular, the U1C and U1G snRNA were generated to bind the *C9ORF72* pre-mRNA 4 nucleotides before the HRE with two different binding efficiencies. In this condition, the U1 snRNA were hypothesized to act, not as splicing promoting factors, but more like ASO, favoring the degradation of the nascent pathological transcripts.

Our pilot results in HEK293T cells expressing the pathological HRE showed that both U1C and U1G constructs lead to a significant decrease in both the number of *C9ORF72* RNA foci and DPR formation. Using iPSC-MN from a *C9ORF72* patient carrying 1200 repeat units, we obtained very promising results about the ability of U1 snRNA to reduce RNA foci formation. Many groups are currently using the quantification of RNA foci number as the most effective readout to evaluate the effectiveness of gene targeting therapies (127,138). However, it is to be kept in mind that RNA foci formation has never been correlated to a worse clinical phenotype in *C9ORF72* patient's tissue or cells, supporting the observation that the gain of function mechanism by toxic RNA aggregation does not exclusively cause the pathology (43). For this reason and to further confirm our results, we plan to further test the efficacy of U1 snRNA in other patient-derived *C9ORF72* iPSC already available in the lab and carrying different HRE length. Moreover, the measurement of the dipeptide proteins polyGP by Meso Scale Discovery (MSD) assay, optimized in Prof. Petruccelli's lab, will allow us to assess U1 snRNA efficacy on reducing also RAN translation in iPSC-MN. We will also evaluate the possible genome-wide off-target effects of U1 snRNA by RNA seq analysis. We do not expect widespread effects on gene expression also because the group of Dr Pagani has previously assessed the specificity of modified U1 snRNA for *SMN2* gene splicing in mouse spinal cord (173) and in human cells (172), where they found altered expression of only few genes. Overall, we believe that the results we obtained in *C9ORF72* iPSC-MN are promising and that this novel therapeutic strategy has the potential to

counteract the main defects associated to *C9ORF72* HRE in ALS and FTD patients with long-lasting effects.

In the last part of my work I established a new iPSC line derived from a HSP patient carrying a novel mutation in the N-terminal domain of *KIF5A* gene, found by a targeted NGS screening conducted by the group of our collaborator Dr Franco Taroni (Istituto Neurologico Carlo Besta, Milan) to identify new variants in a large cohort of patients with neurodegenerative and neurodevelopmental disorders. The purpose of this part of my thesis was to investigate the mechanisms whereby *KIF5A* gene variants in the cargo binding C-terminal or in the motor N-terminal protein domains cause different neurodegenerative diseases, ALS and HSP, respectively. For this reason, we also aim to obtain iPSC carrying *KIF5A* mutations in the C-terminal cargo-binding domain derived from ALS patients or, if not available, from *wild-type* iPSC in which the *KIF5A* mutation will be introduced by CRISPR/Cas9 technology as described by Baron et al (60). Indeed, for my PhD project I have already gene-edited the iPSC line carrying the novel *KIF5A* p.R17Q varinat to both correct the mutation into a *wild-type* sequence (isogenic) and to create a loss-of-function mutation (lof) using recombinant Cas9 protein and specific RNA guides.

When we differentiated the three iPSC lines obtained into MN, we observed a similar differentiation efficiency. However, preliminary semi-quantitative RT-PCR results seem to suggest a reduced ChAT mRNA level in *KIF5A* lof iPSC-MN, even if more analysis will be necessary to confirm these data. Previous findings showed a remarkable decrease of axonal and dendrites outgrowth and of axonal branches number in motor neurons from *KIF5A* knock-out mice, but not in heterozygous *KIF5A* +/– motor neurons (64). Therefore, further analysis will be necessary to assess if KIF5A protein content is important for neuronal differentiation and maintenance of neuronal functions in human motor neurons.

KIF5A p.R17Q is a novel mutation mapping in the ATP-binding domain and whether it causes HSP by a loss of function or a dominant negative mechanism is unknown. To assess if the allelic p.R17Q and lof mutations could impair the ability of KIF5A protein to be correctly processed and matured, we preliminarily analysed KIF5A protein content by western blot in iPSC-MN. Our results showed that KIF5A protein level is not changed in p.R17Q iPSC-MN, suggesting that the mutation does not cause any degradation of the protein. However, to better evaluate KIF5A protein stability, we plan to perform the cycloheximide chase assay which allows to evaluate KIF5A protein levels at different time points from protein synthesis inhibition.

There is large body of evidence that mitochondrial abnormalities are among the primary cell defects underlying both ALS and HSP, and it is known that KIF5A is involved in the anterograde transport of mitochondria mainly via the adaptor Milton-Miro complex, as previously showed in Drosophila and zebrafish models (63,174). Interestingly, motor neurons from *KIF5A* knock-out mice display mitochondrial axonal transport deficits and reduced survival (64). Defects in mitochondrial morphology are already linked to HSP disease (175) and they correlate with mitochondrial dynamics events of fusion and fission (146). Therefore, we investigated the impact of *KIF5A* mutation on mitochondria morphology, density and velocity. When we analysed mitochondrial aspect ratio (AR; width/height), a commonly used quantitative parameter of mitochondrial dynamics, our results showed an increased AR value in both *KIF5A* p.R17Q and lof iPSC-MN, indicating more elongated mitochondria and a likely unbalance between fusion and fission mechanisms in favor of fusion.

The analysis of the mitochondrial density showed a trend to an increased mitochondrial density near the soma in both *KIF5A* p.R17Q and lof iPSC-MN compared to *wild-type* isogenic iPSC-MN. The possible accumulation of mitochondria in the proximity of cell soma could indicate an impaired transport of mitochondria mediated by the mutant *KIF5A*, suggesting a loss of function mechanism also for the missense p.R17Q variant. Indeed, this result is supported by the evidence that deficiency in *KIF5A* expression correlates with an accumulation of phosphorylated neurofilaments and amyloid precursor protein in the neuronal cell bodies of patients with multiple sclerosis (176). We also evaluated if the neuronal distribution of the N-terminal mutant *KIF5A* reflected the high mitochondrial density near the cell soma and we observed a similar localization of the mutant KIF5A both nearby the cell soma and along neurites compared to the isogenic iPSC-MN.

Conversely, it has recently reported that N2A cells overexpressing C-term mutant *KIF5A* displayed an increased accumulation of KIF5A within distal neurites compared to *wild-type KIF5A*, indicating that ALS-mutant *KIF5A* results in a hyperactive kinesin motor protein conferring a toxic gain of function (60). The Authors further confirmed this hypothesis showing a higher percentage of moving mitochondria and an increased anterograde, but not retrograde, velocity in cells overexpressing the C-term mutant versus the *wild-type* (60). Mutation in the N-term domain of *KIF5A* gene (N256S) have instead been associated to a defective anterograde and retrograde flux of mitochondria, but not to a different mitochondrial velocity compared to *wild-type KIF5A* in a Drosophila model (123). Also,

studies conducted in heterozygous *KIF5A* mice did not show significant difference in the mean mitochondrial velocity compared to *wild-type* mice (64).

We conducted time-lapse live imaging assays to assess mitochondria velocity and we did not find any difference in the three iPSC-MN lines although further replicates are needed to confirm these data (n=1). To better characterize the functional effects of mutant *KIF5A*, we also plan to differentiate *KIF5A* iPSC into iPSC-MN using microfluidic devices that are already exploited to properly track trafficking of several cargoes along axons, such as lysosomes, and/or to study axonal degeneration (177,178). Given that KIF5A is involved in the transport of multiple RNA-binding proteins (179), we will also analyze TDP-43 and other RNA-binding proteins (i.e. FMRP, SFPQ, HnRNPA1) movement along axons.

The generation and functional characterization of iPSC-MN from an HSP patient carrying this novel mutation in the N-terminal KIF5A domain certainly represents a personalized approach to disease modelling to help elucidate the different *KIF5A*-related pathomechanisms leading to ALS or HSP.

In conclusion, the results obtained in my PhD work strongly support the use of patient-derived iPSC and iPSC-MN as suitable *in vitro* platforms to model *C9ORF72* and *KIF5A*-related pathogenetic mechanisms in ALS disease and to test the efficacy of a novel therapeutic strategy, based on engineered U1 snRNA, to counteract *C9ORF72* pathology in ALS/FTD patients.

ACKNOWLEDGEMENTS

I wish to thank my supervisor Prof. Antonia Ratti and Prof. Vincenzo Silani for the opportunity to work on this PhD project and for their constant support and precious guidance. I am deeply blessed for having you as mentors in this journey.

I am especially grateful to Dr. Claudia Colombrita, Dr. Patrizia Bossolasco and Prof. Claudia Fallini for their help in performing and interpreting experiments and for their continue encouragement during my PhD.

A big thank also to my colleagues, past and present, for their moral support, the late-evening experiments, the coffee-breaks, and the countless laughs together.

Last but not least, I wish to deep acknowledge the PhD program in Experimental Medicine of the University of Milan for providing me with a doctoral scholarship and with all the training opportunities to build my scientific career.

REFERENCES

1. Roman GC. Neuroepidemiology of amyotrophic lateral sclerosis: clues to aetiology and pathogenesis. J Neurol Neurosurg Psychiatry. 1996 Aug 1;61(2):131–7.
2. Longinetti E, Fang F. Epidemiology of amyotrophic lateral sclerosis: an update of recent literature. Curr Opin Neurol. 2019 Oct;32(5):771–6.
3. Petrov D, Mansfield C, Moussy A, Hermine O. ALS Clinical Trials Review: 20 Years of Failure. Are We Any Closer to Registering a New Treatment? Front Aging Neurosci. 2017 Mar 22;9.
4. Saitoh Y, Takahashi Y. Riluzole for the treatment of amyotrophic lateral sclerosis. Neurodegener Dis Manag. 2020 Dec;10(6):343–55.
5. Dorst J, Genge A. Clinical studies in amyotrophic lateral sclerosis. Curr Opin Neurol. 2022 Oct;35(5):686–92.
6. Masrori P, van Damme P. Amyotrophic lateral sclerosis: a clinical review. Eur J Neurol. 2020 Oct 7;27(10):1918–29.
7. Ghasemi M, Brown RH. Genetics of Amyotrophic Lateral Sclerosis. Cold Spring Harb Perspect Med. 2018 May;8(5):a024125.
8. van Rheenen W, van der Spek RAA, Bakker MK, van Vugt JJFA, Hop PJ, Zwamborn RAJ, et al. Common and rare variant association analyses in amyotrophic lateral sclerosis identify 15 risk loci with distinct genetic architectures and neuron-specific biology. Nat Genet. 2021 Dec 6;53(12):1636–48.
9. Brown AL, Wilkins OG, Keuss MJ, Hill SE, Zanovello M, Lee WC, et al. TDP-43 loss and ALS-risk SNPs drive mis-splicing and depletion of UNC13A. Nature. 2022 Mar 3;603(7899):131–7.
10. Ma XR, Prudencio M, Koike Y, Vatsavayai SC, Kim G, Harbinski F, et al. TDP-43 represses cryptic exon inclusion in the FTD–ALS gene UNC13A. Nature. 2022 Mar 3;603(7899):124–30.
11. van Blitterswijk M, van Es MA, Hennekam EAM, Dooijes D, van Rheenen W, Medic J, et al. Evidence for an oligogenic basis of amyotrophic lateral sclerosis. Hum Mol Genet. 2012 Sep 1;21(17):3776–84.
12. Hop PJ, Zwamborn RAJ, Hannon E, Shireby GL, Nabais MF, Walker EM, et al. Genome-wide study of DNA methylation shows alterations in metabolic, inflammatory, and cholesterol pathways in ALS. Sci Transl Med. 2022 Feb 23;14(633).
13. Zago S, Lorusso L, Aiello EN, Ugolini M, Poletti B, Ticozzi N, et al. Cognitive and behavioral involvement in ALS has been known for more than a century. Neurological Sciences. 2022 Dec 2;43(12):6741–60.
14. Lillo P, Hodges JR. Frontotemporal dementia and motor neurone disease: Overlapping clinic-pathological disorders. Journal of Clinical Neuroscience. 2009 Sep;16(9):1131–5.
15. Arai T, Hasegawa M, Akiyama H, Ikeda K, Nonaka T, Mori H, et al. TDP-43 is a component of ubiquitin-positive tau-negative inclusions in frontotemporal lobar degeneration and amyotrophic lateral sclerosis. Biochem Biophys Res Commun. 2006 Dec;351(3):602–11.
16. Neumann M, Sampathu DM, Kwong LK, Truax AC, Micsenyi MC, Chou TT, et al. Ubiquitinated TDP-43 in Frontotemporal Lobar Degeneration and Amyotrophic Lateral Sclerosis. Science (1979). 2006 Oct 6;314(5796):130–3.
17. Buratti E, Baralle FE. TDP-43: gumming up neurons through protein–protein and protein–RNA interactions. Trends Biochem Sci. 2012 Jun;37(6):237–47.
18. Mitchell JC, Constable R, So E, Vance C, Scotter E, Glover L, et al. Wild type human TDP-43 potentiates ALS-linked mutant TDP-43 driven progressive motor and cortical

neuron degeneration with pathological features of ALS. Acta Neuropathol Commun. 2015 Dec 25;3(1):36.
19. DeJesus-Hernandez M, Mackenzie IR, Boeve BF, Boxer AL, Baker M, Rutherford NJ, et al. Expanded GGGGCC Hexanucleotide Repeat in Noncoding Region of C9ORF72 Causes Chromosome 9p-Linked FTD and ALS. Neuron. 2011 Oct;72(2):245–56.
20. Renton AE, Majounie E, Waite A, Simón-Sánchez J, Rollinson S, Gibbs JR, et al. A Hexanucleotide Repeat Expansion in C9ORF72 Is the Cause of Chromosome 9p21-Linked ALS-FTD. Neuron. 2011 Oct;72(2):257–68.
21. van Blitterswijk M, Mullen B, Wojtas A, Heckman MG, Diehl NN, Baker MC, et al. Genetic modifiers in carriers of repeat expansions in the C9ORF72 gene. Mol Neurodegener. 2014 Dec 20;9(1):38.
22. Bourinaris T, Houlden H. C9orf72 and its Relevance in Parkinsonism and Movement Disorders: A Comprehensive Review of the Literature. Mov Disord Clin Pract. 2018 Nov 8;5(6):575–85.
23. Galimberti D, Reif A, Dell'Osso B, Kittel-Schneider S, Leonhard C, Herr A, et al. The C9ORF72 hexanucleotide repeat expansion is a rare cause of schizophrenia. Neurobiol Aging. 2014 May;35(5):1214.e7-1214.e10.
24. Gijselinck I, Cruts M, van Broeckhoven C. The Genetics of *C9orf72* Expansions. Cold Spring Harb Perspect Med. 2018 Apr;8(4):a026757.
25. Ratti A, Peverelli S, D'Adda E, Colombrita C, Gennuso M, Prelle A, et al. Genetic and epigenetic disease modifiers in an Italian *C9orf72* family expressing ALS, FTD or PD clinical phenotypes. Amyotroph Lateral Scler Frontotemporal Degener. 2022 Apr 3;23(3–4):292–8.
26. van Mossevelde S, van der Zee J, Cruts M, van Broeckhoven C. Relationship between C9orf72 repeat size and clinical phenotype. Curr Opin Genet Dev. 2017 Jun;44:117–24.
27. Jackson JL, Finch NA, Baker MC, Kachergus JM, DeJesus-Hernandez M, Pereira K, et al. Elevated methylation levels, reduced expression levels, and frequent contractions in a clinical cohort of C9orf72 expansion carriers. Mol Neurodegener. 2020 Dec 30;15(1):7.
28. Murphy NA, Arthur KC, Tienari PJ, Houlden H, Chiò A, Traynor BJ. Age-related penetrance of the C9orf72 repeat expansion. Sci Rep. 2017 Dec 18;7(1):2116.
29. Balendra R, Isaacs AM. C9orf72-mediated ALS and FTD: multiple pathways to disease. Nat Rev Neurol. 2018 Sep 17;14(9):544–58.
30. Liu EY, Russ J, Wu K, Neal D, Suh E, McNally AG, et al. C9orf72 hypermethylation protects against repeat expansion-associated pathology in ALS/FTD. Acta Neuropathol. 2014 Oct 8;128(4):525–41.
31. Zhang D, Iyer LM, He F, Aravind L. Discovery of Novel DENN Proteins: Implications for the Evolution of Eukaryotic Intracellular Membrane Structures and Human Disease. Front Genet. 2012;3.
32. Webster CP, Smith EF, Bauer CS, Moller A, Hautbergue GM, Ferraiuolo L, et al. The C9orf72 protein interacts with Rab1a and the <scp>ULK</scp> 1 complex to regulate initiation of autophagy. EMBO J. 2016 Aug 22;35(15):1656–76.
33. Amick J, Roczniak-Ferguson A, Ferguson SM. C9orf72 binds SMCR8, localizes to lysosomes, and regulates mTORC1 signaling. Mol Biol Cell. 2016 Oct 15;27(20):3040–51.
34. O'Rourke JG, Bogdanik L, Yáñez A, Lall D, Wolf AJ, Muhammad AKMG, et al. *C9orf72* is required for proper macrophage and microglial function in mice. Science (1979). 2016 Mar 18;351(6279):1324–9.
35. Ling SC, Polymenidou M, Cleveland DW. Converging Mechanisms in ALS and FTD: Disrupted RNA and Protein Homeostasis. Neuron. 2013 Aug;79(3):416–38.

36. Ciura S, Lattante S, le Ber I, Latouche M, Tostivint H, Brice A, et al. Loss of function of C9orf72 causes motor deficits in a zebrafish model of Amyotrophic Lateral Sclerosis. Ann Neurol. 2013 Apr;n/a-n/a.
37. Waite AJ, Bäumer D, East S, Neal J, Morris HR, Ansorge O, et al. Reduced C9orf72 protein levels in frontal cortex of amyotrophic lateral sclerosis and frontotemporal degeneration brain with the C9ORF72 hexanucleotide repeat expansion. Neurobiol Aging. 2014 Jul;35(7):1779.e5-1779.e13.
38. Farg MA, Sundaramoorthy V, Sultana JM, Yang S, Atkinson RAK, Levina V, et al. C9ORF72, implicated in amytrophic lateral sclerosis and frontotemporal dementia, regulates endosomal trafficking. Hum Mol Genet. 2014 Jul 1;23(13):3579–95.
39. Aoki Y, Manzano R, Lee Y, Dafinca R, Aoki M, Douglas AGL, et al. C9orf72 and RAB7L1 regulate vesicle trafficking in amyotrophic lateral sclerosis and frontotemporal dementia. Brain. 2017 Apr 1;140(4):887–97.
40. Haeusler AR, Donnelly CJ, Periz G, Simko EAJ, Shaw PG, Kim MS, et al. C9orf72 nucleotide repeat structures initiate molecular cascades of disease. Nature. 2014 Mar 5;507(7491):195–200.
41. Fratta P, Mizielinska S, Nicoll AJ, Zloh M, Fisher EMC, Parkinson G, et al. C9orf72 hexanucleotide repeat associated with amyotrophic lateral sclerosis and frontotemporal dementia forms RNA G-quadruplexes. Sci Rep. 2012 Dec 21;2(1):1016.
42. Mori K, Arzberger T, Grässer FA, Gijselinck I, May S, Rentzsch K, et al. Bidirectional transcripts of the expanded C9orf72 hexanucleotide repeat are translated into aggregating dipeptide repeat proteins. Acta Neuropathol. 2013 Dec 17;126(6):881–93.
43. DeJesus-Hernandez M, Finch NA, Wang X, Gendron TF, Bieniek KF, Heckman MG, et al. In-depth clinico-pathological examination of RNA foci in a large cohort of C9ORF72 expansion carriers. Acta Neuropathol. 2017 Aug 15;134(2):255–69.
44. Mizielinska S, Lashley T, Norona FE, Clayton EL, Ridler CE, Fratta P, et al. C9orf72 frontotemporal lobar degeneration is characterised by frequent neuronal sense and antisense RNA foci. Acta Neuropathol. 2013 Dec 30;126(6):845–57.
45. Almeida S, Gascon E, Tran H, Chou HJ, Gendron TF, DeGroot S, et al. Modeling key pathological features of frontotemporal dementia with C9ORF72 repeat expansion in iPSC-derived human neurons. Acta Neuropathol. 2013 Sep 9;126(3):385–99.
46. Lee YB, Chen HJ, Peres JN, Gomez-Deza J, Attig J, Štalekar M, et al. Hexanucleotide Repeats in ALS/FTD Form Length-Dependent RNA Foci, Sequester RNA Binding Proteins, and Are Neurotoxic. Cell Rep. 2013 Dec;5(5):1178–86.
47. Gendron TF, Bieniek KF, Zhang YJ, Jansen-West K, Ash PEA, Caulfield T, et al. Antisense transcripts of the expanded C9ORF72 hexanucleotide repeat form nuclear RNA foci and undergo repeat-associated non-ATG translation in c9FTD/ALS. Acta Neuropathol. 2013 Dec 16;126(6):829–44.
48. Ash PEA, Bieniek KF, Gendron TF, Caulfield T, Lin WL, DeJesus-Hernandez M, et al. Unconventional Translation of C9ORF72 GGGGCC Expansion Generates Insoluble Polypeptides Specific to c9FTD/ALS. Neuron. 2013 Feb;77(4):639–46.
49. Kwon I, Xiang S, Kato M, Wu L, Theodoropoulos P, Wang T, et al. Poly-dipeptides encoded by the *C9orf72* repeats bind nucleoli, impede RNA biogenesis, and kill cells. Science (1979). 2014 Sep 5;345(6201):1139–45.
50. Boeynaems S, Bogaert E, Kovacs D, Konijnenberg A, Timmerman E, Volkov A, et al. Phase Separation of C9orf72 Dipeptide Repeats Perturbs Stress Granule Dynamics. Mol Cell. 2017 Mar;65(6):1044-1055.e5.
51. Brenner D, Yilmaz R, Müller K, Grehl T, Petri S, Meyer T, et al. Hot-spot KIF5A mutations cause familial ALS. Brain. 2018 Mar 1;141(3):688–97.

52. Nicolas A, Kenna KP, Renton AE, Ticozzi N, Faghri F, Chia R, et al. Genome-wide Analyses Identify KIF5A as a Novel ALS Gene. Neuron. 2018 Mar;97(6):1268-1283.e6.
53. Reid E, Kloos M, Ashley-Koch A, Hughes L, Bevan S, Svenson IK, et al. A Kinesin Heavy Chain (KIF5A) Mutation in Hereditary Spastic Paraplegia (SPG10). The American Journal of Human Genetics. 2002 Nov;71(5):1189–94.
54. Crimella C, Baschirotto C, Arnoldi A, Tonelli A, Tenderini E, Airoldi G, et al. Mutations in the motor and stalk domains of KIF5A in spastic paraplegia type 10 and in axonal Charcot-Marie-Tooth type 2. Clin Genet. 2012 Aug;82(2):157–64.
55. Liu YT, Laura M, Hersheson J, Horga A, Jaunmuktane Z, Brandner S, et al. Extended phenotypic spectrum of KIF5A mutations: From spastic paraplegia to axonal neuropathy. Neurology. 2014 Aug 12;83(7):612–9.
56. Miki H, Setou M, Kaneshiro K, Hirokawa N. All kinesin superfamily protein, KIF, genes in mouse and human. Proceedings of the National Academy of Sciences. 2001 Jun 19;98(13):7004–11.
57. Hirokawa N, Noda Y, Tanaka Y, Niwa S. Kinesin superfamily motor proteins and intracellular transport. Nat Rev Mol Cell Biol. 2009 Oct;10(10):682–96.
58. ADIO S, RETH J, BATHE F, WOEHLKE G. Review: regulation mechanisms of Kinesin-1. J Muscle Res Cell Motil. 2006 Feb 1;27(2):153–60.
59. de Boer EMJ, van Rheenen W, Goedee HS, Kamsteeg EJ, Brilstra EH, Veldink JH, et al. Genotype-phenotype correlations of *KIF5A* stalk domain variants. Amyotroph Lateral Scler Frontotemporal Degener. 2021 Oct 2;22(7–8):561–70.
60. Baron DM, Fenton AR, Saez-Atienzar S, Giampetruzzi A, Sreeram A, Shankaracharya, et al. ALS-associated KIF5A mutations abolish autoinhibition resulting in a toxic gain of function. Cell Rep. 2022 Apr;39(1):110598.
61. Kawaguchi K. Role of Kinesin-1 in the Pathogenesis of SPG10, a Rare Form of Hereditary Spastic Paraplegia. The Neuroscientist. 2013 Aug 10;19(4):336–44.
62. Seog DH, Lee DH, Lee SK. Molecular Motor Proteins of the Kinesin Superfamily Proteins (KIFs): Structure, Cargo and Disease. J Korean Med Sci. 2004;19(1):1.
63. Campbell PD, Shen K, Sapio MR, Glenn TD, Talbot WS, Marlow FL. Unique Function of Kinesin Kif5A in Localization of Mitochondria in Axons. Journal of Neuroscience. 2014 Oct 29;34(44):14717–32.
64. Karle KN, Möckel D, Reid E, Schöls L. Axonal transport deficit in a KIF5A –/– mouse model. Neurogenetics. 2012 May 1;13(2):169–79.
65. Xia CH, Roberts EA, Her LS, Liu X, Williams DS, Cleveland DW, et al. Abnormal neurofilament transport caused by targeted disruption of neuronal kinesin heavy chain KIF5A. Journal of Cell Biology. 2003 Apr 14;161(1):55–66.
66. Cook C, Petrucelli L. Genetic Convergence Brings Clarity to the Enigmatic Red Line in ALS. Neuron. 2019 Mar;101(6):1057–69.
67. Kok JR, Palminha NM, dos Santos Souza C, El-Khamisy SF, Ferraiuolo L. DNA damage as a mechanism of neurodegeneration in ALS and a contributor to astrocyte toxicity. Cellular and Molecular Life Sciences. 2021 Aug 26;78(15):5707–29.
68. Yang J, Xu ZP, Huang Y, Hamrick HE, Duerksen-Hughes PJ, Yu YN. ATM and ATR: Sensing DNA damage. World J Gastroenterol. 2004;10(2):155.
69. Rass U, Ahel I, West SC. Defective DNA Repair and Neurodegenerative Disease. Cell. 2007 Sep;130(6):991–1004.
70. Ogawa LM, Baserga SJ. Crosstalk between the nucleolus and the DNA damage response. Mol Biosyst. 2017;13(3):443–55.
71. Shaikh AY, Martin LJ. DNA base-excision repair enzyme apurinic/apyrimidinic endonuclease/redox factor-1 is increased and competent in the brain and spinal cord

of individuals with amyotrophic lateral sclerosis. Neuromolecular Med. 2002 Aug;2(1):47–60.
72. VehvilÃ¤inen P, Koistinaho J, Gundars G. Mechanisms of mutant SOD1 induced mitochondrial toxicity in amyotrophic lateral sclerosis. Front Cell Neurosci. 2014 May 9;8.
73. Kim BW, Jeong YE, Wong M, Martin LJ. DNA damage accumulates and responses are engaged in human ALS brain and spinal motor neurons and DNA repair is activatable in iPSC-derived motor neurons with SOD1 mutations. Acta Neuropathol Commun. 2020 Dec 31;8(1):7.
74. Wang WY, Pan L, Su SC, Quinn EJ, Sasaki M, Jimenez JC, et al. Interaction of FUS and HDAC1 regulates DNA damage response and repair in neurons. Nat Neurosci. 2013 Oct 15;16(10):1383–91.
75. Hill SJ, Mordes DA, Cameron LA, Neuberg DS, Landini S, Eggan K, et al. Two familial ALS proteins function in prevention/repair of transcription-associated DNA damage. Proceedings of the National Academy of Sciences. 2016 Nov 29;113(48).
76. Polci R, Peng A, Chen PL, Riley DJ, Chen Y. NIMA-Related Protein Kinase 1 Is Involved Early in the Ionizing Radiation-Induced DNA Damage Response. Cancer Res. 2004 Dec 15;64(24):8800–3.
77. Fang X, Lin H, Wang X, Zuo Q, Qin J, Zhang P. The NEK1 interactor, C21ORF2, is required for efficient DNA damage repair. Acta Biochim Biophys Sin (Shanghai). 2015 Oct 1;47(10):834–41.
78. Skourti-Stathaki K, Proudfoot NJ, Gromak N. Human Senataxin Resolves RNA/DNA Hybrids Formed at Transcriptional Pause Sites to Promote Xrn2-Dependent Termination. Mol Cell. 2011 Jun;42(6):794–805.
79. Farg MA, Konopka A, Soo KY, Ito D, Atkin JD. The DNA damage response (DDR) is induced by the C9orf72 repeat expansion in amyotrophic lateral sclerosis. Hum Mol Genet. 2017 Aug 1;26(15):2882–96.
80. Walker C, Herranz-Martin S, Karyka E, Liao C, Lewis K, Elsayed W, et al. C9orf72 expansion disrupts ATM-mediated chromosomal break repair. Nat Neurosci. 2017 Sep 17;20(9):1225–35.
81. Lopez-Gonzalez R, Lu Y, Gendron TF, Karydas A, Tran H, Yang D, et al. Poly(GR) in C9ORF72 -Related ALS/FTD Compromises Mitochondrial Function and Increases Oxidative Stress and DNA Damage in iPSC-Derived Motor Neurons. Neuron. 2016 Oct;92(2):383–91.
82. Higelin J, Catanese A, Semelink-Sedlacek LL, Oeztuerk S, Lutz AK, Bausinger J, et al. NEK1 loss-of-function mutation induces DNA damage accumulation in ALS patient-derived motoneurons. Stem Cell Res. 2018 Jul;30:150–62.
83. Andrade NS, Ramic M, Esanov R, Liu W, Rybin MJ, Gaidosh G, et al. Dipeptide repeat proteins inhibit homology-directed DNA double strand break repair in C9ORF72 ALS/FTD. Mol Neurodegener. 2020 Dec 24;15(1):13.
84. Kannan A, Cuartas J, Gangwani P, Branzei D, Gangwani L. Mutation in senataxin alters the mechanism of R-loop resolution in amyotrophic lateral sclerosis 4. Brain. 2022 Sep 14;145(9):3072–94.
85. Konopka A, Atkin JD. DNA Damage, Defective DNA Repair, and Neurodegeneration in Amyotrophic Lateral Sclerosis. Front Aging Neurosci. 2022 Apr 27;14.
86. Nihei Y, Mori K, Werner G, Arzberger T, Zhou Q, Khosravi B, et al. Poly-glycine–alanine exacerbates C9orf72 repeat expansion-mediated DNA damage via sequestration of phosphorylated ATM and loss of nuclear hnRNPA3. Acta Neuropathol. 2020 Jan 23;139(1):99–118.
87. Goldberg MW. Nuclear pore complex tethers to the cytoskeleton. Semin Cell Dev Biol. 2017 Aug;68:52–8.

88. Schmidt HB, Görlich D. Transport Selectivity of Nuclear Pores, Phase Separation, and Membraneless Organelles. Trends Biochem Sci. 2016 Jan;41(1):46–61.
89. Vanneste J, van den Bosch L. The Role of Nucleocytoplasmic Transport Defects in Amyotrophic Lateral Sclerosis. Int J Mol Sci. 2021 Nov 10;22(22):12175.
90. Kinoshita Y, Ito H, Hirano A, Fujita K, Wate R, Nakamura M, et al. Nuclear Contour Irregularity and Abnormal Transporter Protein Distribution in Anterior Horn Cells in Amyotrophic Lateral Sclerosis. J Neuropathol Exp Neurol. 2009 Nov;68(11):1184–92.
91. Chou CC, Zhang Y, Umoh ME, Vaughan SW, Lorenzini I, Liu F, et al. TDP-43 pathology disrupts nuclear pore complexes and nucleocytoplasmic transport in ALS/FTD. Nat Neurosci. 2018 Feb 8;21(2):228–39.
92. Tyzack GE, Luisier R, Taha DM, Neeves J, Modic M, Mitchell JS, et al. Widespread FUS mislocalization is a molecular hallmark of amyotrophic lateral sclerosis. Brain. 2019 Sep 1;142(9):2572–80.
93. Steyaert J, Scheveneels W, Vanneste J, van Damme P, Robberecht W, Callaerts P, et al. FUS-induced neurotoxicity in Drosophila is prevented by downregulating nucleocytoplasmic transport proteins. Hum Mol Genet. 2018 Sep 7;
94. Xiao S, MacNair L, McGoldrick P, McKeever PM, McLean JR, Zhang M, et al. Isoform-specific antibodies reveal distinct subcellular localizations of <scp>C</scp> 9orf72 in amyotrophic lateral sclerosis. Ann Neurol. 2015 Oct 29;78(4):568–83.
95. Donnelly CJ, Zhang PW, Pham JT, Haeusler AR, Mistry NA, Vidensky S, et al. RNA Toxicity from the ALS/FTD C9ORF72 Expansion Is Mitigated by Antisense Intervention. Neuron. 2013 Oct;80(2):415–28.
96. Zhang K, Donnelly CJ, Haeusler AR, Grima JC, Machamer JB, Steinwald P, et al. The C9orf72 repeat expansion disrupts nucleocytoplasmic transport. Nature. 2015 Sep 3;525(7567):56–61.
97. Jovičić A, Mertens J, Boeynaems S, Bogaert E, Chai N, Yamada SB, et al. Modifiers of C9orf72 dipeptide repeat toxicity connect nucleocytoplasmic transport defects to FTD/ALS. Nat Neurosci. 2015 Sep 26;18(9):1226–9.
98. Freibaum BD, Lu Y, Lopez-Gonzalez R, Kim NC, Almeida S, Lee KH, et al. GGGGCC repeat expansion in C9orf72 compromises nucleocytoplasmic transport. Nature. 2015 Sep 3;525(7567):129–33.
99. Boeynaems S, Bogaert E, van Damme P, van den Bosch L. Inside out: the role of nucleocytoplasmic transport in ALS and FTLD. Acta Neuropathol. 2016 Aug 6;132(2):159–73.
100. Shi KY, Mori E, Nizami ZF, Lin Y, Kato M, Xiang S, et al. Toxic PR_n poly-dipeptides encoded by the *C9orf72* repeat expansion block nuclear import and export. Proceedings of the National Academy of Sciences. 2017 Feb 14;114(7).
101. Andersen PM, Al-Chalabi A. Clinical genetics of amyotrophic lateral sclerosis: What do we really know? Vol. 7, Nature Reviews Neurology. 2011. p. 603–15.
102. Wu CH, Fallini C, Ticozzi N, Keagle PJ, Sapp PC, Piotrowska K, et al. Mutations in the profilin 1 gene cause familial amyotrophic lateral sclerosis. Nature. 2012 Aug 15;488(7412):499–503.
103. Giampetruzzi A, Danielson EW, Gumina V, Jeon M, Boopathy S, Brown RH, et al. Modulation of actin polymerization affects nucleocytoplasmic transport in multiple forms of amyotrophic lateral sclerosis. Nat Commun. 2019 Dec 23;10(1):3827.
104. Sivadasan R, Hornburg D, Drepper C, Frank N, Jablonka S, Hansel A, et al. C9ORF72 interaction with cofilin modulates actin dynamics in motor neurons. Nat Neurosci. 2016 Dec 10;19(12):1610–8.
105. Fallini C, Khalil B, Smith CL, Rossoll W. Traffic jam at the nuclear pore: All roads lead to nucleocytoplasmic transport defects in ALS/FTD. Neurobiol Dis. 2020 Jul;140:104835.

106. An. Actin disruption agents induce phosphorylation of histone H2AX in human breast adenocarcinoma MCF-7 cells. Oncol Rep. 2011 May 1;25(5).
107. dos Santos Á, Cook AW, Gough RE, Schilling M, Olszok NA, Brown I, et al. DNA damage alters nuclear mechanics through chromatin reorganization. Nucleic Acids Res. 2021 Jan 11;49(1):340–53.
108. Rouleau GA, Clark AW, Rooke K, Pramatarova A, Krizus A, Suchowersky O, et al. SOD1 mutation is assosiated with accumulation of neurofilaments in amyotrophic lateral scelaries. Ann Neurol. 1996 Jan;39(1):128–31.
109. Williamson TL, Cleveland DW. Slowing of axonal transport is a very early event in the toxicity of ALS–linked SOD1 mutants to motor neurons. Nat Neurosci. 1999 Jan;2(1):50–6.
110. Zhang B, Tu P hsien, Abtahian F, Trojanowski JQ, Lee VMY. Neurofilaments and Orthograde Transport Are Reduced in Ventral Root Axons of Transgenic Mice that Express Human SOD1 with a G93A Mutation. Journal of Cell Biology. 1997 Dec 1;139(5):1307–15.
111. de Vos KJ, Chapman AL, Tennant ME, Manser C, Tudor EL, Lau KF, et al. Familial amyotrophic lateral sclerosis-linked SOD1 mutants perturb fast axonal transport to reduce axonal mitochondria content. Hum Mol Genet. 2007 Nov 15;16(22):2720–8.
112. Fallini C, Bassell GJ, Rossoll W. The ALS disease protein TDP-43 is actively transported in motor neuron axons and regulates axon outgrowth. Hum Mol Genet. 2012 Aug 15;21(16):3703–18.
113. Volkening K, Leystra-Lantz C, Yang W, Jaffee H, Strong MJ. Tar DNA binding protein of 43 kDa (TDP-43), 14-3-3 proteins and copper/zinc superoxide dismutase (SOD1) interact to modulate NFL mRNA stability. Implications for altered RNA processing in amyotrophic lateral sclerosis (ALS). Brain Res. 2009 Dec;1305:168–82.
114. Alami NH, Smith RB, Carrasco MA, Williams LA, Winborn CS, Han SSW, et al. Axonal Transport of TDP-43 mRNA Granules Is Impaired by ALS-Causing Mutations. Neuron. 2014 Feb;81(3):536–43.
115. Fumagalli L, Young FL, Boeynaems S, de Decker M, Mehta AR, Swijsen A, et al. *C9orf72* -derived arginine-containing dipeptide repeats associate with axonal transport machinery and impede microtubule-based motility. Sci Adv. 2021 Apr 9;7(15).
116. Smith BN, Ticozzi N, Fallini C, Gkazi AS, Topp S, Kenna KP, et al. Exome-wide Rare Variant Analysis Identifies TUBA4A Mutations Associated with Familial ALS. Neuron. 2014 Oct;84(2):324–31.
117. Figlewicz DA, Rouleau GA, Krizus A, Julien JP. Polymorphism in the multi-phosphorylation domain of the human neurofilament heavy-subunit-encoding gene. Gene. 1993 Oct;132(2):297–300.
118. Gros-Louis F, Larivière R, Gowing G, Laurent S, Camu W, Bouchard JP, et al. A Frameshift Deletion in Peripherin Gene Associated with Amyotrophic Lateral Sclerosis. Journal of Biological Chemistry. 2004 Oct;279(44):45951–6.
119. Pant DC, Parameswaran J, Rao L, Loss I, Chilukuri G, Parlato R, et al. <scp>ALS</scp> -linked <scp>KIF5A ΔExon27</scp> mutant causes neuronal toxicity through gain-of-function. EMBO Rep. 2022 Aug 3;23(8).
120. Nakano J, Chiba K, Niwa S. An <scp>ALS</scp> -associated <scp>KIF5A</scp> mutant forms oligomers and aggregates and induces neuronal toxicity. Genes to Cells. 2022 Jun 20;27(6):421–35.
121. Nicolas A, Kenna KP, Renton AE, Ticozzi N, Faghri F, Chia R, et al. Genome-wide Analyses Identify KIF5A as a Novel ALS Gene. Neuron. 2018 Mar;97(6):1268-1283.e6.

122. Dutta M, Diehl MR, Onuchic JN, Jana B. Structural consequences of hereditary spastic paraplegia disease-related mutations in kinesin. Proceedings of the National Academy of Sciences. 2018 Nov 13;115(46).
123. Füger P, Sreekumar V, Schüle R, Kern J v., Stanchev DT, Schneider CD, et al. Spastic Paraplegia Mutation N256S in the Neuronal Microtubule Motor KIF5A Disrupts Axonal Transport in a Drosophila HSP Model. PLoS Genet. 2012 Nov 29;8(11):e1003066.
124. Takahashi K, Yamanaka S. Induction of Pluripotent Stem Cells from Mouse Embryonic and Adult Fibroblast Cultures by Defined Factors. Cell. 2006 Aug;126(4):663–76.
125. Zhang X, Hu D, Shang Y, Qi X. Using induced pluripotent stem cell neuronal models to study neurodegenerative diseases. Biochimica et Biophysica Acta (BBA) - Molecular Basis of Disease. 2020 Apr;1866(4):165431.
126. Rivetti di Val Cervo P, Besusso D, Conforti P, Cattaneo E. hiPSCs for predictive modelling of neurodegenerative diseases: dreaming the possible. Nat Rev Neurol. 2021 Jun 3;17(6):381–92.
127. Jiang J, Zhu Q, Gendron TF, Saberi S, McAlonis-Downes M, Seelman A, et al. Gain of Toxicity from ALS/FTD-Linked Repeat Expansions in C9ORF72 Is Alleviated by Antisense Oligonucleotides Targeting GGGGCC-Containing RNAs. Neuron. 2016 May;90(3):535–50.
128. O'Rourke JG, Bogdanik L, Muhammad AKMG, Gendron TF, Kim KJ, Austin A, et al. C9orf72 BAC Transgenic Mice Display Typical Pathologic Features of ALS/FTD. Neuron. 2015 Dec;88(5):892–901.
129. Peters OM, Cabrera GT, Tran H, Gendron TF, McKeon JE, Metterville J, et al. Human C9ORF72 Hexanucleotide Expansion Reproduces RNA Foci and Dipeptide Repeat Proteins but Not Neurodegeneration in BAC Transgenic Mice. Neuron. 2015 Dec;88(5):902–9.
130. Cohen-Hadad Y, Altarescu G, Eldar-Geva T, Levi-Lahad E, Zhang M, Rogaeva E, et al. Marked Differences in C9orf72 Methylation Status and Isoform Expression between C9/ALS Human Embryonic and Induced Pluripotent Stem Cells. Stem Cell Reports. 2016 Nov;7(5):927–40.
131. Selvaraj BT, Livesey MR, Zhao C, Gregory JM, James OT, Cleary EM, et al. C9ORF72 repeat expansion causes vulnerability of motor neurons to Ca2+-permeable AMPA receptor-mediated excitotoxicity. Nat Commun. 2018 Dec 24;9(1):347.
132. Dafinca R, Barbagallo P, Talbot K. The Role of Mitochondrial Dysfunction and ER Stress in TDP-43 and C9ORF72 ALS. Front Cell Neurosci. 2021 Apr 1;15.
133. Medina DX, Boehringer A, Dominick M, Lorenzini I, Saez-Atienzar S, Pioro EP, et al. Generation of two induced pluripotent stem cell (iPSC) lines from an ALS patient with simultaneous mutations in KIF5A and MATR3 genes. Stem Cell Res. 2021 Jan;50:102141.
134. Ahmad I, Goel D, Ghosh A, Kapoor H, Kumar D, Srivastava AK, et al. Lab resource: Single cell line generation and characterization of a human-derived induced pluripotent stem cell line (IGIBi005-A) from a patient with spastic paraplegia/ataxia/ALS phenotype due to the mutation of the gene Kinesin Family Member 5A (KIF5A). Stem Cell Res. 2022 Oct;64:102904.
135. Miller TM, Pestronk A, David W, Rothstein J, Simpson E, Appel SH, et al. An antisense oligonucleotide against SOD1 delivered intrathecally for patients with SOD1 familial amyotrophic lateral sclerosis: a phase 1, randomised, first-in-man study. Lancet Neurol. 2013 May;12(5):435–42.
136. Miller TM, Cudkowicz ME, Genge A, Shaw PJ, Sobue G, Bucelli RC, et al. Trial of Antisense Oligonucleotide Tofersen for *SOD1* ALS. New England Journal of Medicine. 2022 Sep 22;387(12):1099–110.

137. Sareen D, O'Rourke JG, Meera P, Muhammad AKMG, Grant S, Simpkinson M, et al. Targeting RNA Foci in iPSC-Derived Motor Neurons from ALS Patients with a *C9ORF72* Repeat Expansion. Sci Transl Med. 2013 Oct 23;5(208).
138. Lagier-Tourenne C, Baughn M, Rigo F, Sun S, Liu P, Li HR, et al. Targeted degradation of sense and antisense *C9orf72* RNA foci as therapy for ALS and frontotemporal degeneration. Proceedings of the National Academy of Sciences. 2013 Nov 19;110(47).
139. Su Z, Zhang Y, Gendron TF, Bauer PO, Chew J, Yang WY, et al. Discovery of a Biomarker and Lead Small Molecules to Target r(GGGGCC)-Associated Defects in c9FTD/ALS. Neuron. 2014 Sep;83(5):1043–50.
140. Simone R, Balendra R, Moens TG, Preza E, Wilson KM, Heslegrave A, et al. G-quadruplex-binding small molecules ameliorate *C9orf72* <scp>FTD</scp> / <scp>ALS</scp> pathology *in vitro* and *in vivo*. EMBO Mol Med. 2018 Jan 7;10(1):22–31.
141. Kramer NJ, Carlomagno Y, Zhang YJ, Almeida S, Cook CN, Gendron TF, et al. Spt4 selectively regulates the expression of *C9orf72* sense and antisense mutant transcripts. Science (1979). 2016 Aug 12;353(6300):708–12.
142. Bush JA, Meyer SM, Fuerst R, Tong Y, Li Y, Benhamou RI, et al. A blood–brain penetrant RNA-targeted small molecule triggers elimination of $r(G_4C_2)^{exp}$ in c9ALS/FTD via the nuclear RNA exosome. Proceedings of the National Academy of Sciences. 2022 Nov 29;119(48).
143. Amoroso MW, Croft GF, Williams DJ, O'Keeffe S, Carrasco MA, Davis AR, et al. Accelerated High-Yield Generation of Limb-Innervating Motor Neurons from Human Stem Cells. Journal of Neuroscience. 2013 Jan 9;33(2):574–86.
144. Fernandopulle MS, Prestil R, Grunseich C, Wang C, Gan L, Ward ME. Transcription Factor–Mediated Differentiation of Human iPSCs into Neurons. Curr Protoc Cell Biol. 2018 Jun 1;79(1).
145. Licata N v, Cristofani R, Salomonsson S, Wilson KM, Kempthorne L, Vaizoglu D, et al. C9orf72 ALS/FTD dipeptide repeat protein levels are reduced by small molecules that inhibit PKA or enhance protein degradation. EMBO J. 2022 Jan 4;41(1).
146. Liu YJ, McIntyre RL, Janssens GE, Houtkooper RH. Mitochondrial fission and fusion: A dynamic role in aging and potential target for age-related disease. Mech Ageing Dev. 2020 Mar;186:111212.
147. Bardelli D, Sassone F, Colombrita C, Volpe C, Gumina V, Peverelli S, et al. Reprogramming fibroblasts and peripheral blood cells from a *C9ORF72* patient: A proof-of-principle study. J Cell Mol Med. 2020 Apr 3;24(7):4051–60.
148. Zu T, Liu Y, Bañez-Coronel M, Reid T, Pletnikova O, Lewis J, et al. RAN proteins and RNA foci from antisense transcripts in *C9ORF72* ALS and frontotemporal dementia. Proceedings of the National Academy of Sciences. 2013 Dec 17;110(51).
149. McGoldrick P, Zhang M, van Blitterswijk M, Sato C, Moreno D, Xiao S, et al. Unaffected mosaic *C9orf72* case. Neurology. 2018 Jan 23;90(4):e323–31.
150. Ababneh NA, Scaber J, Flynn R, Douglas A, Barbagallo P, Candalija A, et al. Correction of amyotrophic lateral sclerosis related phenotypes in induced pluripotent stem cell-derived motor neurons carrying a hexanucleotide expansion mutation in C9orf72 by CRISPR/Cas9 genome editing using homology-directed repair. Hum Mol Genet. 2020 Aug 3;29(13):2200–17.
151. Zhao C, Devlin A, Chouhan AK, Selvaraj BT, Stavrou M, Burr K, et al. Mutant *C9orf72* human iPSC-derived astrocytes cause non-cell autonomous motor neuron pathophysiology. Glia. 2020 May 16;68(5):1046–64.

152. Galiakberova AA, Dashinimaev EB. Neural Stem Cells and Methods for Their Generation From Induced Pluripotent Stem Cells in vitro. Front Cell Dev Biol. 2020 Oct 8;8.
153. Sharma A, Singh K, Almasan A. Histone H2AX Phosphorylation: A Marker for DNA Damage. In 2012. p. 613–26.
154. Du ZW, Chen H, Liu H, Lu J, Qian K, Huang CL, et al. Generation and expansion of highly pure motor neuron progenitors from human pluripotent stem cells. Nat Commun. 2015 May 25;6(1):6626.
155. Hu BY, Zhang SC. Differentiation of spinal motor neurons from pluripotent human stem cells. Nat Protoc. 2009 Sep 20;4(9):1295–304.
156. Thiry L, Clément JP, Haag R, Kennedy TE, Stifani S, Kennedy T. Optimization of long-term human iPSC-derived spinal motor neuron culture using a dendritic polyglycerol amine-based substrate. Available from: https://doi.org/10.1101/2021.09.14.460098
157. Hyung S, Yoon Lee B, Park JC, Kim J, Hur EM, Francis Suh JK. Coculture of Primary Motor Neurons and Schwann Cells as a Model for In Vitro Myelination. Sci Rep. 2015 Dec 12;5(1):15122.
158. An. Actin disruption agents induce phosphorylation of histone H2AX in human breast adenocarcinoma MCF-7 cells. Oncol Rep. 2011 May 1;25(5).
159. Lash LL, Wallar BJ, Turner JD, Vroegop SM, Kilkuskie RE, Kitchen-Goosen SM, et al. Small-Molecule Intramimics of Formin Autoinhibition: A New Strategy to Target the Cytoskeletal Remodeling Machinery in Cancer Cells. Cancer Res. 2013 Nov 15;73(22):6793–803.
160. Hetrick B, Han MS, Helgeson LA, Nolen BJ. Small Molecules CK-666 and CK-869 Inhibit Actin-Related Protein 2/3 Complex by Blocking an Activating Conformational Change. Chem Biol. 2013 May;20(5):701–12.
161. Müller P, Langenbach A, Kaminski A, Rychly J. Modulating the Actin Cytoskeleton Affects Mechanically Induced Signal Transduction and Differentiation in Mesenchymal Stem Cells. PLoS One. 2013 Jul 29;8(7):e71283.
162. Hirano K, Chartier L, Taylor RG, Allen RE, Fusetani N, Karaki H, et al. Changes in the cytoskeleton of 3T3 fibroblasts induced by the phosphatase inhibitor, calyculin-A. J Muscle Res Cell Motil. 1992 Jun;13(3):341–53.
163. Gao J, Nakamura F. Actin-Associated Proteins and Small Molecules Targeting the Actin Cytoskeleton. Int J Mol Sci. 2022 Feb 14;23(4):2118.
164. Towbin BD, González-Aguilera C, Sack R, Gaidatzis D, Kalck V, Meister P, et al. Step-Wise Methylation of Histone H3K9 Positions Heterochromatin at the Nuclear Periphery. Cell. 2012 Aug;150(5):934–47.
165. Fernandez Alanis E, Pinotti M, Dal Mas A, Balestra D, Cavallari N, Rogalska ME, et al. An exon-specific U1 small nuclear RNA (snRNA) strategy to correct splicing defects. Hum Mol Genet. 2012 Jun 1;21(11):2389–98.
166. Nizzardo M, Simone C, Dametti S, Salani S, Ulzi G, Pagliarani S, et al. Spinal muscular atrophy phenotype is ameliorated in human motor neurons by SMN increase via different novel RNA therapeutic approaches. Sci Rep. 2015 Dec 30;5(1):11746.
167. Donegà S, Rogalska ME, Pianigiani G, Igreja S, Amaral MD, Pagani F. Rescue of common exon-skipping mutations in cystic fibrosis with modified U1 snRNAs. Hum Mutat. 2020 Dec 14;41(12):2143–54.
168. Dal Mas A, Fortugno P, Donadon I, Levati L, Castiglia D, Pagani F. Exon-Specific U1s Correct SPINK *5* Exon 11 Skipping Caused by a Synonymous Substitution that Affects a Bifunctional Splicing Regulatory Element. Hum Mutat. 2015 May;36(5):504–12.
169. Balestra D, Faella A, Margaritis P, Cavallari N, Pagani F, Bernardi F, et al. An engineered <scp>U</scp> 1 small nuclear <scp>RNA</scp> rescues splicing-

defective coagulation <*scp*>*F*</*scp*> *7* gene expression in mice. Journal of Thrombosis and Haemostasis. 2014 Feb 7;12(2):177–85.
170. Romano G, Riccardi F, Bussani E, Vodret S, Licastro D, Ragone I, et al. Rescue of a familial dysautonomia mouse model by AAV9-Exon-specific U1 snRNA. The American Journal of Human Genetics. 2022 Aug;109(8):1534–48.
171. Donadon I, Pinotti M, Rajkowska K, Pianigiani G, Barbon E, Morini E, et al. Exon-specific U1 snRNAs improve ELP1 exon 20 definition and rescue ELP1 protein expression in a familial dysautonomia mouse model. Hum Mol Genet. 2018 Jul 15;27(14):2466–76.
172. Donadon I, Bussani E, Riccardi F, Licastro D, Romano G, Pianigiani G, et al. Rescue of spinal muscular atrophy mouse models with AAV9-Exon-specific U1 snRNA. Nucleic Acids Res. 2019 Aug 22;47(14):7618–32.
173. Rogalska ME, Tajnik M, Licastro D, Bussani E, Camparini L, Mattioli C, et al. Therapeutic activity of modified U1 core spliceosomal particles. Nat Commun. 2016 Sep 4;7(1):11168.
174. Schwarz TL. Mitochondrial Trafficking in Neurons. Cold Spring Harb Perspect Biol. 2013 Jun 1;5(6):a011304–a011304.
175. Denton K, Mou Y, Xu CC, Shah D, Chang J, Blackstone C, et al. Impaired mitochondrial dynamics underlie axonal defects in hereditary spastic paraplegias. Hum Mol Genet. 2018 Jul 15;27(14):2517–30.
176. Hares K, Redondo J, Kemp K, Rice C, Scolding N, Wilkins A. Axonal motor protein KIF5A and associated cargo deficits in multiple sclerosis lesional and normal-appearing white matter. Neuropathol Appl Neurobiol. 2017 Apr;43(3):227–41.
177. Farfel-Becker T, Roney JC, Cheng XT, Li S, Cuddy SR, Sheng ZH. Neuronal Soma-Derived Degradative Lysosomes Are Continuously Delivered to Distal Axons to Maintain Local Degradation Capacity. Cell Rep. 2019 Jul;28(1):51-64.e4.
178. de Vitis E, la Pesa V, Gervaso F, Romano A, Quattrini A, Gigli G, et al. A microfabricated multi-compartment device for neuron and Schwann cell differentiation. Sci Rep. 2021 Mar 29;11(1):7019.
179. Fukuda Y, Pazyra-Murphy MF, Silagi ES, Tasdemir-Yilmaz OE, Li Y, Rose L, et al. Binding and transport of SFPQ-RNA granules by KIF5A/KLC1 motors promotes axon survival. Journal of Cell Biology. 2021 Jan 4;220(1).

LIST OF FIGURES AND TABLES

DISSEMINATION OF RESULTS

1. Poster presentation

Data obtained during my PhD work have been disseminated to the public by presenting posters at the following national and international conferences:

1. **European Network to Cure ALS (ENCALS) MEETING 2021**, Virtual, 12-14/05/2021
"Effect of *NEK1/C9ORF72* double mutation on DNA damage response in patient-derived neural stem cells"
S. Santangelo, C.Colombrita, P. Bossolasco, S.Peverelli, S.Invernizzi, A. Brusati, V. Gumina, D.Bardelli, N. Ticozzi, V. Silani, A. Ratti

2. **1st European Society for Neurochemistry (ESN)** conference, "Future perspectives for European neurochemistry - a young scientists conference". Virtual, 25-26/05/2021
"Effect of *NEK1/C9ORF72* double mutation on DNA damage response in patient-derived neural stem cells"
S. Santangelo, C.Colombrita, P. Bossolasco, S.Peverelli, S.Invernizzi, A. Brusati, V. Gumina, D.Bardelli, N. Ticozzi, V. Silani, A. Ratti

3. **BioMeTra workshop 2021**, Università degli Studi di Milano, Milan, 27/09/2021
- "Generation of mutant *KIF5A* iPSC and its isogenic control by CRISPR/Cas9 system: a new in vitro model to study pathomechanisms underlying *KIF5A*-related disorders"
S. Santangelo, P. Bossolasco, D. Bardelli, S. Magri, D. Di Bella, C. Colombrita, V. Silani, F. Taroni, A. Ratti
- "Effect of *NEK1/C9ORF72* double mutation on DNA damage response in patient-derived neural stem cells"
S. Santangelo, C.Colombrita, P. Bossolasco, S.Peverelli, S.Invernizzi, A. Brusati, V. Gumina, D.Bardelli, N. Ticozzi, V. Silani, A. Ratti

4. **FIRST INTERNATIONAL STEMNET MEETING**, Padua, Italy, 22-24/09/2021
"Effect of *NEK1/C9ORF72* double mutation on DNA damage response in neural stem cells and motoneurons derived from Amyotrophic Lateral Sclerosis patient"
S. Santangelo, C.Colombrita, P. Bossolasco, S.Peverelli, S.Invernizzi, A. Brusati, V. Gumina, D.Bardelli, N. Ticozzi, V. Silani, A. Ratti

5. **32nd INTERNATIONAL SYMPOSIUM ON ALS/MND**, Virtual, 07-10/12/2021
"Effect of *NEK1/C9ORF72* double mutation on DNA damage response in patient-derived iPSC-motoneurons"
S. Santangelo, C. Colombrita, P. Bossolasco, S. Peverelli, S. Invernizzi, A. Brusati, V. Gumina, D. Bardelli, N. Ticozzi, V. Silani, A. Ratti

6. **European Network to Cure ALS (ENCALS) MEETING 2022**, Edinburgh, Scotland, 01-03/06/2022
"Rapamycin reverts TDP-43 splicing defects in a human in vitro model of TDP-43 proteinopathy"
V. Casiraghi, C. Colombrita, S. Santangelo, I. Milone, M. Sorce, V. Silani, A. Ratti

7. **ALS Association – Arizona Chapter – LiveLikeLou Foundation meeting 2022**, Phoenix, Arizona, USA, 15-16/07/2022

"Effects of nuclear pore disruption on mRNA processing in *C9ORF72* mutant iPSC derived cortical neurons"

M. Gregoire, S. Santangelo, C. Fallini

8. **BioMeTra workshop 2022.** Università degli Studi di Milano, Milan, 20/09/2022

"Modeling a novel N-terminal mutation of *KIF5A* gene in patient-derived iPSC-motoneurons"

S. Santangelo, P. Bossolasco, C. Fallini, S. Magri, M. Bertocchi, S. Invernizzi, D. Di Bella, D. Bardelli, C. Colombrita, V. Silani, F. Taroni, A. Ratti

9. **AriSLA meeting 2022,** Milan, 3-4/11/2022

- "U1 snRNA as a novel RNA-based therapeutic approach to modulate *C9ORF72* pathology in patient-derived iPSC-motoneurons"

S. Santangelo, C. Colombrita, E. Bussani, S.Invernizzi, M. Nice Sorce, V. Casiraghi, C. Lattuada, P. Bossolasco, V. Silani, F. Pagani, A. Ratti

- "Modeling ALS disease by 3D organoids culture from human-derived iPSCs"

M. N. Sorce, L. Lattuada, S. Santangelo, P. Podini, S. Invernizzi, V. Casiraghi, A. Quattrini, V. Silani, A. Ratti, P. Bossolasco

10. **Society for Neuroscience (SfN),** San Diego, California, USA, 11-16/11/2022

"Modeling a novel N-terminal mutation of *KIF5A* gene in patient-derived iPSC-motoneurons"

S. Santangelo, P. Bossolasco, C. Fallini, S. Magri, M. Bertocchi, S. Invernizzi, D. Di Bella, D. Bardelli, C. Colombrita, V. Silani, F. Taroni, A. Ratti

11. **52nd Congress of Italian Neurology Society (SIN)**, Milan, 3-6/12/2022

"Modelling ALS disease by 2D and 3D in vitro models of patient-derived iPSC"

P. Bossolasco, S. Santangelo, L. Lattuada, M. N. Sorce, C. Colombrita, V. Casiraghi, S.Peverelli, A. Ratti, V. Silani

12. **33nd INTERNATIONAL SYMPOSIUM ON ALS/MND**, Virtual, 6-9/12/2022

"Characterization of iPSC-motoneurons from a HSP patient with a novel mutation in *KIF5A* N-terminal region"

S. Santangelo, P. Bossolasco, C. Fallini, S. Magri, M. Bertocchi, S. Invernizzi, D. Di Bella, D. Bardelli, C. Colombrita, V. Silani, F. Taroni, A. Ratti

2. Publications on journals

"Generation of five induced pluripotent stem cells lines from four members of the same family carrying a C9orf72 repeat expansion and one wild-type member". Stem Cell Research, 2022.

Chiara Lattuada; Serena Santangelo; Silvia Peverelli; Philip McGoldrick; Ekaterina Rogaeva; Lorne Zinman; Georg Haase; Vincent Géli; Vincenzo Silani; Janice Robertson; Antonia Ratti.

https://doi.org/10.1016/j.scr.2022.102998

"Generation of an iPSC line from a patient with spastic paraplegia type 10 carrying a novel mutation in *KIF5A* gene". Stem Cell Research, 2022.

Serena Santangelo; Patrizia Bossolasco; Stefania Magri; Claudia Colombrita; Sabrina

Invernizzi; Cinzia Gellera; Lorenzo Nanetti; Daniela Di Bella; Vincenzo Silani; Franco Taroni, Antonia Ratti. https://doi.org/10.1016/j.scr.2022.103008

Under review

"Association of APOE genotype and CSF Aβ and tau biomarkers with cognitive and motor phenotype in ALS". Brain, 2022.
Maranzano, Alessio; Verde, Federico; Dubini, Antonella; Torre, Silvia; *Colombo, Eleonora; Doretti, Alberto; Gentile, Francesco; Manini, Arianna; Milone, Ilaria; Brusati, Alberto; Peverelli, Silvia; Santangelo, Serena; Torresani, Erminio; Gentilini, Davide; Messina, Stefano; Morelli, Claudia; Poletti, Barbara; Ratti, Antonia; Silani, Vincenzo; Ticozzi, Nicola*

3. Lay summary

Amyotrophic Lateral Sclerosis (ALS) is an incurable and adult-onset neurodegenerative disease characterized by the loss of motor neurons, leading to a progressive and severe muscular atrophy with rapid death for respiratory failure.
The study of ALS has always been hampered by the lack of suitable experimental models to study disease mechanisms. The recent possibility to obtain induced pluripotent stem cells (iPSC) directly from patients' blood or biopsies has revolutionized the study of neurodegenerative disorders because iPSC can be differentiated into any kind of cell, including motor neurons and glial cells, and used to generate brain organoids.
My research provides evidence that patient-derived iPSC carrying different genetic mutations represent suitable platforms to study the disease and to test new potential therapeutic approaches for ALS treatment.

La sclerosi laterale amiotrofica (SLA) è una malattia neurodegenerativa incurabile dell'età adulta, che causa la perdita dei neuroni motori e porta a progressiva paralisi e atrofia muscolare, culminante con la morte per arresto respiratorio. Lo studio della SLA è da sempre stato ostacolato dalla mancanza di modelli sperimentali che potessero mimare in modo adeguato i meccanismi alla base della malattia.
La recente possibilità di generare cellule staminali pluripotenti indotte (iPSC) direttamente da sangue o da biopsie cutanee del paziente ha rivoluzionato lo studio delle malattie neurodegenerative poiché le iPSC possono essere differenziate in qualsiasi tipo cellulare, inclusi i neuroni motori e cellule gliali, e anche usate per ottenere organoidi cerebrali.
Il mio lavoro di ricerca dimostra che queste cellule derivate da paziente rappresentano una piattaforma efficace per studiare in modo efficace la SLA *in vitro* e per testare nuovi potenziali approcci terapeutici per la cura della malattia.

APPENDIX

Stem Cell Research 66 (2023) 103008

Contents lists available at ScienceDirect

Stem Cell Research

journal homepage: www.elsevier.com/locate/scr

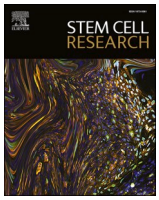

Lab Resource: Single Cell Line

Generation of an iPSC line from a patient with spastic paraplegia type 10 carrying a novel mutation in *KIF5A* gene

Serena Santangelo [a,b], Patrizia Bossolasco [b], Stefania Magri [c], Claudia Colombrita [b], Sabrina Invernizzi [b], Cinzia Gellera [c], Lorenzo Nanetti [c], Daniela Di Bella [c], Vincenzo Silani [b,d], Franco Taroni [c], Antonia Ratti [a,b,*]

[a] Department of Medical Biotechnology and Translational Medicine, Università degli Studi di Milano, Milan, Italy
[b] Department of Neurology and Laboratory of Neuroscience, IRCCS Istituto Auxologico Italiano, Milan, Italy
[c] Unit of Medical Genetics and Neurogenetics, Fondazione IRCCS Istituto Neurologico Carlo Besta, Milan, Italy
[d] Department of Pathophysiology and Transplantation, "Dino Ferrari" Center, Università degli Studi di Milano, Milan, Italy

A B S T R A C T

We generated an iPSC line from a patient with spastic paraplegia type 10 (SPG10) carrying the novel missense variant c.50G > A (p.R17Q) in the *N*-terminal motor domain of the kinesin family member 5A (*KIF5A*) gene.

This patient-derived *in vitro* cell model will help to investigate the role of different *KIF5A* mutations in inducing neurodegeneration in spastic paraplegia and in other *KIF5A*-related disorders, including Charcot-Marie-Tooth type 2 (CMT2) and amyotrophic lateral sclerosis (ALS).

Resource table

Unique stem cell line identifier	IAIi010-A
Alternative name(s) of stem cell line	KIF5A_C3
Institution	IRCCS Istituto Auxologico Italiano, Milan, Italy
Contact information of distributor	Antonia Ratti, antonia.ratti@unimi.it
Type of cell line	iPSC
Origin	Human
Additional origin info required for human ESC or iPSC	Ethnicity: Caucasian Age: 79 Sex: Female
Cell Source	Skin fibroblasts
Clonality	Clonal
Method of reprogramming	CytoTune iPS 2.0 Sendai Reprogramming Kit
Genetic Modification	NO
Type of Genetic Modification	N/A
Evidence of the reprogramming transgene loss (including genomic copy if applicable)	RT-PCR
Associated disease	Autosomal dominant Spastic Paraplegia type 10 (SGP10)
Gene/locus	KIF5A, chromosome 12q13.13 NM_004984.3: c.50G > A (p.R17Q)
Date archived/stock date	October 2022
Cell line repository/bank	https://hpscreg.eu/user/cellline/edit/IAIi010-A
Ethical approval	Ethical committee Regione Lombardia, sezione Fondazione IRCCS Istituto Neurologico "Carlo Besta", Milan, Italy, Approval n.64

1. Resource utility

Allelic mutations in *KIF5A* gene are associated to different neurodegenerative disorders, such as spastic paraplegia type 10 (SPG10), axonal Charcot-Marie-Tooth type 2 (CMT2), and amyotrophic lateral sclerosis (ALS) as well as to neonatal intractable myoclonus (NEIMY) with distinct mutational hotspots.

We generated an iPSC line from a SPG10 individual carrying the novel missense mutation p.R17Q (c.50G > A) in KIF5A protein motor domain.

This iPSC line represents a new *in vitro* disease model to elucidate, upon differentiation into motoneurons, the pathomechanisms associated with *KIF5A* mutations.

* Corresponding author.
E-mail address: antonia.ratti@unimi.it (A. Ratti).

https://doi.org/10.1016/j.scr.2022.103008
Received 18 November 2022; Accepted 19 December 2022
Available online 21 December 2022

2. Resource details

The kinesin family member 5A (*KIF5A*) gene encodes for the heavy chain of the kinesin motor protein involved in the anterograde transport of synaptic vesicles, RNA granules, mitochondria and neurofilaments along dendrites and axons in neurons.

KIF5A forms a dimer of identical heavy chains which associate with 2 identical 60–70-kDa light chains. The KIF5A heavy chain contains 3 domains: an *N*-terminal globular domain (motor domain), a long alpha-helical coiled coil domain (stalk domain), and a small C-terminal globular domain (cargo domain).

Interestingly, *KIF5A* missense mutations in the *N*-terminal motor domain have been linked to SPG10 and CMT2 (Reid et al., 2002), loss-of-function variants in the C-terminal cargo-binding domain to ALS (Nicolas et al., 2018; Brenner et al., 2018 Mar), while C-terminal variants with a dominant-negative effect to the neurodevelopmental disorder

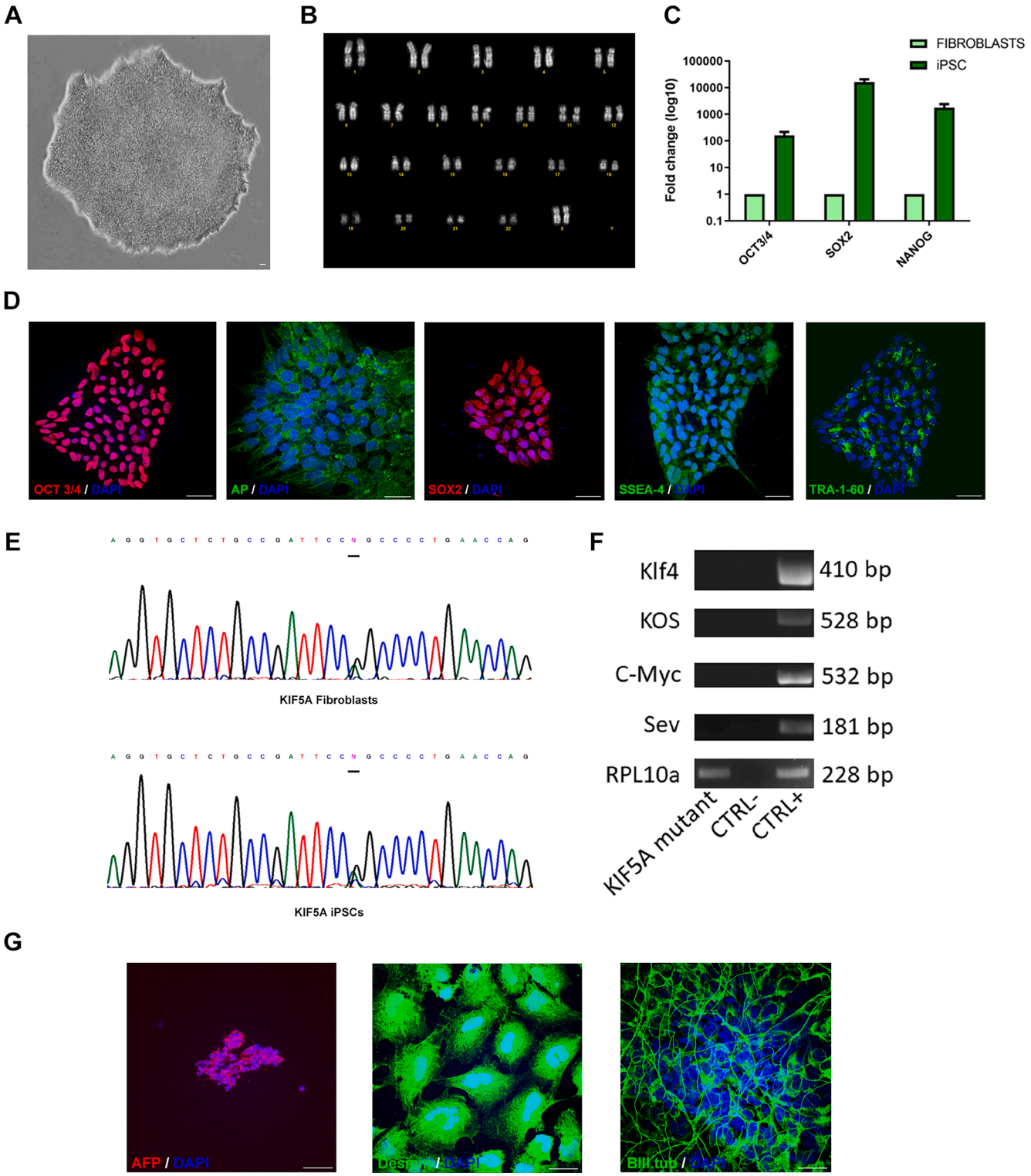

Fig. 1. Characterization of the generated iPSc line.

NEIMY (Duis et al., 2016).

The establishment of *in vitro* models to study *KIF5A*-related disorders is essential to understand the exact mechanisms whereby *KIF5A* allelic variants lead to neurodegeneration and cause different clinical phenotypes.

A targeted mutational screening of patients with hereditary spastic paraplegia allowed to identify a novel heterozygous missense variant (c.50G > A, p.R17Q) in the ATP-binding motor domain of *KIF5A* at the *N*-terminal region.

We isolated skin fibroblasts from the mutant SPG10 patient which were then reprogrammed into iPSC (IAIi010-A) using the Cytotune™-iPS 2.0 Sendai Reprogramming kit (ThermoFisher Scientific). The clonal iPSC colonies were isolated and, after expansion in E8 medium, they showed the typical stem cell morphology **(**Fig. 1**A)** and a normal karyotype (46, XX) at G-banding analysis **(**Fig. 1**B)**.

We evaluated their pluripotency status by the expression of OCT3/4, SOX2 and NANOG by Q-PCR (Fig. 1**C)** and of OCT3/4, AP (Alkaline Phosphatase), SOX2, SSEA-4 and TRA-1-60 pluripotency markers by immunofluorescence staining **(**Fig. 1**D)**.

Sanger sequencing confirmed the presence of the heterozygous c.50 G > A mutation in *KIF5A* exon 1 both in the SPG10 patient's fibroblasts and in the derivative iPSC line **(**Fig. 1**E).** Perfect matching with the original fibroblasts was also assessed by genotyping 22 different STRs (short tandem repeats) (data available on request).

Absence of the Sendai vector transcripts (Klf4, Kos, c-Myc, and Sev) was confirmed by semi-quantitative RT-PCR **(**Fig. 1**F).**

The ability of this iPSC line to spontaneously differentiate into derivatives of the three germ layers was assessed by *in vitro* embryoid body (EB) formation and immunofluorescence staining for specific markers: α-fetoprotein (AFP; endoderm), Desmin (mesoderm) and βIII-tubulin (ectoderm) **(**Fig. 1**G).**

The generated iPSC line tested negative for Mycoplasma infection **(Supplementary** Fig. 1**).**

The complete characterization is summarized in Table 1.

Table 1
Characterization and validation.

Classification	Test	Result	Data
Morphology	Brightfield image	Typical human pluripotent stem cell colony morphology	Fig. 1*A*
Phenotype	Qualitative analysis by immunocytochemistry	Expression of pluripotency markers: OCT3/4, Alkaline Phosphatase, SOX2, SSEA-4, TRA-1-60	Fig. 1*D*
	Quantitative analysis by Q-PCR	Expression of pluripotency markers: OCT3/4, SOX2, NANOG	Fig. 1*C*
Genotype	Karyotype (Q-banding) and resolution	46, XX	Fig. 1*B*
Identity	STR analysis	22 STR analyzed with 22 perfect matches	*Available from the Authors*
Mutation analysis	Sanger sequencing	Heterozygous mutation NM_004984.3: c.50G > A (p. R17Q) in *KIF5A*	Fig. 1*E*
	Southern Blot OR WGS	*N/A*	*N/A*
Microbiology and virology	Mycoplasma	Mycoplasma testing by PCR: Negative	*Suppl.* Fig. 1
Differentiation potential	Embryoid body-derived germ layers	Expression of specific markers: endoderm (AFP), mesoderm (Desmin) and ectoderm (βIII-Tubulin)	Fig. 1*G*
List of recommended germ layer markers	Expression of specific germ layers markers by Immunofluorescence	Positivity for the AFP (endoderm), Desmin (mesoderm) and βIII-Tubulin (ectoderm) markers	Fig. 1*G*
Donor screening (OPTIONAL)	HIV 1 + 2 Hepatitis B, Hepatitis C	N/A	N/A
Genotype additional info (OPTIONAL)	Blood group genotyping	N/A	N/A
	HLA tissue typing	N/A	N/A

3. Materials and methods

3.1. Fibroblast reprogramming

Primary fibroblasts were obtained from skin biopsy and reprogramming was performed within the fifth passage *in vitro*. iPSCs were obtained using the CytoTune®-iPS 2.0 Sendai Reprogramming Kit (Thermo Fisher Scientific) following manufacturer's instructions.

Briefly, 24 h after transduction, the fibroblast cell medium was replaced with fresh medium and cells were then cultured for 6 more days, replacing the medium every other day. At day 7, fibroblasts were plated in fresh fibroblast medium into 6-well plate pre-coated with hESC-Qualified Matrix (Corning). At day 8, the medium was replaced with Essential 8 medium (Thermo Fisher) until emerging colonies reached a suitable size to be manually picked. Colonies were grown at 37 °C, 5 % CO2 and splitted 1:10 using 0.5 mM EDTA solution.

3.2. Karyotyping

Standard cytogenetic procedures were used to analyse iPSC karyotype. Following overnight addition of Colcemid solution (KaryoMAX™, Thermo Fisher Scientific), chromosome analysis was achieved by Q-Band staining.

3.3. Immunocytochemistry

iPSCs cultured on glass coverslips were fixed in 4 % paraformaldehyde for 20 min and permeabilized with 0.3 % Triton X-100 (Sigma-Aldrich) for 10 min at room temperature. Cells were then incubated for 20 min in 10 % normal goat serum (NGS)(Gibco) in PBS and primary antibodies were added for 90 min at 37 °C.

After two washes with 10 % NGS/PBS, cells were stained with secondary antibodies. Nuclei were stained using DAPI (Sigma-Aldrich) and images acquired with a confocal microscope Nikon Eclipse Ti using a 60x oil-immersion objective. All the antibodies used are listed in Table 2.

3.4. In vitro spontaneous differentiation

Embryoid bodies (EBs) were generated by suspending iPSC in low-adhesion plates in HuES medium (DMEM/F12, NEAA, KSR, Glutamine, Pen/Strep, β-mercaptoethanol). After 7 days, EBs were plated on Matrigel-coated (Corning) coverslips and grown in Essential 8 medium for additional 10 days. Expression of the three-germ layer-specific markers was evaluated by immunofluorescence **(**Table 2**).**

3.5. Quantitative PCR (Q-PCR)

Total RNA was isolated with the TRIzol reagent (Invitrogen) and reversed transcribed using SuperScript II reverse transcriptase (Invitrogen). Q-PCR was performed using SYBRGreen reaction mix

Table 2
Reagents details.

	Antibodies used for immunocytochemistry/flow-cytometry			
	Antibody	**Dilution**	**Company Cat #**	**RRID**
Pluripotency Markers	Mouse anti-Alkaline Phosphatase (AP)	1:250	Abcam cat# ab-108337	*RRID: AB_10862036*
	Mouse anti-SSEA-4	1:100	Invitrogen 14-8843-80	*RRID: AB_657847*
	Mouse anti-TRA-1-60	1:125	Invitrogen 14-8863-80	*RRID: AB_891612*
	Mouse anti-OCT-3/4	1:200	Santa Cruz Biotechnology cat#sc-5279	*RRID: AB_628051*
	Rabbit anti-SOX2	1:70	Abcam cat#ab15830	*RRID: AB_443255*
Differentiation Markers	Rabbit anti-βIII-Tubulin	1:500	Abcam cat#ab-52623	*RRID: AB_869991*
	Rabbit anti-Desmin	1:10	Chemicon Millipore cat#AB907	*RRID: AB_2092609*
	Mouse anti-Alpha-fetoprotein (AFP)	1:125	Invitrogen cat#14-6583-80	*RRID: AB_2865213*
e.g. Secondary antibodies	Alexa FluorTM 488 goat anti-mouse IgG (H + L)	1:500	Life Technologies cat# A-11001	*RRID: AB_2534069*
	Alexa FluorTM 555 goat anti-mouse IgG (H + L)	1:500	Life Technologies cat#A21422	*RRID: AB_2535844*
	Alexa FluorTM 555 goat anti-rabbit IgG (H + L)	1.500	Life Technologies cat# A-21428	*RRID: AB_2535849*
Nuclear stain	4′,6-diamidino-2-phenylindole, dihydrochloride (DAPI)	2 μg/mL	Sigma-Aldrich D9542	
	Primers			
	Target	**Size of band**	**Forward/Reverse primer (5′-3′)**	
Pluripotency Markers (qPCR)	OCT3/4	81 bp	Fwd: AGTGCCCGAAACCCACACTG Rev: CCACACTCGGACCACATCCT	
	SOX2	151 bp	Fwd: GGGAAATGGGAGGGGTGCAAAAGAGG Rev: CACCAATCCCATCCACACTCACGCAA	
	NANOG	154 bp	Fwd: TGAACCTCAGCTACAAACAG Rev: TGGTGGTAGGAAGAGTAAAG	
House-Keeping Genes (Q-PCR)	RPL10a	51 bp	Fwd: GAAGAAGGTGTTATGTCTGG Rev: TCTGTCATCTTCACGTGAC	
Sendai virus detection (RT-PCR)	Klf4	528 bp	Fwd: TTCCTGCATGCCAGAGGAGCCC Rev: AATGTATCGAAGGTGCTCAA	
	Kos	410 bp	Fwd: ATGCACCGCTACGACGTGAGCGC Rev: ACCTTGACAATCCTGATGTGG	
	c-Myc	532 bp	Fwd: TAACTGACTAGCAGGCTTGTCG Rev: TCCACATACAGTCCTGGATGATGATG	
	Sev	181 bp	Fwd: GGATCACTAGGTGATATCGAGC Rev: ACCAGACAAGAGTTTAAGAGATATGTATC	
	RPL10a	228 bp	Fwd: CAAGAAGCTGGCCAAGAAGTATG Rev: TCTGTCATCTTCACGTGAC	
Genotyping	22 STRs (CyberGene AB kit)	N/A	N/A	
Targeted mutation analysis/sequencing	KIF5A	370 bp	Fwd: CAGAGACTGAGCACCTGTCCTCC Rev: GGGGAAGAGGATGAAGGATGAGC	

(ThermoFisher Scientific) and specific primer pairs (Table 2) using QuantStudio 12 k Flex instrument (Applied Biosystems). Target gene expression data (Ct) were normalized to RPL10a gene Ct values (ΔCt) and fold change was calculated as $2^{-\Delta\Delta Ct}$.

3.6. Sanger sequencing

Genomic DNA was extracted using the Wizard® Genomic DNA Purification Kit (Promega) and amplified by PCR using specific primer pairs (Table 2). Amplicons were sequenced with BigDye Terminator v3.1 Cycle Sequencing Kit on an ABI 3500 Genetic Analyzer (Applied Biosystems).

3.7. STR analysis

The genetic STR profile was obtained using ChromoQuant SuperSTaR Optima QF-PCR Kit (CyberGene AB) detecting 22 STR loci according to the manufacturer's instructions. Amplicons were run on ABI Prism 3500 Genetic Analyzer and fragment lengths determined by Gene Mapper v.4 software (Applied Biosystems).

3.8. Mycoplasma detection

Mycoplasma test was performed using the *N*-GARDE Mycoplasma Detection PCR Kit (Euroclone) following the manufacturer's instructions. Amplicons were run on 1.5 % agarose gel together with positive and negative control samples.

Resource table.

Declaration of Competing Interest

The authors declare that they have no known competing financial interests or personal relationships that could have appeared to influence the work reported in this paper.

Acknowledgments

This work was financially supported by the Italian Ministry of Health (Grant RF-2018-12367768 and RRC 2022).

Appendix A. Supplementary data

Supplementary data to this article can be found online at https://doi.org/10.1016/j.scr.2022.103008.

References

Aude Nicolas, A., Kenna, Kevin P., Renton, Alan E., et al., 2018 Mar 21. Genome-wide analyses identify KIF5A as a novel ALS gene. Neuron 97 (6), 1268–1283.e6. https://doi.org/10.1016/j.neuron.2018.02.027.

Brenner, David, Yilmaz, Rüstem, Müller, Kathrin, et al., 2018 Mar. Hot-spot KIF5A mutations cause familiar ALS. Brain 141 (3), 668–697. https://doi.org/10.1093/brain/awx370.

Duis, Jessica, Dean, Shannon, Applegate, Carolyn, et al., 2016 Oct. KIF5A mutations cause an infantile onset phenotype including severe myoclonus with evidence of mitochondrial dysfunction. Ann. Neurol. 80 (4), 633–637. https://doi.org/10.1002/ana.24744.

Reid, Evan, Kloos, Mark, Ashley-Koch, Allison, Hughes, Lori, et al., 2002 Nov. A Kinesin Heavy Chain (KIF5A) Mutation in Hereditary Spastic Paraplegia (SPG10). Am. J. Hum. Genet. 71 (5), 1189–1194. https://doi.org/10.1086/344210. Epub 2002 Sep 24.

Stem Cell Research 66 (2023) 102998

Contents lists available at ScienceDirect

Stem Cell Research

journal homepage: www.elsevier.com/locate/scr

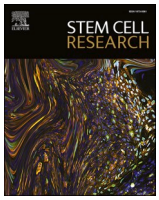

Lab Resource: Multiple Cell Lines

Generation of five induced pluripotent stem cells lines from four members of the same family carrying a *C9orf72* repeat expansion and one wild-type member

Chiara Lattuada [a], Serena Santangelo [a,b], Silvia Peverelli [a], Philip McGoldrick [c], Ekaterina Rogaeva [c], Lorne Zinman [d], Georg Haase [e], Vincent Géli [f], Vincenzo Silani [a,g], Janice Robertson [c], Antonia Ratti [a,b,1], Patrizia Bossolasco [a,1,*]

[a] *Department of Neurology and Laboratory of Neuroscience, IRCCS Istituto Auxologico Italiano, Milan, Italy*
[b] *Department of Medical Biotechnology and Translational Medicine, Università degli Studi di Milano, Milan, Italy*
[c] *Tanz Centre for Research in Neurodegenerative Diseases, University of Toronto, Canada*
[d] *Sunnybrook Health Sciences Centre, Toronto, Canada*
[e] *MPATHY Laboratory, Institute of Systems Neuroscience, U1106 INSERM & Aix-Marseille University, Marseille, France*
[f] *Marseille Cancer Research Centre (CRCM), Inserm U1068, CNRS UMR7258, Institut Paoli-Calmettes, Aix-Marseille University, Marseille, France*
[g] *"Dino Ferrari" Center, Department of Pathophysiology and Transplantation, Università degli Studi di Milano, Milan, Italy*

A B S T R A C T

The most common genetic cause of Amyotrophic Lateral Sclerosis (ALS) is the expansion of a G4C2 hexanucleotide repeat in the *C9orf72* gene. The size of the repeat expansion is highly variable and a cut-off of 30 repeats has been suggested as the lower pathological limit. Repeat size variability has been observed intergenerationally and intraindividually in tissues from different organs and within the same tissue, suggesting instability of the pathological repeat expansion. In order to study this genomic instability, we established iPSCs from five members of the same family of which four carried a *C9orf72* repeat expansion and one was wild-type.

Resource Table:

Unique stem cell lines identifier	IAIi005-A IAIi006-A IAIi007-A IAIi008-A IAIi009-A
Alternative name(s) of stem cell lines	AC52 (IAIi005-A)BC6 (IAIi006-A)CC5 (IAIi007-A)DC2 (IAIi008-A)EC1 (IAIi009-A)
Institution	IRCCS Istituto Auxologico Italiano, Milan, Italy
Contact information of distributor	Patrizia Bossolasco, p. bossolasco@auxologico.it
Type of cell lines	iPSC
Origin	Human
Additional origin info required	Ethnicity: Caucasian (IAIi005-A), Age:89, Sex: MaleEthnicity: Caucasian (IAIi006-A) , Age:65, Sex: FemaleEthnicity: Caucasian (IAIi007-A) , Age:57, Sex: FemaleEthnicity: Caucasian (IAIi008-A) , Age:51, Sex: FemaleEthnicity: Caucasian (IAIi009-A) , Age:65, Sex: Female
Cell Source	Fibroblasts
Clonality	Clonal
Method of reprogramming	Sendai virus
Genetic Modification	No
Type of Genetic Modification	N/A
Evidence of the reprogramming transgene loss (including genomic copy if applicable)	RT-PCR
Associated disease	Amyotrophic lateral sclerosis (ALS)
Gene/locus	*C9orf72* gene/chromosome 9p21.2
Date archived/stock date	
Cell line repository/bank	https://hpscreg.eu/cell-line/IAIi005-A https://hpscreg.eu/cell-line/IAIi006-A https://hpscreg.eu/cell-line/IAIi007-A

(*continued on next column*)

(*continued*)

(*continued on next page*)

* Corresponding author.
E-mail address: p.bossolasco@auxologico.it (P. Bossolasco).
[1] Joint last authors.

https://doi.org/10.1016/j.scr.2022.102998
Received 26 September 2022; Received in revised form 21 November 2022; Accepted 4 December 2022
Available online 9 December 2022

(*continued*)

	https://hpscreg.eu/cell-line/IAIi008-A https://hpscreg.eu/cell-line/IAIi009-A
Ethical approval	Ethical committee of IRCCS Istituto Auxologico Italiano, approval number 2022_03_15_12

1. Resource utility

Hexanucleotide repeat expansions in *C9orf72* cause ALS and Frontotemporal Dementia (FTD), two neurodegenerative diseases in a clinical *continuum*. Generation of iPSCs from four individuals with different repeat expansions and clinical history (3 ALS and 1 asymptomatic) and a wild-type member of the same family will enable study of *C9orf72*-related pathomechanisms.

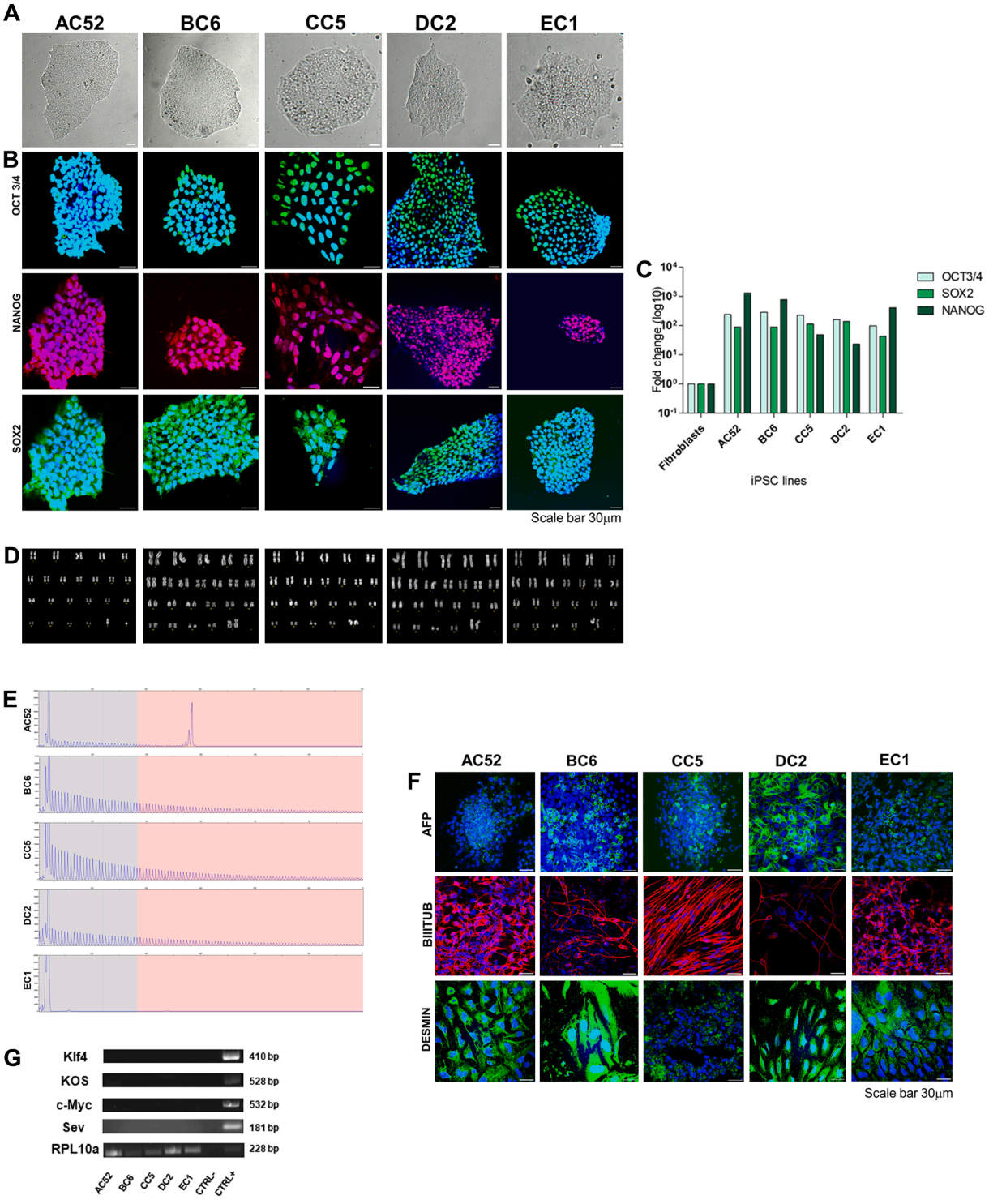

Fig. 1. Characterization of the five iPSC lines.

2. Resource details

Amyotrophic Lateral Sclerosis (ALS) is a fatal neurodegenerative disease affecting spinal, bulbar and cortical motor neurons and leading to a progressive muscular atrophy with rapid death of patients, usually due to respiratory failure. Expansion of the G_4C_2 hexanucleotide repeat in the first intron of *C9orf72* gene is the most common genetic cause of ALS and Frontotemporal Dementia (FTD) (DeJesus-Hernandez and Mackenzie, 2011; McGoldrick et al., 2018). The number of G_4C_2 repeats is polymorphic: 2–23 units in healthy subjects, but>30 to up to thousands in ALS/FTD patients. The correlation between repeat expansion length and disease severity or phenotype still needs to be fully clarified in particular for small expansions (<100 repeats). Similarly, how these expansions may have occurred by genome instability is still under debate. We generated iPSCs lines from five members of the same *C9orf72* family (PED25) already described (Renton et al., 2011; Xi et al., 2015). Previous Southern Blot analysis on both peripheral blood and fibroblasts revealed a small expansion for the asymptomatic father (AC52) (70 repeats), while the three daughters with ALS (BC6, CC5, DC2) had a larger expansion (~1,750 repeats) and one unaffected daughter (EC1) was wild-type (Renton et al., 2011; Xi et al., 2015). Reprogramming was performed on fibroblasts of all these family members using a non-integrating Sendai virus commercial kit. One clone from each subject was fully characterized. All clones displayed an iPSC-like morphology (Fig. 1A), were positive both by immunocytochemistry (Fig. 1B) and qPCR (Fig. 1C) for the pluripotent markers Oct3/4, Nanog and Sox2 and exhibited a normal karyotype (Fig. 1D). Short tandem repeat (STR) analysis confirmed matching of all 22 STR markers between fibroblasts and iPSC, indicating cell identity. Maintenance of a small repeat expansion (47 repeats) in iPSCs of the father, a larger expansion in iPSCs of three ALS daughters and the absence of the expansion in the wild-type daughter's iPSCs was confirmed by Repeat-primed PCR (Fig. 1E). Absence of Mycoplasma contamination was verified by PCR (Suppl. Fig. 1). All clones were able to spontaneously differentiate into the three germ layers *in vitro* as revealed by positivity to specific markers by immunocytochemistry (endoderm: alpha-fetoprotein (AFP); mesoderm: desmin; ectoderm: βIII Tubulin (βIIITub)) (Fig. 1F). Absence of Sendai vector transcripts (Klf4, KOS, c-myc, and Sev) was confirmed by semi-quantitative RT-PCR (Fig. 1G and Table 1).

In summary, we generated clonal cell lines from five members of the same family, fulfilling all the criteria to be considered iPSCs and representing a useful *in vitro* model to study genetic instability of the *C9orf72* repeat expansion. Indeed, in this family, the small repeat expansion of the unaffected father jumped to a larger pathogenic length in the three daughters presenting with ALS (Renton et al., 2011; Xi et al., 2015).

Table 1
Characterization and validation.

Classification	Test	Result	Data
Morphology	Photography Bright field	Normal	Fig. 1A
Phenotype	Qualitative analysis: immunocytochemistry	Expression of the pluripotency markers: Oct3/4, Nanog, Sox2	Fig. 1B
	Quantitative analysis: qPCR	Expression of the pluripotency markers: Oct3/4, Nanog, Sox2	Fig. 1C
Genotype	Karyotype (Q-banding) and resolution	AC52: 46,XY BC6: 46,XX CC5: 46,XX DC2: 46,XX EC1: 46,XX	Fig. 1D
Identity	STR analysis	22 loci analyzed, 22 matched	Available from the authors
Mutation analysis (IF APPLICABLE)	Sequencing	Number of GGGGCC repeats in C9orf72 AC52: 2/47 BC6: 2/> 145 CC5: 2/> 145 DC2: 2/> 145 EC1: 2/2	Fig. 1E
	Southern Blot OR WGS	Not performed	
Microbiology and virology	Mycoplasma	Venor®*GeM* OneStep Mycoplasma detection: all negative	Suppl. Fig. 1
Differentiation potential	Embryoid body derived germ layers	Expression of specific markers: endoderm: AFP, mesoderm: desmin and ectoderm: βIIITub	Fig. 1F
List of recommended germ layer markers	Expression of the markers has to be demonstrated at mRNA (RT PCR) or protein (IF) levels, at least 2 markers need to be shown per germ layer	Expression of specific markers: endoderm: AFP, mesoderm: desmin and ectoderm: βIIITub	Fig. 1F
Donor screening (OPTIONAL)	HIV 1 + 2 Hepatitis B, Hepatitis C	Not performed	N/A
Genotype additional info (OPTIONAL)	Blood group genotyping	Not performed	N/A
	HLA tissue typing	Not performed	N/A

3. Materials and methods

3.1. Fibroblast reprogramming

Fibroblasts from the five family members were obtained and propagated as previously described (Renton et al., 2011). Fibroblasts below passage six were frozen and shipped to the laboratory of Neurosciences (Istituto Auxologico Italiano IRCCS, Italy) where they were reprogrammed using the CytoTune®-iPS 2.0 Sendai Reprogramming Kit (Thermo Fisher Scientific). At day 7, transduced cells were harvested and plated onto Matrigel (Corning) coated dishes. Medium was switched to Essential 8 medium (Thermo Fisher Scientific) until emerging colonies reached a suitable size to be picked. Colonies were grown at 37 °C, 5 % CO2 and passaged 1:10 using 0.5 mM EDTA solution.

3.2. Stemness evaluation

Expression of stemness markers was evaluated by immunocytochemistry and by qPCR. iPSCs grown for 6 passages on coverslips were fixed in 4 % paraformaldehyde (Santa Cruz Biotechnology), permeabilized with 0.3 % Triton X-100 and incubated for 20 min in blocking buffer containing 10 % normal goat serum (Gibco) in PBS. Cells were incubated with primary antibodies (Table 2) for 90 min at 37 °C and then with fluorescently-labelled secondary antibodies (Table 2) for 45 min at room temperature, both antibodies diluted in blocking buffer. Nuclei were stained with DAPI (Sigma-Aldrich). Images were acquired with Eclipse C1 confocal microscope and NIS-elements software (Nikon). For qPCR, total RNA was extracted from iPSCs and fibroblasts using TRIzol Reagent following manufacturer instructions and reverse transcribed using SuperScript II reverse transcriptase. Amplicons were obtained in duplicates with specific primer pairs (Table 2) and SYBRGreen reaction mix (All from ThermoFisher Scientific) using QuantStudio 12 k Flex instrument (Applied Biosystems). Target gene expression data (Ct) were normalized to *RPL10a* gene Ct values and fold change was calculated as $2^{-\Delta\Delta Ct}$.

3.3. Karyotyping

Standard cytogenetic procedures were used to analyse iPSC

Table 2
Reagents details.

	Antibodies used for immunocytochemistry/flow-cytometry Antibody	Dilution	Company Cat #	RRID
Pluripotency marker	Mouse anti-Oct-3/4	1:200	Santa Cruz Biotechnology cat#sc-5279	RRID:AB_628051
	Rabbit anti-Nanog	1:200	Abcam cat#ab21624	RRID:AB_446437
	Rabbit anti-Sox2	1:70	Abcam cat#ab15830	RRID:AB_443255
Differentiation Markers	Rabbit anti-β III tubulin	1:500	Abcamcat#ab-52623	RRID:AB_869991
	Rabbit anti-Desmin	1:10	Chemicon Milliporecat#AB907	RRID:AB_2092609
	Mouse anti-Alpha-fetoprotein	1:125	Invitrogen cat#14-6583-80	RRID:AB_2865213
Secondary antibodies	Alexa FluorTM 488 goat anti-mouse IgG (H+L)	1:500	Life Technologies cat# A-11001	RRID:AB_2534069
	Alexa FluorTM 488 goat anti-rabbit IgG	1:500	Life Technologiescat#A-11008	RRID:AB_143165
	Alexa FluorTM 555 goat anti-rabbit IgG (H+L)	1:500	Life Technologies cat# A-21428	RRID:AB_2535849
Nuclear stain	4′,6-diamidino-2-phenylindole, dihydrochloride (DAPI)	2 μg/mL	Sigma-Aldrich D9542	

	Primers Target	Size of band	Forward/Reverse primer (5′-3′)
Pluripotency Markers (q-PCR)	Oct-04	81 bp	Fwd: AGTGCCCGAAACCCACACTG Rev: CCACACTCGGACCACATCCT
	NANOG	154 bp	Fwd: TGAACCTCAGCTACAAACAG Rev: TGGTGGTAGGAAGAGTAAAG
	SOX2	151 bp	Fwd: GGGAAATGGGAGGGGTGCAAAAGAGG Rev: CACCAATCCCATCCACACTCACGCAA
House-Keeping Genes (q-PCR)	RPL10a	51 bp	Fwd: GAAGAAGGTGTTATGTCTGG Rev: TCTGTCATCTTCACGTGAC
Sendai virus detection (RT-PCR)	KOS	528 bp	Fwd: ATGCACCGCTACGACGTGAGCGC Rev: ACCTTGACAATCCTGATGTGG
	Klf4	410 bp	Fwd: TTCCTGCATGCCAGAGGAGCCC
	Sev	181 bp	Rev: AATGTATCGAAGGTGCTCAA
	c-myc	532 bp	Fwd: TAACTGACTAGCAGGCTTGTCG Rev: TCCACATACAGTCCTGGATGATGATG
	Sev	181 bp	Fwd: GGATCACTAGGTGATATCGAGC Rev: ACCAGACAAGAGTTTAAGAGATATGTATC
	RPL10a	228 bp	Fwd: CAAGAAGCTGGCCAAGAAGTATG Rev: TCTGTCATCTTCACGTGAC
Genotyping	C9orf72 expansion	From 129bp	AmplideX® PCR/CE C9orf72 Kit - Asuragen
Targeted mutation analysis/sequencing	Not performed	N/A	N/A

karyotype. Following overnight addition of Colcemid solution (KaryoMAX™, Thermo Fisher Scientific), chromosome analysis was achieved by Q-Band staining.

3.4. STR analysis

Genomic DNA from the 5 iPSCs cell lines and from the parental fibroblasts was extracted using Wizard Genomic DNA Purification kit (Promega). The genetic STR profile was obtained using ChromoQuant SuperSTaR Optima QF-PCR Kit (CyberGene AB) detecting 22 STR loci (mix solution 1) according to the manufacturer instructions. Amplicons were run on ABI Prism 3500 (Applied Biosystems) and analyzed using Gene Mapper v.4 software (Applied Biosystems).

3.5. Mutation analysis

The presence of the *C9orf72* repeat expansion in iPSCs and fibroblasts was evaluated by Repeat-primed PCR using a commercial kit (Asuragen). Amplicons were analyzed on ABI 3500 Genetic Analyzer and by using Gene Mapper v.4 software. The kit allows detection of repeat expansions up to 145 units.

3.6. Mycoplasma detection

Absence of mycoplasma contamination was evaluated by PCR using a commercial Kit from Minerva biolabs.

3.7. In vitro spontaneous differentiation

To evaluate the spontaneous differentiation potential of iPSCs into the three germ layers, we generated embryoid bodies (EBs) cultured on low adhesion plates in for 7 days (HUES medium). EBs were seeded onto Matrigel-coated plates in Essential 8 medium for an additional 10 days. Immunocytochemical analysis were performed to evaluate the expression of mesodermal, ectodermal and endodermal specific markers (Table 2).

Declaration of Competing Interest

The authors declare that they have no known competing financial interests or personal relationships that could have appeared to influence the work reported in this paper.

Acknowledgments

This work was financially supported by Italian Ministry of Health (E-Rare-3 JTC Grant REPETOMICS).

Appendix A. Supplementary data

Supplementary data to this article can be found online at https://doi.org/10.1016/j.scr.2022.102998.

References

DeJesus-Hernandez, M., Mackenzie, I.R., et al., 2011. Expanded GGGGCC hexanucleotide repeat in noncoding region of C9ORF72 causes chromosome 9p-linked FTD and ALS. Neuron 72 (2), 245–256. https://doi.org/10.1016/j.neuron.2011.09.011.

McGoldrick, P., Zhang, M., van Blitterswijk, M., Sato, C., Moreno, D., Xiao, S., Zhang, A. B., McKeever, P.M., Weichert, A., Schneider, R., Keith, J., Petrucelli, L., Rademakers, R., Zinman, L., Robertson, J., Rogaeva, E., 2018. Unaffected mosaic C9orf72 case: RNA foci, dipeptide proteins, but upregulated C9orf72 expression. Neurology 90 (4), e323–e331. https://doi.org/10.1212/WNL.0000000000004865.

Renton, A.E., Majounie, E., Waite, A., et al., 2011. A hexanucleotide repeat expansion in C9ORF72 is the cause of chromosome 9p21-linked ALS-FTD. Neuron 72 (2), 257–268. https://doi.org/10.1016/j.neuron.2011.09.010.

Xi, Z., van Blitterswijk, M., Zhang, M., McGoldrick, P., McLean, J.R., Yunusova, Y., Knock, E., Moreno, D., Sato, C., McKeever, P.M., Schneider, R., Keith, J.,

Petrescu, N., Fraser, P., Tartaglia, M.C., Baker, M.C., Graff-Radford, N.R., Boylan, K. B., Dickson, D.W., Mackenzie, I.R., Rademakers, R., Robertson, J., Zinman, L., Rogaeva, E., 2015. Jump from pre-mutation to pathologic expansion in C9orf72. Am. J. Hum. Genet. 96 (6), 962–970. https://doi.org/10.1016/j.ajhg.2015.04.016.